

THESIS FOR THE DEGREE OF DOCTOR OF PHILOSOPHY

Design, Modeling and Verification of Distributed Electric Drivetrain

Nimananda Sharma



Division of Electric Power Engineering

Department of Electrical Engineering

CHALMERS UNIVERSITY OF TECHNOLOGY

Gothenburg, Sweden 2022

Design, Modeling and Verification of Distributed Electric Drivetrain

NIMANANDA SHARMA

ISBN: 978-91-7905-673-5

© NIMANANDA SHARMA, 2022.

Doktorsavhandlingar vid Chalmers tekniska högskola

Ny series nr 5139

ISSN 0346-718X

Division of Electric Power Engineering

Department of Electrical Engineering

Chalmers University of Technology

SE-412 79 Gothenburg

Sweden

Telephone +46 (0)31-030 4330

Chalmers Library, Reproservice

Gothenburg, Sweden 2021

Abstract

The electric drivetrain in a battery electric vehicle (BEVs) consists of an electric machine, an inverter, and a transmission. The drivetrain topology of available BEVs, e.g., Nissan Leaf, is centralized with a single electric drivetrain used to propel the vehicle. However, the drivetrain components can be integrated mechanically, resulting in a more compact solution. Furthermore, multiple drivetrain units can propel the vehicle resulting in a distributed drive architecture, e.g., Tesla Model S. Such drivetrains provide an additional degree of control and topology optimization leading to cheaper and more efficient solutions.

To reduce the cost, the drivetrain unit in a distributed drivetrain can be standardized. However, to standardize the drivetrain, the drivetrain needs to be dimensioned such that the performance of a range of different vehicles can be satisfied. This work investigates a method for dimensioning the torque and power of an electric drivetrain that could be standardized across different passenger and light-duty vehicles. A system modeling approach is used to verify the proposed method using drive cycle simulations.

The laboratory verification of such drivetrain components using a conventional dyno test bench can be expensive. Therefore, alternative methods such as power-hardware-in-the-loop (PHIL) and mechanical-hardware-in-the-loop (MHIL) are investigated. The PHIL test method for verifying inverters can be inexpensive as it eliminates the need for rotating electric machines. In this method, the inverter is tested using a machine emulator consisting of a voltage source converter and a coupling network, e.g., inductors and transformer. The emulator is controlled so that currents and voltages at the terminals resemble a machine connected to a mechanical load. In this work, a 60-kW machine emulator is designed and experimentally verified. In the MHIL method, the real-time simulation of the system is combined with a dyno test bench. One drivetrain is implemented in the dyno test bench, while the remaining are simulated using a real-time simulator to utilize this method for distributed drivetrain systems. Including the remaining drivetrains in the real-time simulation eliminates the need for a full-scale dyno test bench, providing a less expensive method for laboratory verification. An MHIL test bench for verification of distributed drivetrain control and components is also designed and experimentally verified.

Index Terms: Distributed drivetrain, electric vehicles, power-hardware-in-the-loop, mechanical-hardware-in-the-loop, real-time modeling, system modeling.

Acknowledgement

I want to take the opportunity here to thank all of those who have positively impacted this work.

Firstly, I would like to thank my main supervisor Yujing Liu for his guidance and support during my studies. He has encouraged me to pursue my research interest and develop technical expertise. Furthermore, he has been very supportive during the ups and downs of my Ph.D. education. Further, I thank my co-supervisor, Emma Grunditz, for her support and valuable feedback on my work. In addition, I would like to thank my examiner Ola Carlson, especially for his guidance in study planning and feedback on this thesis work.

I want to thank all my colleagues from the division who have been instrumental in their support and discussion. Special thanks go to Dr. Junfei Tang for his help with prototyping, experiments, and theoretical and philosophical discussions. I want to thank Georgios Mademlis, ex-office mate, and Bowen Jiang for your support in the experiments and our collaborations. I would also like to thank my office mate Artem Rodionov for all our discussions and collaborations. Lastly, I would like to thank the lunch group for all the exciting discussions and for making it easier to survive the difficult times.

The European Commission financially supports this project. I appreciate the support from the commission and the discussions with the colleagues from the DRIVEMODE project.

Finally, I thank my wife, Afraah Fathima, for her constant support and encouragement.

Nimananda Sharma

Gothenburg, Sweden

August 2022

List of Abbreviations

AC	Alternating current
BEV	Battery electric vehicle
BFM	Backward-facing model
CLC	Current limit circle
CLM	Close loop interface method
DC	Direct current
EMF	Electromotive force
EMI	Electromagnetic interference
FEM	Finite element method
FFM	Forward-facing model
FFT	Fast Fourier transform
FL	Front left
FOC	Field-oriented control
FPGA	Field-programmable gate array
FR	Front right
ICEV	Internal combustion engine-based vehicle
IUT	Inverter under test
MHIL	Mechanical-hardware-in-the-loop
MOSFET	Metal Oxide Semiconductor Field Effect Transistor
MTPA	Maximum torque per ampere
NEF	New energy finance
OLM	Open loop interface method
PHIL	Power-hardware-in-the-loop

PI	Proportional-integral
PLECS	Piecewise linear electrical circuit simulation
PMSM	Permanent magnet synchronous machine
PWM	Pulse width modulation
RL	Resistive and inductive
RMS	Root mean square
SVM	Space vector modulation
UNECE	United nations economic commission for Europe
VLE	Voltage limit ellipse of the emulator VSC
VLM	Voltage limit ellipse of the PMSM
VSC	Voltage source converter
WLTC	Worldwide harmonized light vehicles test cycles

List of Symbols

0	Zero-sequence
a	Phase A; major axis of ellipse
A	Area
b	Phase B; minor axis of ellipse
B	Viscous damping co-efficient
c	Phase C
C	Thermal capacity; Specific heat capacity
C_d	Aero-dynamic drag co-efficient
C_r	Rolling resistance co-efficient
d	Direct-Axis
f	Frequency
g	Acceleration due to gravity
h	Heat transfer co-efficient
i	Current
I	Fundamental component of current; average current
J	Rotating inertia
k	Gear ratio
k_c	Eddy current coefficient
k_h	Hysteresis coefficient
L	Inductance
m	Mass
M	Mutual inductance
p	Pole-pairs, instantaneous active power

P	Average active power; average power loss
q	Quadrature-axis; instantaneous reactive power
Q	Average reactive power
r	Radius
R	Resistance
t	Time
T	Torque; Transformation matrix; Temperature
u	Voltage
U	Fundamental component of voltage; average voltage; voltage amplitude
α	Road gradient angle; α -axis
β	β -axis
ω	Electrical angular frequency
Ω	Mechanical angular speed
ψ	Flux linkage
ρ	Air density
θ	Angle

Contents

Abstract.....	iii
Acknowledgement	v
List of Abbreviations	vi
List of Symbols	ix
Contents.....	xi
Chapter 1 Introduction	1
1.1 Background.....	1
1.2 Contributions of the study.....	4
1.3 Publications	5
Chapter 2 Conceptualization of a Standardized Drivetrain for BEVs	7
2.1 Vehicle classification.....	7
2.1.1 Classification of ICEVs.....	7
2.1.2 Classification of BEVs.....	10
2.2 Wheel torque and power analysis	12
2.3 Electric machine torque and power requirements	16
2.4 System model	19
2.4.1 Electric machine model	19
2.4.2 Inverter.....	23
2.4.3 Machine control	25
2.4.4 Transmission.....	26
2.4.5 Vehicle load	26
2.5 Drive cycle analysis	27
Chapter 3 Control of Machine Emulators.....	36
3.1 Model of coupling network	36
3.1.1 Single-phase inductor	36

3.1.2	Three-phase coupled inductor	39
3.2	Control of machine emulator.....	41
3.2.1	Open loop control	41
3.2.2	Closed loop control.....	42
3.3	Verification of open loop control.....	44
3.3.1	Steady state performance	47
3.3.2	Dynamic performance	50
Chapter 4	Experimental Evaluation of a Machine Emulator	52
4.1	Coupling network	52
4.2	Voltage source converter.....	55
4.3	PHIL test bench.....	55
4.3.1	Steady-state performance.....	56
4.3.2	Dynamic performance	59
4.4	Comparison with a PMSM drive	60
4.4.1	Flux linkage estimation.....	61
4.4.2	Estimation of mechanical parameters	63
4.4.3	Comparison of emulator and PMSM current and voltages.....	65
4.4.4	Steady state comparison of active and reactive power	66
Chapter 5	Design of a High Bandwidth Machine Emulator	67
5.1	Bandwidth of machine emulator	67
5.1.1	Operating region of a machine emulator	67
5.1.2	Dimensioning of coupling network inductance	69
5.1.3	Evaluation of the operating boundary	70
5.2	High bandwidth machine emulator	73
5.2.1	Model of three-phase transformer.....	74
5.2.2	Design of the three-phase transformer	78
5.3	Verification of high bandwidth emulator.....	80
5.3.1	Steady state performance	80

5.3.2	Dynamic performance	81
Chapter 6	MHIL Testing of Multi-Motor Drive System	84
6.1	Mechanical-hardware-in-the-loop test bench	84
6.1.1	Vehicle Model.....	84
6.1.2	Electric Drive Model	86
6.1.3	Dynamometer test bench.....	87
6.2	Interface between real-time simulations and the dyno test bench	88
6.2.1	Open-loop Interface	88
6.2.2	Closed-loop Interface	89
6.3	Experimental results	90
6.3.1	OLM 1 Interface Experimental Results	91
6.3.2	CLM 1 Interface Experimental Results	91
6.3.3	Anti-slip control verification using OLM 1	94
Chapter 7	Conclusions and Future Work.....	97
7.1	Conclusions.....	97
7.2	On-Going and Future Work	98
References	99
Appendix 1	Data of ICEVs	103
Appendix 2	Data of BEVs.....	106

Chapter 1

Introduction

1.1 Background

In the past decade, electrification efforts in transportation have increased, motivated by a need to reduce tailpipe emissions. This growth is evident since the global stock of battery electric vehicles (BEVs) has increased from less than 20 thousand to over 6 million in the past decade, as shown in Figure 1-1 [1]. The increased adoption of BEVs can be attributed to reducing Li-ion battery pack prices [2], government policy support [1], and improved driving range of battery electric vehicles [1]. The price of Li-ion battery packs used in BEVs was reduced by 757% between 2010 and 2019 [2]. In addition, the average driving range has quadrupled between 2015 and 2020 [1]. However, BEVs' average cost is still higher than their internal combustion engine vehicles (ICEVs). A study by Bloomberg NEF on behalf of the European Federation of Transport and Environment predicts that the cost of BEVs is expected to reach price parity with ICEVs by the late 2020s [3]. The main drivers for cost reduction in [3] are manufacturing strategy and battery pack prices. However, one can also expect that standardization of the electric drivetrain could reduce costs.

The electric drivetrain in a BEV consists of an electric machine, an inverter, and a transmission. Although the direct manufacturing cost of an electric drivetrain per [3] is a fraction of the drivetrain in ICEVs, development costs are associated with industrializing new drivetrains for

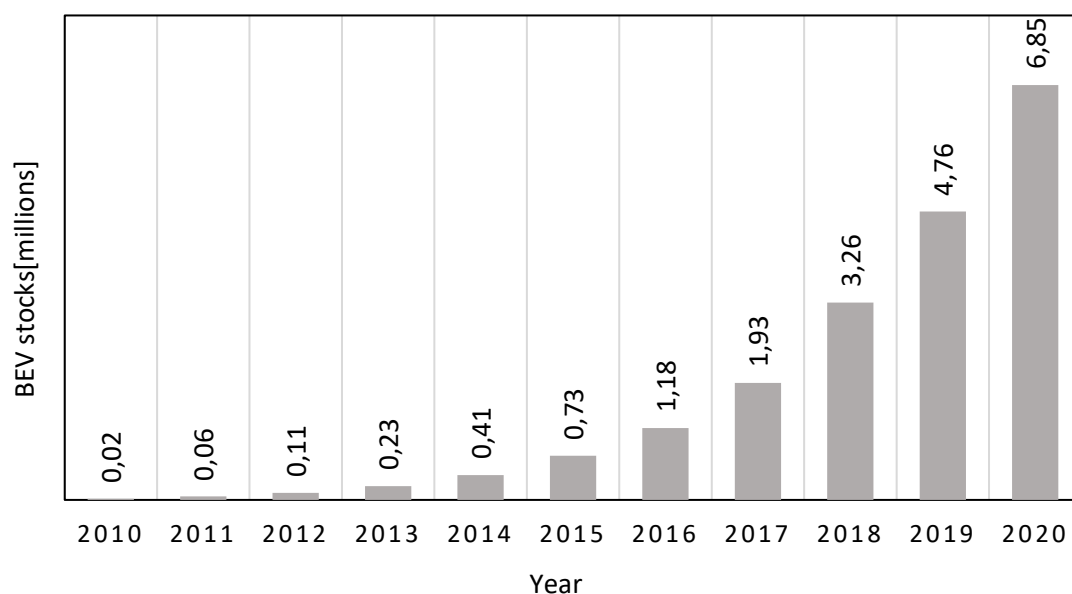


Figure 1-1: Global yearly battery electric vehicle stock starting from 2010 to 2020 [1].

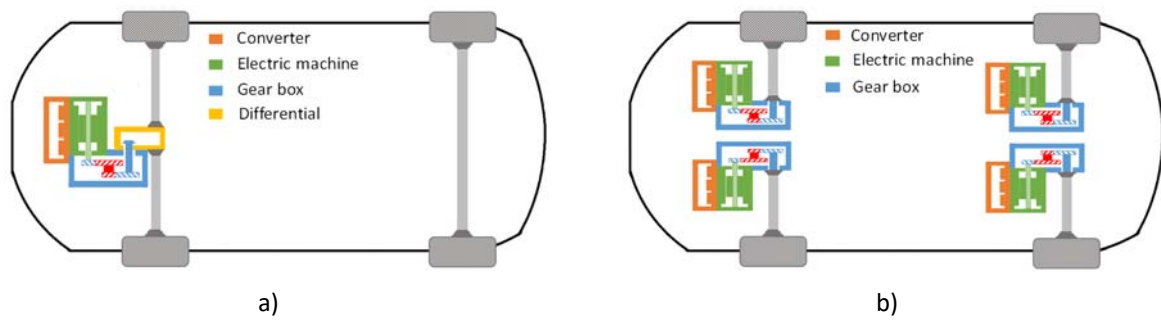


Figure 1-2: An illustration of two different drivetrain architecture a) centralized, b) distributed

different vehicles. The vehicle manufacturer can significantly reduce the development cost by standardizing the drivetrain system across vehicle segments. To standardize the drivetrain, they need to be dimensioned such that the performance of a range of different vehicles can be satisfied. However, standardization is hard to achieve using only centralized drivetrain architecture. In such an architecture, a single electric drivetrain is used to propel the vehicle, as shown in Figure 1-2a. Therefore, the drivetrain is likely to be optimized for a single vehicle model. On the other hand, a distributed architecture uses more than one electric drivetrain to propel a vehicle, as illustrated Figure 1-2b. Therefore, the number of drivetrain units in a distributed architecture can be scaled to meet the performance requirements of various vehicle models.

Distributed drivetrains have been studied extensively in the literature. However, most of the work has focused on optimization of the drivetrain for a particular model and on novel control methods to improve energy efficiency [4] - [10] or vehicle dynamics performance [11] - [13]. To the author's knowledge, no work on using the distributed architecture for conceptualizing a standardized drivetrain is found in the literature. This work investigates a method for dimensioning the torque and power of an electric drivetrain that could be standardized across different passenger BEVs. The method is verified with drive cycle simulations using a system model of electric vehicles.

Laboratory verification of the drivetrain is essential to ensure reliability, performance, and quality. However, using traditional laboratory verification of distributed drivetrains can be expensive and limited as will be discussed in the following sections. Therefore, alternative test methods which are flexible and inexpensive can be interesting. Two such methods, namely power-hardware-in-the-loop (PHIL) and mechanical-hardware-in-loop (MHIL) testing, have been investigated in this work.

In the initial design stage, a three-phase resistive and inductive (RL) circuit can be used as the load to test the inverter. However, it is limited in terms of power factor, currents, and voltage amplitude that can be tested. As shown in Figure 1-3, a dynamometer test bench can be used to test it comprehensively. However, the intended electric machine may not be available during the initial development phases of the inverter. Therefore, the test conditions could still be limited to cover the actual use case. The need for such test benches can be eliminated by using a machine emulator to verify inverters, as shown in Figure 1-4. Test benches as shown in the figure has been referred as PHIL test bench in literature [14] - [26]. The machine emulator in a PHIL test bench consists of a voltage source converter (VSC) which emulates the

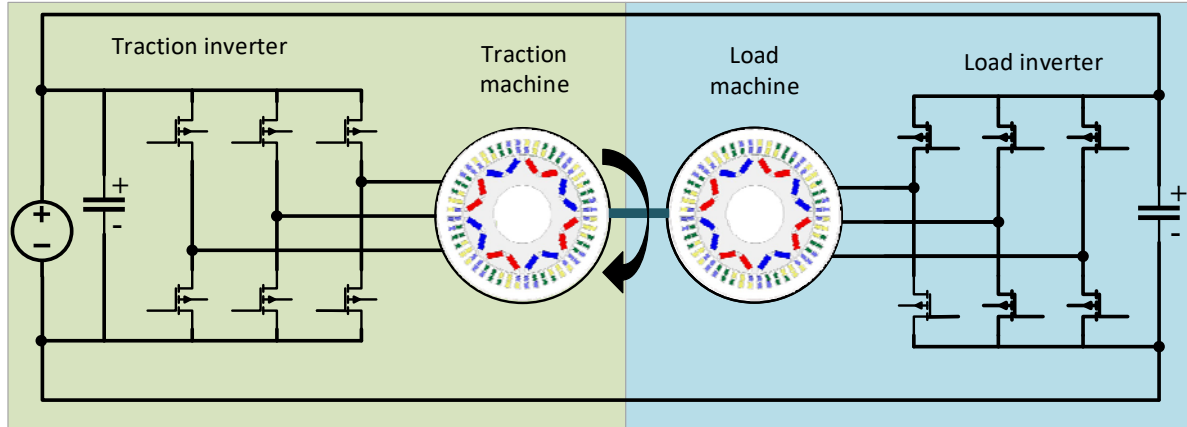


Figure 1-3: A dynamometer test bench for verification of electric machine and inverter

machine back-EMF and a coupling network to represent machine inductance and resistance. The VSC is controlled so that currents and voltages at the emulator terminal resemble a machine connected to a mechanical load. Therefore, the PHIL method can provide a flexible and cost-effective solution for laboratory verification of inverters by eliminating the need for rotating machines.

There are two ways to calculate the voltage reference of VSC in the emulator: closed loop and open loop. Most emulators covered in the literature use the closed loop approach [16], [17], [21], [22], [24], [26] - [29]. However, the emulator setup can be complex and expensive when using a closed loop control since measurement of PWM voltages, VSCs with the higher switching frequency, and FPGAs for control implementation is required [16]. On the other hand, the open loop control can result in a flexible and cheaper solution because it provides two possibilities in selecting a voltage source converter (VSC) to build the emulator. First, a standard 2-level VSC with a similar rating, e.g., voltage, current, and maximum switching frequency as IUT, can be used. Second, the VSC used as IUT can be used inside the emulator.

Very few works are found in the literature using open loop control of machine emulators [14], [18]. In [14] and [18], the verification of the emulator is limited since the emulated machines

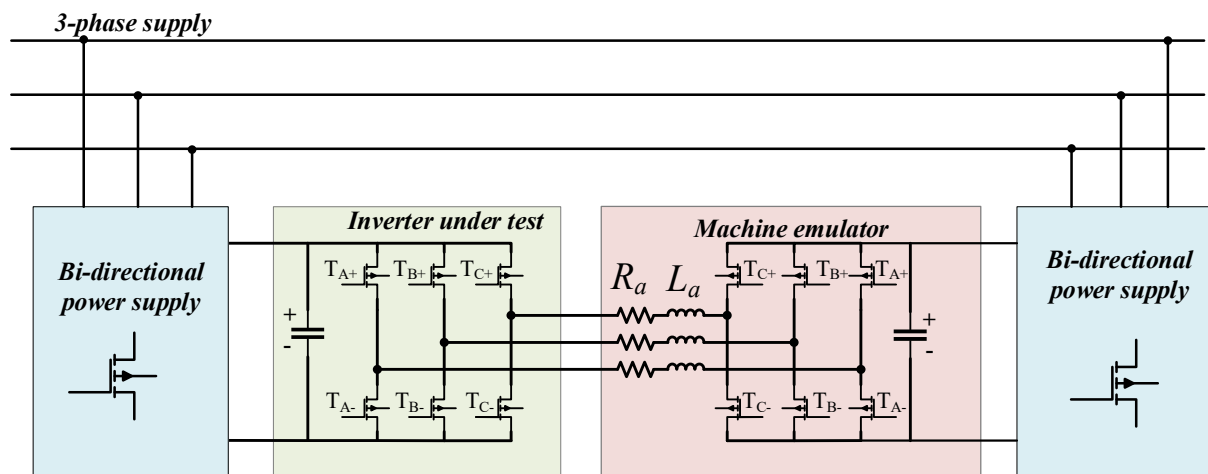


Figure 1-4: A power-hardware-in-the-loop (PHIL) test bench for verification traction inverters

are intended for industrial application. In addition, coupling inductance dimensioning and its effect on the operating range of the emulator are not covered. The operating range for an electric machine in a traction application needs to cover a wider operating region in terms of torque and speed. Therefore, evaluation of the operating range of bandwidth of the emulator becomes significant. Furthermore, the limitation of open loop control is not demonstrated in the reviewed literature. This work investigates the open loop control of the machine emulator to verify the traction inverter with a focus on operating bandwidth and controller performance.

The PHIL test bench, however, is limited in verifying other drivetrain components, e.g., electric machines. The traditional method uses a dynamometer test bench, shown in Figure 1-3. In such a test bench, the traction machine and inverter represent the electric drivetrain under test. The traction machine is often controlled using torque reference. The load machine emulates the driven wheel and is controlled using speed reference. To build a full-scale dynamometer test bench for a distributed drivetrain, e.g., a BEV propelled by two drivetrains, would require two dynamometers [8] [12] [30]. Therefore, such test benches can be very expensive for laboratory verification of such drivetrain systems.

One alternative is to use an MHIL test method. In this test method, a real-time simulation of the system is combined with a dynamometer test bench. This method has been utilized in the literature for testing the electric drivetrain and control strategies for single-motor drivetrain systems [31] - [35]. However, to utilize this method for multi-motor drivetrain systems, one drivetrain is implemented in the dyno test bench while the remaining are simulated using a real-time simulator [36]. By including the remaining drivetrains in the real-time simulation, multi-motor drivetrain components and control methods can be tested less expensively.

Very few works are found in the literature adapting the MHIL method to verify multi-motor drivetrain systems [36]. In [36], the authors have used look-up tables-based efficiency maps to represent the electric machine in real-time simulation. Therefore, the dynamics of the electrical machine are not included. In addition, most of the reviewed work has used vehicle models without considering multi-body vehicle dynamics in real-time simulation which provide limited verification capabilities [31] - [37]. Furthermore, the interface between the real-time simulation and the dyno test bench has not been discussed in detail in the reviewed literature [33], [35], [36]. Therefore, there is a clear gap in the literature regarding the design of an MHIL test bench for a multi-motor drivetrain system that utilizes a high-fidelity vehicle model and a dynamic electric machine model.

1.2 Contributions of the study

This thesis work aims to advance the research on distributed electric drivetrain design, modeling, and verification. The distributed drivetrain has been extensively studied in the literature. However, conceptualizing a standardized drivetrain for BEVs is lacking in the reviewed literature. In addition, alternative methods of drivetrain system verifications can lead to reduced cost and faster industrialization. The main contributions of this study are summarized as follows.

- A standardized drivetrain for passenger BEVs has been conceptualized. A method is proposed to dimension the torque and power of the standardized drivetrain. The

performance requirements of four passenger BEV models are used to estimate the torque and power of the standardized drivetrain. This method ensures that the performance requirements of a wide range of passenger vehicles can be met when implementing the standardized drivetrain. The drivetrain performance is analyzed by comparing the four representative vehicle models' WLTC drive cycle energy consumption by implementing a system model of the complete vehicle in PLECS/Simulink.

- A PHIL test bench is designed, prototyped, and experimentally evaluated to verify a traction inverter. The proposed test bench can be flexible and cheaper since the VSC used as IUT is utilized inside the emulator. Therefore, verifying VSCs with different ratings would only require prototyping a suitable coupling network. The machine emulator performance is compared to simulations and experimental measurements of an equivalent electric machine. The emulator is controlled using an open-loop control method whose accuracy depends on the accurate estimation of the coupling network and the machine parameters. Compared to simulations of the equivalent machine, the machine emulators' experimental results have a minor error than experimental results from the dyno test bench.
- An analytical formulation of the machine emulator operating region in a back-to-back PHIL test bench is presented. The machine emulator and the test inverter share the same DC link in such a test bench, limiting the operating boundary depending on the coupling network inductance dimension. Therefore, an analytical method is proposed to dimension the coupling network inductance to utilize the maximum operating bandwidth of the emulator. Furthermore, the design three-phase transformed for a high bandwidth emulator maximum operating frequency of 800 Hz is proposed. Finally, simulations are performed for a 60-kW machine emulator to verify the operating boundary of the proposed high bandwidth emulator. Simulation results show that the emulator can reach the same operating points as the representative machine over the entire operating frequency.
- An MHIL test bench for distributed drivetrains is prototyped and experimentally verified. The real-time simulation of a vehicle with two independently driven front wheels is interfaced to a dynamometer test bench with two identical 60-kW PMSMs. Detailed analysis and experimental evaluation of two different interfacing strategies to combine the real-time simulation with the dyno test bench are presented.

1.3 Publications

- [1] **N. Sharma**, B. Jiang, A. Rodionov, and Y. Liu, "A Mechanical-Hardware-in-the-Loop Test Bench for Verification of Multi-Motor Drivetrain Systems," in *IEEE Transactions on Transportation Electrification*, 2022, doi: 10.1109/TTE.2022.3191411 [Early access].
- [2] **N. Sharma**, G. Mademlis, Y. Liu and J. Tang, "Evaluation of Operating Range of a Machine Emulator for a Back-to-Back Power-Hardware-in-the-Loop Test Bench," in *IEEE Transactions on Industrial Electronics*, vol. 69, no. 10, pp. 9783-9792, Oct. 2022, doi: 10.1109/TIE.2022.3142421.
- [3] G. Mademlis, **N. Sharma**, Y. Liu, and J. Tang, "Zero-Sequence Current Reduction Technique for Electrical Machine Emulators with DC-Coupling by Regulating the SVM

- Zero States," in *IEEE Transactions on Industrial Electronics*, vol. 69, no. 11, pp. 10947-10957, Nov. 2022, doi: 10.1109/TIE.2021.3120485.
- [4] B. Jiang, **N. Sharma**, Y. Liu, C. Li, and X. Huang, "Real-Time FPGA/CPU-Based Simulation of a Full-Electric Vehicle Integrated with a High-Fidelity Electric Drive Model," *Energies*, vol. 15, no. 5, p. 1824, Mar.
 - [5] B. Jiang, **N. Sharma**, Y. Liu, and C. Li, "Acceleration-based wheel slip control realized with decentralised electric drivetrain systems," *IET Electrical Systems in Transportation*, vol. 12, no. 2, Mar pp. 143-152, 2022.
 - [6] G. Mademlis, R. Orbay, Y. Liu, **N. Sharma**, R. Arvidsson, T. Thiringer, "Multidisciplinary cooling design tool for electric vehicle SiC inverters utilizing transient 3D-CFD computations", *eTransportation*, Volume 7, 2021, 100092, ISSN 2590-1168.
 - [7] **N. Sharma**, Y. Liu, G. Mademlis and X. Huang, "Design of a Power Hardware-in-the-Loop Test Bench for a Traction Permanent Magnet Synchronous Machine Drive," *2020 International Conference on Electrical Machines (ICEM)*, 2020, pp. 1765-1771.
 - [8] G. Mademlis, Y. Liu, J. Tang, L. Boscaglia and **N. Sharma**, "Performance Evaluation of Electrically Excited Synchronous Machine compared to PMSM for High-Power Traction Drives," *2020 International Conference on Electrical Machines (ICEM)*, 2020, pp. 1793-1799.
 - [9] J. Tang, Y. Liu, and **N. Sharma**, "Modeling and Experimental Verification of High-Frequency Inductive Brushless Exciter for Electrically Excited Synchronous Machines," in *IEEE Transactions on Industry Applications*, vol. 55, no. 5, pp. 4613-4623, Sept.-Oct. 2019.
 - [10] **N. Sharma** and Y. Liu, "Multiple electrical machines applied for high drive train efficiency," *2018 IEEE International Conference on Electrical Systems for Aircraft, Railway, Ship Propulsion and Road Vehicles & International Transportation Electrification Conference (ESARS-ITEC)*, 2018, pp. 1-7.

Chapter 2

Conceptualization of a Standardized

Drivetrain for BEVs

In this chapter, a standardized drivetrain is conceptualized and evaluated using simulations. First, a vehicle classification is derived, and four representative BEVs are selected. Next, the performance specifications of these vehicles are used to define the torque and power requirements of a standardized electric machine. Finally, simulations are performed with the WLTC drive cycle using system models of the BEVs implemented in PLECS/Simulink.

2.1 Vehicle classification

In the literature, various classification methodologies for electric passenger vehicles can be found [38] [39]. In [38], BEVs are classified as city, highway, and sports based on their performance requirements, e.g., top speed, acceleration, gradability, driving range, and curb weight. Furthermore, in [39], vehicles are classified into four categories: small, medium-large, high performance, and sport. A similar categorization is also done in this work with a slightly different methodology. First, the specification data of conventional internal combustion engine-based vehicles (ICEVs) are analyzed to define the different vehicle classes. Afterward, the classification is expanded to BEVs. The goal of the classification is to enable the selection of representative BEV models. The parameters of these models will be used later to dimension the torque and power requirements of the standardized drivetrain.

2.1.1 Classification of ICEVs

The specification data for the top-selling vehicle models in Europe for 2017 are analyzed to classify the vehicles [40]. The primary data points used in the classification are curb weight, top speed, and acceleration since these parameters influence the power and torque requirements of the powertrain [38], [39], [41]. All the data for the selected models were obtained for the United Kingdom market to ensure uniformity and because the information is available in English. The selected vehicle models are ICEVs. Each model has several variants with different performance specifications depending on fuel type, maximum power output, type of transmission, number of gear reduction stages, and vehicle dimensions. Therefore, it is necessary to define a base variant to analyze the vehicle models' specifications across manufacturers. Therefore, the base variant is defined as the one with a petrol engine with the lowest power output, a manual transmission with minimum speed reduction stages, and the smallest overall length. The data of the base variant of the selected vehicle models collected from the manufacturer's website and brochure are presented in Appendix 1.

The vehicle models are classified into four segments: light vehicle, C class, D class, and performance vehicles in increasing order of vehicle mass and size. The vehicle classification is summarized in Table 2-1 based on 42 ICEVs. The specification range is defined to enclose the data points used in the analysis with some approximation, e.g., in the case of overall length, the lowest value is rounded down while the highest is rounded up. In the case of performance vehicles, the lowest specification is used. It can be observed that the definition of light vehicle and C class are mutually exclusive with minimal overlap. On the other hand, the C and D class vehicles have similar top speed and acceleration performance. However, the D class vehicles are, in comparison, longer and heavier. The significant overlap in curb weight indicates that the overall length could be a differentiating factor between the C class and D class vehicles. Finally, the performance vehicles have the best acceleration and top speed performance.

The overall length, top speed, and acceleration (0 – 100 km/h) data of the ICEVs are presented in Figure 2-1, Figure 2-2, and Figure 2-3, respectively. It can be observed from Figure 2-1 that, on average, the light vehicles have the smallest length and lowest curb weight, with average length and curb weight around 4000 mm and 1000 kg, respectively. On the other hand, the C class vehicles are slightly longer and heavier, with average length and curb weight around 4300 mm and 1250 kg, respectively. Similarly, D class vehicles are, on average, longer, around 4500 mm, and heavier, 1400 kg compared to C class vehicles. Furthermore, performance vehicles' average length and curb weight are around 4650 mm and 1600 kg, respectively.

With some exceptions, a clear distinction could also be made between the Light and C class vehicles in terms of acceleration and top speed performance, as seen in Figure 2-2 and Figure 2-3, respectively. The time to accelerate from 0 to 100 km/h for the light and C class vehicles in Figure 2-2 is, on average, around 14 sec and 11 sec, respectively. Similarly, on average, the top speed of light and C class vehicles in Figure 2-3 around 160 km/h and 190 km/h, respectively. However, the difference between the C and D class vehicles is unclear when comparing acceleration and top speed performance. Both vehicle segments have an average acceleration time of around 11 sec and a top speed of around 190 km/h. The performance vehicles have the highest top speed and fastest acceleration capability. Although the performance vehicles have too few data points in the collected sample, they could be expected to occupy the bottom right corner in Figure 2-2 and the top right corner in Figure 2-3. The average top speed of the performance vehicle is around 230 km/h, and the average acceleration time is around 7.4 sec.

Table 2-1: Passenger vehicle segment definition for ICEVs

Vehicle segment	Overall length (mm)	Curb weight (kg)	Top speed (km/h)	Acceleration in sec (0 – 100 km/h)
Light vehicle	3550 – 4200	850 – 1200	155 – 175	12,5 – 16
C class	4200 – 4450	1100 – 1400	170 – 210	8,5 – 13
D class	4400 – 4800	1300 – 1600	180 – 210	8,5 – 13
Performance	> 4650	>1450	>220	< 7,5

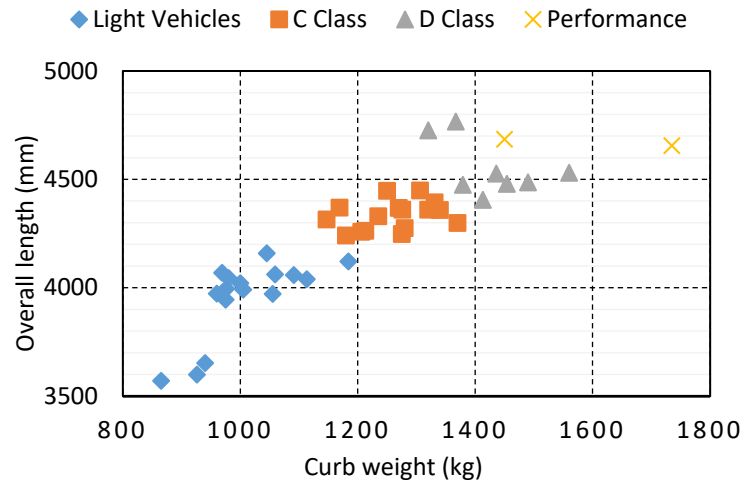


Figure 2-1: Overall length of selected ICEV models as a function of curb weight

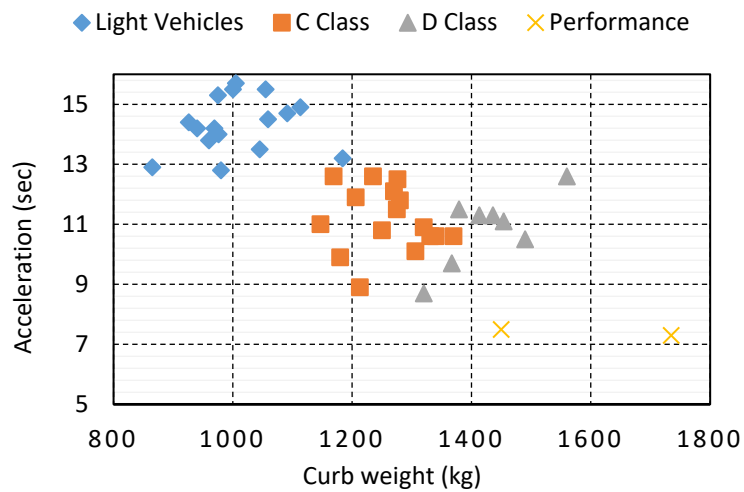


Figure 2-2: 0 – 100 km/h acceleration time of the selected ICEV models as a function of curb weight

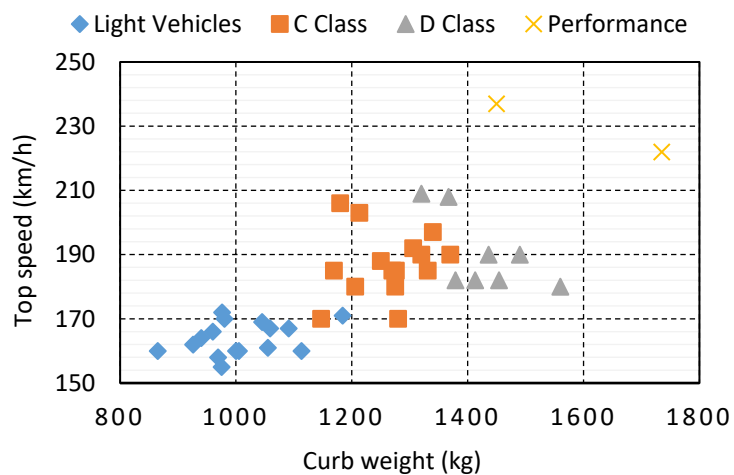


Figure 2-3: Top speed of the selected ICEV models as a function of curb weight

2.1.2 Classification of BEVs

The number of BEVs in the market at the time of the study was limited to 19 models, which makes it difficult to classify them using the available data [39]. Therefore, instead of analyzing the available BEVs to derive a vehicle classification, the specifications of a few BEVs are compared to their respective ICEV variant, e.g., Volkswagen e-golf, Volkswagen e-up!, Ford focus electric hatch. As expected, the overall length of BEV models is observed to be the same as for the ICEV variant. However, the curb weight is almost 200 to 300 kg higher for the corresponding BEV versions of the studied models. Based on the above observations, the vehicle classification of ICEVs is adapted to BEVs by adjusting the curb weight range, i.e., the lowest value is increased by 200 kg and the highest value by 300 kg. The weight data is then used to group the available BEVs to derive the range of top speed and acceleration performance for the defined vehicle segments.

The overall length of the BEVs analyzed is presented w.r.t curb weight Figure 2-4. From the figure, it can be observed that almost half of the BEVs have a shorter length than specified in Table 2-2. On the other hand, they fit the curb weight range with just one exception. Therefore, the overall length range is lowered for light vehicles, C and D class, by 100 mm and performance vehicles by 550 mm. The analyzed vehicles' acceleration and top speed performance data are presented in Figure 2-5 and Figure 2-6, respectively. It can be observed from the figures that the light vehicles have an average acceleration time of 11 sec and a top speed of 135 km/h. In contrast to ICEVs, the C class and D class vehicles have more significant differences in BEVs' top speed and acceleration performance. For example, the average acceleration time is 9 sec and 7 sec, respectively. Similarly, the average top speeds are 150 km/h and 175 km/h. In line with ICEVs, the performance vehicles have the highest top speeds and the lowest acceleration time for BEVs.

The vehicle segment definitions are updated after analyzing the available BEVs' acceleration and top speed performance and are summarized in Table 2-2. Comparing Table 2-1 and Table 2-2, it can be observed that the BEVs, on average, have a lower 0 to 100 km/h acceleration time. The reason is the faster dynamic response of electric machines compared to combustion engines. However, the top speed of BEVs except the performance vehicles are on average lower. The lower top speed in BEVs could be due to the single-speed transmission compared to a multi-speed transmission used in ICEVs. It should be noted that with the development of the high-speed electric machine, the top speed of future BEVs may become like the ICEVs. In

Table 2-2: Passenger vehicle segment definition for BEVs

Vehicle segment	Overall length (mm)	Curb weight (kg)	Top speed (km/h)	Acceleration in sec (0 – 100 km/h)
Light vehicle	3450 – 4200	1050 – 1500	120 – 135	12 – 13,5
C class	4100 – 4450	1300 – 1700	135 – 165	6,5 – 11,5
D class	4300 – 4800	1500 – 1900	160 – 210	5,5 - 8
Performance	> 4100	>1650	>220	< 5,5

addition, improvements in Li-ion battery energy density could lead to reduction in the curb weight. Therefore, the vehicle segment definitions of BEVs could be very similar to ICEVs in

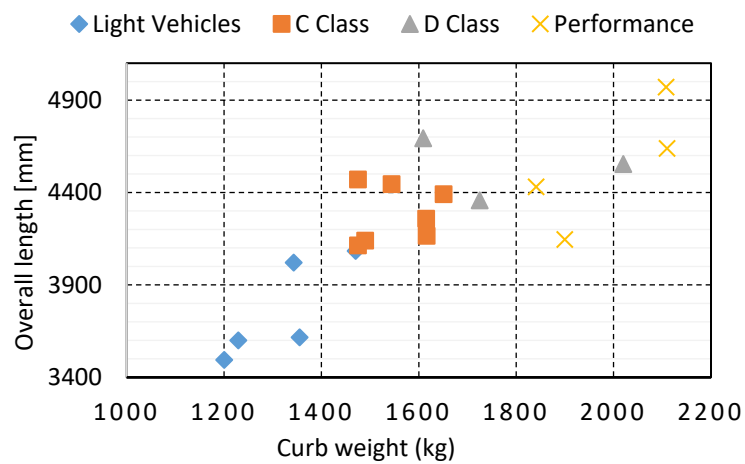


Figure 2-4: Overall length of selected BEV models as a function of curb weight

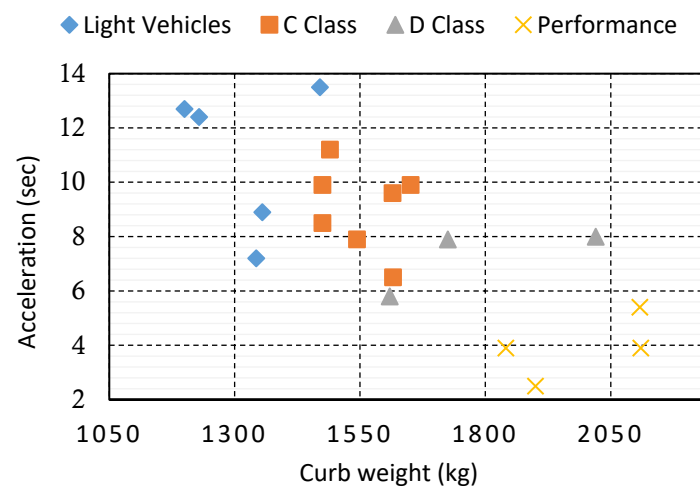


Figure 2-5: 0 – 100 km/h acceleration time of the selected BEV models as a function of curb weight

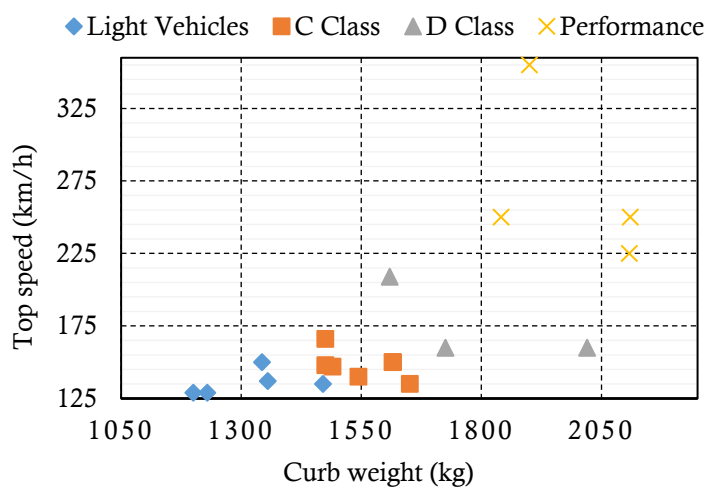


Figure 2-6: Top speed of the selected BEV models as a function of curb weight

future in terms of curb weight and top speed.

2.2 Wheel torque and power analysis

The maximum power and torque of the analyzed BEVs could be used to define the requirements of the standardized drivetrain. However, considering the limited number of available BEV models, the results may be inaccurate. Therefore, traction torque and power on the wheels are estimated by utilizing the performance specifications of four representatives BEVs. The vehicle classification presented earlier in Table 2-2 is used to define a representative model for each of the four passenger vehicle segments.

The resistive force exerted on the vehicle by the road during the longitudinal motion of the vehicle can be estimated as

$$F_r = \frac{1}{2} \rho C_d A v^2 + m g \sin \alpha + m g C_r \quad (2-1)$$

where m is the vehicle mass; v is vehicle speed; ρ is the air density; C_d is aero-dynamic drag co-efficient; A is the effective cross-section area of the vehicle; C_r is rolling resistance co-efficient; g is the acceleration due to gravity; α is the road gradient angle. The traction force can be estimated as

$$F_t = F_r + m \frac{dv}{dt} \quad (2-2)$$

The traction torque and power on the wheel can be obtained as

$$T_w = F_t r_w \quad ; \quad P_w = F_t v \quad (2-3)$$

where r_w is the wheel radius.

The selected BEV models are based on existing vehicles in the market, and their most important parameters are presented in Table 2-3. The manufacturer's specification is used for dimensional and performance details, including length, width, height, mass, top speed, and acceleration times. However, manufacturers usually do not mention the aerodynamic drag and the effective cross-section areas. Other sources, e.g., literature, and online articles, estimate these specifications. The value of rolling resistance co-efficient is assumed according to [38]. The light and C class vehicles are assumed to have low rolling resistance tires with a co-efficient 0.009 corresponding to the top speed. However, the D class and performance vehicles with higher top speed are expected to have tires with a high rolling resistance coefficient of 0.012. The wheel diameter is estimated from the tire specification using the method specified in [39]. In the case of performance vehicles, the top speed specification is lower than the representative model. The requirement can be met by increasing the electric machine maximum speed or reducing the gear ratio. These solutions will result in two extreme requirements on electric machine size. The top speed in gradient is defined using UNECE guidelines for Trans-European North-South Motorway. 4% and 6% gradients are considered,

Table 2-3: Specifications of the representative vehicle models

Vehicle parameters	Light vehicle	C Class	D Class	Performance
	Renault Zoe	Nissan Leaf	Tesla Model 3	Tesla Model S
Length (mm)	4084	4445	4694	4970
Width excluding mirrors (mm)	1730	1770	1933	1964
Unladen height (mm)	1562	1550	1443	1445
Wheelbase length (mm)	2588	2700	2875	2960
Average track width (mm)	1511	1537	1580	1681
Wheel diameter (m)	0,622	0,632	0,67	0,7
Curb weight (kg)	1470	1544	1609	2108
Top speed (km/h)	135	150	180	220
Acceleration in sec (0 – 100 km/h)	13,5	7,9	5,8	5
Aero Dynamic Drag Coefficient	0,29	0,29	0,24	0,24
Effective Cross Section for Drag	2,38	2,27	2,23	2,34
Tire Rolling Resistance	0,009	0,009	0,012	0,012
Uphill driving (km/h, %)	120, 4%	120, 4%	120, 4%	120, 4%
Uphill driving (km/h, %)	80, 6%	80, 6%	80, 6%	80, 6%

and the corresponding vehicle speed is obtained from [42]. The requirements are identical for all vehicles to make a uniform comparison.

The following assumptions are used when estimating the wheel torque:

- I. The vehicle mass of one driver (68 kg) and luggage (7kg) is added to the curb weight when estimating the wheel torque for acceleration requirement.
- II. When estimating the wheel torque for driving on a flat road and uphill, the vehicle mass is calculated by adding one driver (68 kg), four passengers (68 kg each), and luggage (7 kg).
- III. It is assumed that the constant power speed range of the drivetrain is 3. For example, in the case of a light vehicle with a top speed of 135 km/h, the torque produced by the drivetrain is constant till 45 km/h. After 45 km/h, the drivetrain power is assumed to be constant.

The estimated wheel torques of the light, C class, D class, and performance vehicles are presented in Figure 2-7, Figure 2-8, Figure 2-9, and Figure 2-10, respectively. The blue line in the figures shows the required wheel torque needed to drive the vehicle on a flat road. Since the rolling resistance is assumed to be constant, the line starts above zero. The wheel torque needed to drive at the top speed is shown by a data tip, e.g., in the case of a light vehicle, the wheel torque needed to drive at a top speed of 135 km/h is 235,5 Nm, as shown in Figure 2-7.

Similarly, the wheel torques needed to drive at various vehicle speeds on a 4% and 6% gradient are indicated by black and green lines in the figures, respectively. Since it is assumed that the vehicle is driving uphill, the traction force due to the gradient is always positive. These wheel torque requirements on flat roads and gradients are referred to as road load as they represent the resistive force exerted on the vehicle by the road. The road load on a flat road, mainly dominated by the aerodynamic drag, is highest for light vehicles and lowest for D class passenger vehicles at the same speed because the aerodynamic drag force depends on the product of aerodynamic drag co-efficient and the effective cross-section, which is highest for light vehicles and minimum for D class passenger vehicles. The red line represents the wheel torque requirement for accelerating the vehicle.

The maximum wheel power required to fulfill the various performance requirements are summarized in Table 2-4. The acceleration performance defines the maximum power requirement. In the case of light and C class vehicles, the top speed on a 4% gradient is more demanding in terms of maximum wheel power compared to the top speed on a flat road or a

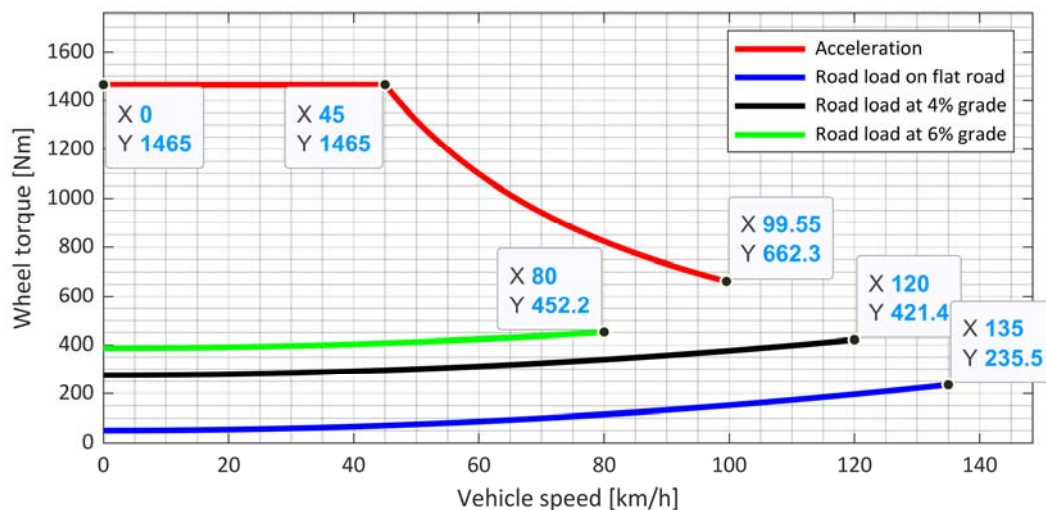


Figure 2-7: Wheel torque requirements of light passenger vehicle

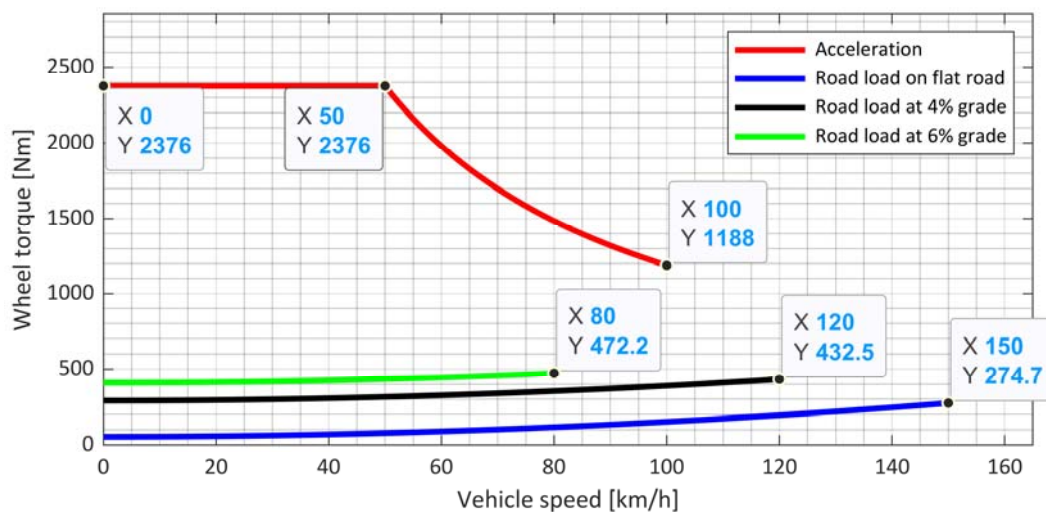


Figure 2-8: Wheel torque requirements of C class passenger vehicle

6% gradient. However, in the case of D class and performance vehicles, the top speed on a flat road demands more wheel power than the top speed on a slope. The reason is that the top speed of D class and performance vehicles on a flat road is 1.5 times and almost two times compared to the top speed requirement for 4% gradient, respectively. Therefore, the

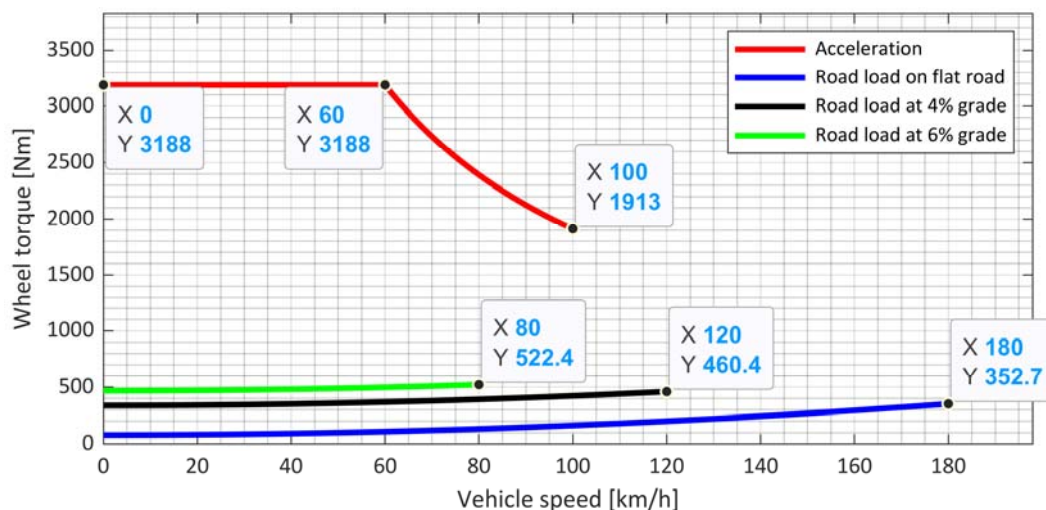


Figure 2-9: Wheel torque requirements of D class passenger vehicle

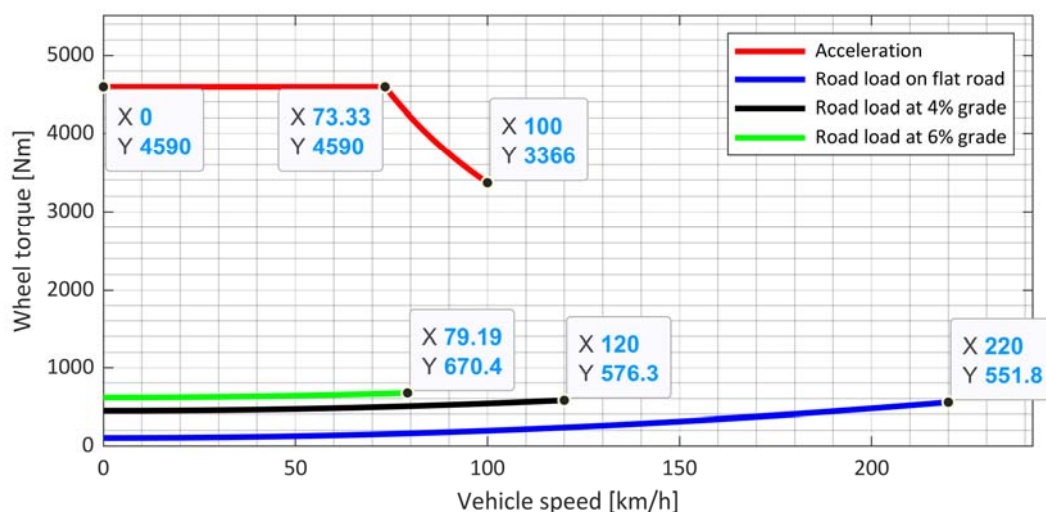


Figure 2-10: Wheel torque requirements of performance vehicle

Table 2-4: Maximum wheel power requirement for the BEVs in kW

Requirements	Light vehicle	C Class	D Class	Performance
0 – 100 km/h acceleration	58,9	104,4	158,6	267,1
Top speed on flat road	28,4	36,2	52,6	96,3
Top speed on 4% gradient	45,2	45,6	45,8	54,9
Top speed on 6% gradient	32,3	33,2	34,7	42,6

maximum wheel power will have a much more significant contribution from aerodynamic drag, which is a quadratic function of vehicle speed.

On the other hand, for light and C class vehicles, the top speed on a flat road is quite close to the top speed on a 4% gradient. Therefore, the gradient force will significantly influence the maximum wheel power requirements. Therefore, it can be concluded that the acceleration performance will determine the vehicles' short-term power or peak power requirements. The long-term or continuous power requirements will come from the top speed requirements on flat roads and gradients.

2.3 Electric machine torque and power requirements

The wheel torque and power analysis presented earlier can be used to obtain the electric machine torque requirements. Additionally, the final gear ratio of the transmission and the number of drivetrain units for each segment should be defined. The following assumptions are made when estimating the electric machine torque:

- I. It is advantageous to have a compact drivetrain to utilize the distributed drive architecture. One way it can be achieved is by reducing the size of the electric machine. Increasing the rotational speed of the electric machine while keeping the same power will result in a lower torque requirement, resulting in a smaller size; the diameter and length of the machine are proportional to the torque. Therefore, the maximum speed of the electric machine is assumed to be 20000 rpm
- II. Transmission efficiency is set to 97%. The gear ratios are determined such that the maximum speed of the electric machine is reached at vehicle top speeds and are presented in Table 2-5.
- III. The peak wheel power requirement for the different vehicle segments summarized in Table 2-4 can be expressed as multiples of the light vehicle requirements. Therefore, the peak power of the electric machine is defined considering the light vehicle requirement. In addition, the number of drivetrain units for the different vehicle segments is defined as presented in Table 2-5.

Using the above assumptions and the wheel torque estimated earlier from the acceleration performance, the electric machine torque required to meet the performance requirement of the vehicles are obtained and are shown together in Figure 2-11. The torque is highest for performance vehicle followed by light, C class and D class vehicles. The peak torque requirement of the electric machine in the standardized drivetrain is then defined to enclose the requirement of all the vehicles. It is shown in the figure as a dotted line. The peak torque is defined. In the low-speed region, the peak torque is equal to the light vehicle requirements.

Table 2-5: Number of drivetrain units and gear ratio of transmission for different vehicle segments

Requirements	Light vehicle	C Class	D Class	Performance
Number of drivetrain units	1	2	3	4
Gear ratio	15.9	14.1	14.1	12.1

The peak power is defined considering performance vehicle requirements up to the speed of 9400 rev/min. After this speed, the peak power requirements are defined considering the light vehicles. Since, the acceleration performances of the vehicles are not defined, the peak torque requirements at higher speeds are undefined. However, it can be defined by allowing a gradual reduction in peak power such that at the maximum speed of the machine, the peak and continuous powers are the same.

The required torque of the electric machine for driving on a flat road and gradients for the different vehicles are shown in Figure 2-12, Figure 2-13, and Figure 2-14. These are used to dimension the electric machine's continuous, shown as a dotted line in the figures. It can be observed from Figure 2-12 that the torque required to drive on a flat road is highest for light passenger vehicles, followed by C class, performance, and D class vehicles. A similar trend can be observed in Figure 2-13 and Figure 2-14 as well. The continuous torque requirements at lower speed are given by road load for driving uphill on a 6% gradient, at medium speed by road load for driving uphill on a 4% gradient and at high rotational speed by road load for

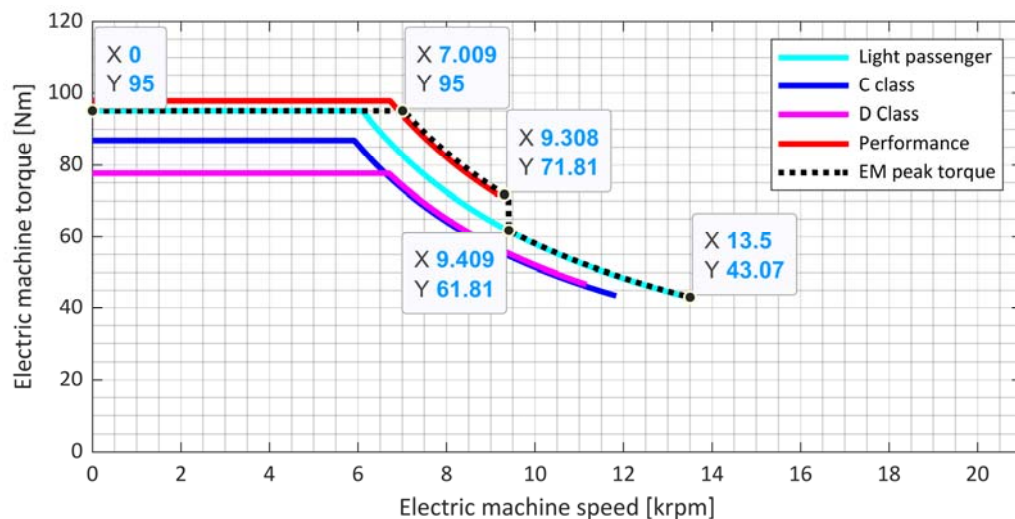


Figure 2-11: Peak electric machine torque needed to meet the vehicle requirements

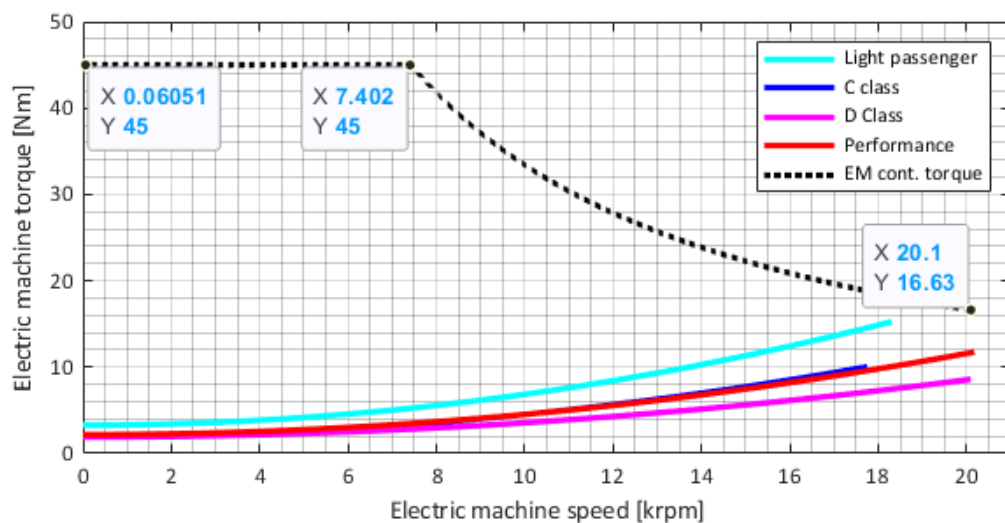


Figure 2-12: Required continuous torque for driving on flat road

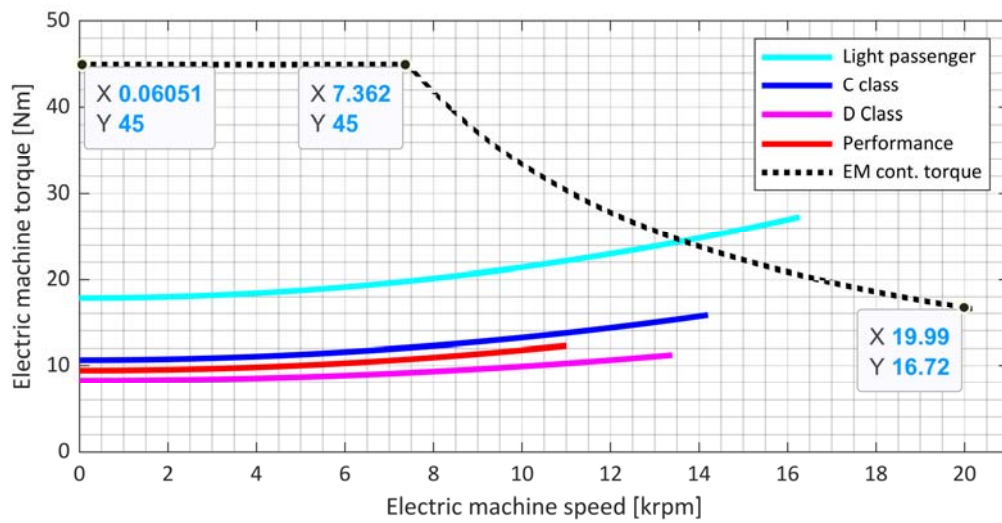


Figure 2-13: Required continuous torque for driving uphill on 4% gradient

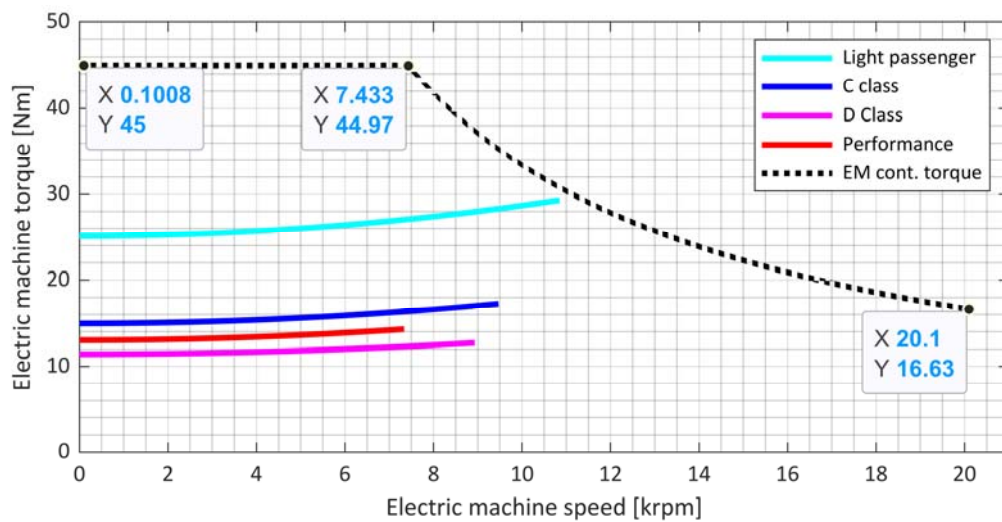


Figure 2-14: Required continuous torque for driving uphill on 6% gradient

driving on a flat road. It can be observed in Figure 2-13 that the selected continuous torque is insufficient to meet the road load for driving uphill on a 4% gradient for the light passenger vehicle. The maximum power required to meet the road load for driving a light passenger vehicle uphill on a 4% gradient is almost 30% higher than the dimensioned continuous torque. However, increasing the continuous torque to meet this requirement will over-dimension the continuous torque and power for all other vehicles; hence, it is disregarded. In Figure 2-12, the selected continuous torque is higher compared to the road load of driving on flat roads for all passenger vehicles. The estimation of road loads is done without considering any crosswinds and assuming that the gearbox efficiency is constant at 97%. Therefore, it may be better to have some buffer between the selected continuous torque and the road load for driving on a flat road. Hence, the continuous torque is slightly higher than the requirements for constant speed driving, except for the light vehicle on a 4% gradient.

2.4 System model

System models of vehicles can be divided mainly into two broad categories depending on the direction of calculation: backward and forward-facing models [43]. A backward-facing model (BFM) starts with the tractive effort required at the wheels and then calculates the required torque of the electric machine in a backward manner. The actual vehicle speed and reference are assumed to be the same in such models. BFMs are commonly used for energy consumption calculations because of their simplicity and faster computations. In addition, drivetrain components are often modeled as efficiency maps. However, since both the mechanical and electrical parameters are assumed to be in a steady state, such models cannot simulate the electrical and mechanical dynamics of the system. Therefore, they are not considered for modeling.

On the other hand, a forward-facing model (FFM) uses a speed controller or drive model to calculate the tractive effort required on the wheels based on the difference between reference and actual vehicle speed. The accuracy and complexity of an FFM can differ quite a lot depending on the level of details. Therefore, a balance between accuracy and simulation time must be achieved using a lumped parameter modeling approach [44] [45]. Nevertheless, control, mechanical and electrical transients can be simulated in sufficient detail. PLECS is chosen as the simulation platform in this work due to its reasonable accuracy in modeling semiconductor losses. The system model consists of models of an electric machine, an inverter, a transmission, and vehicle dynamics.

2.4.1 Electric machine model

Dynamic model of a permanent magnet synchronous machine (PMSM) in dq-frame can be expressed as

$$\begin{bmatrix} u_d \\ u_q \end{bmatrix} = \mathbf{R}_{\text{mat}} \begin{bmatrix} i_d \\ i_q \end{bmatrix} + \mathbf{L}_{\text{mat}} \begin{bmatrix} \frac{di_d}{dt} \\ \frac{di_q}{dt} \end{bmatrix} + \begin{bmatrix} -\omega\psi_q \\ \omega\psi_d \end{bmatrix} \quad (2-4)$$

$$\mathbf{L}_{\text{mat}} = \begin{bmatrix} L_{dd} & L_{dq} \\ L_{qd} & L_{qq} \end{bmatrix}$$

$$\mathbf{R}_{\text{mat}} = \begin{bmatrix} R_s & 0 \\ 0 & R_s \end{bmatrix}$$

where R_s denotes the phase resistance, ω indicates electrical angular speed, ψ_d and ψ_q represents d- and q-axis flux linkages respectively, L_{dd} , L_{qq} , L_{dq} and L_{qd} are incremental inductances, u_d and u_q are d- and q-axis voltage respectively and i_d and i_q are d- and q-axis currents respectively [46]. Some key parameters of the machine used in modeling are presented in Table 2-6. In an electric machine, stator windings are connected in either star or delta. A star connection might be preferred as the phase currents are lower than a delta connection, requiring smaller currents from the inverter. However, the neutral point in a star-connected stator winding of an electric machine is usually not grounded. Therefore, the zero-

sequence current experiences infinite impedance. Hence, in the dq-frame analysis of machines, the zero-sequence component of current can often be neglected.

To acquire, the d- and q-axis flux linkages, a parametric sweep can be performed using finite element method (FEM) analysis on an electromagnetic model of the electric machine. To perform a parametric sweep, there are two ways to select the co-ordinates of stator currents in dq-frame as shown in Figure 2-15. Either, using current amplitude and current angle as variables in which case, the data points will be radially distributed. Or to perform the sweep using d- and q-axis currents as variables resulting into a rectangular distribution. The blue dots represent the selected operating points. As can be observed from the distribution of the operating points, rectangular distribution will be preferred for simplified interpolation of the data. This is because in rectangular distribution, the interpolation space is uniform in the entire operating range, except at the current limit circle. However, in radial distribution the interpolation space is dense close to origin and becomes less dense when moving away from origin.

The d- and q-axis flux linkages of the machine can also be obtained via steady-state measurements as follows

$$\Psi_d = \frac{U_q - R_s I_q}{\omega} \quad (2-5)$$

Table 2-6: Parameters of the PMSM used in system modeling

Parameters	Value	Unit
Number of pole pair	4	
Phase resistance	0.00267	Ω
End winding leakage inductance	1.634×10^{-5}	H
Rotor inertia	0.008775	kgm^2

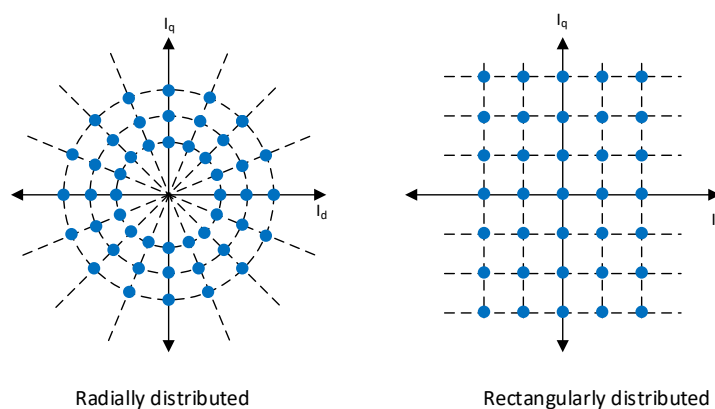


Figure 2-15: Two different methods of selecting co-ordinates of stator currents in dq-frame to calculate flux linkages of electric machine in FEM.

$$\Psi_q = \frac{R_s I_d - U_d}{\omega}$$

where U and I indicates steady-state voltage and currents and Ψ is the steady-state value of flux linkage. If the voltage drops across the switches and cables are neglected, then the controller voltage references can be used instead of voltage measurements [46]. In this work, the FEM analysis approach is used with a rectangular distribution of the variables to obtain the flux linkages as shown in Figure 2-16(a) and (b). The step size of current amplitude is

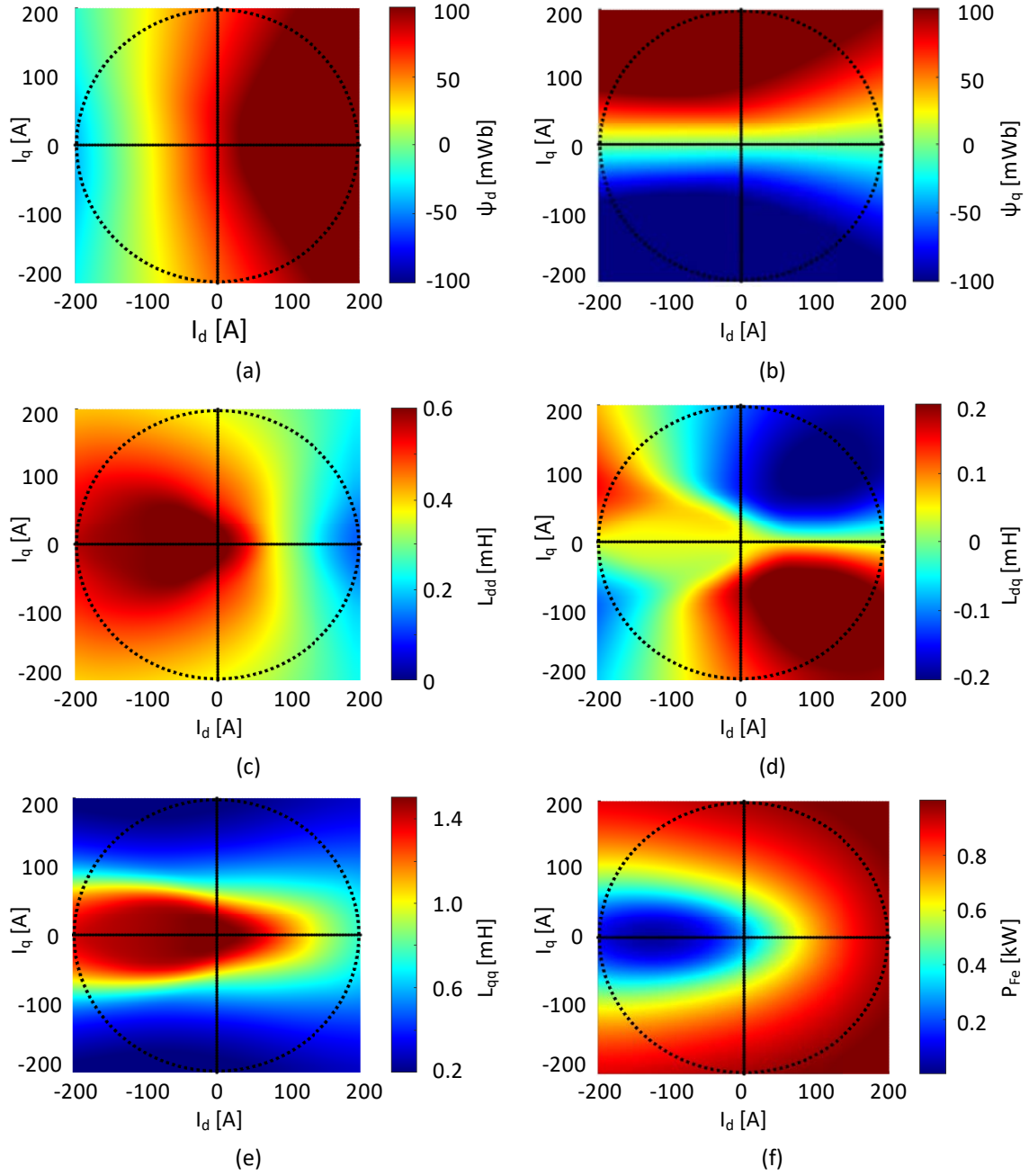


Figure 2-16: Look up tables of the PMSM used for modeling in PLECS. a) d- axis flux linkage, b) q- axis flux linkage, c) d- axis self-inductance, d) q- axis self-inductance e) dq- axis mutual inductance and f) iron core loss at 7000 rev/min

selected to be 5% of the peak currents while performing a parametric sweep. A smaller step size will, of course, result in better interpolation accuracy. However, it will increase the time needed to perform the FEM simulations. The flux linkages will have both fundamental and harmonic components. In this work, the harmonics of the flux linkages are not considered.

The phase resistance can be measured or estimated from the machine geometry. In the case of stranded conductors, the resistance will change with the temperature of the windings. However, this work uses a PMSM with rectangular solid conductors whose resistance will vary with temperature and current frequency through the conductor. Therefore, modeling the temperature dependency of phase resistance will require a coupled thermal model to estimate temperature. On the other hand, the frequency dependencies in the case of rectangular conductors may require performing FEM simulations. Therefore, to simplify the modeling of the machine, the dependency of resistance on temperature and frequency is not considered.

Incremental inductances in (2-4) can be calculated from the flux linkages as

$$\begin{aligned} L_{dd} &= \frac{\partial \psi_d^{(i_d, i_q=\text{constant})}}{\partial i_d} & L_{qq} &= \frac{\partial \psi_q^{(i_d=\text{constant}, i_q)}}{\partial i_q} \\ L_{dq} &= \frac{\partial \psi_d^{(i_d=\text{constant}, i_q)}}{\partial i_q} & L_{qd} &= \frac{\partial \psi_q^{(i_d, i_q=\text{constant})}}{\partial i_d}. \end{aligned} \quad (2-6)$$

Figure 2-16(c)-(e) shows incremental inductances calculated from the flux linkages. It can be observed that the mutual inductance between the d- and q-axis is much smaller compared to the self-inductance of d- and q-axis. Therefore, the mutual inductance in (2-4) can be neglected and the model of the machine can be implemented as an equivalent circuit model, as shown in Figure 2-1. The electromagnetic torque of the PMSM can be calculated as [47]

$$T_e = \frac{3}{2}p(\psi_d i_q - \psi_q i_d) \quad (2-7)$$

where p indicates number of pole-pairs in the rotor. Rotor speed and rotor angle can be expressed as

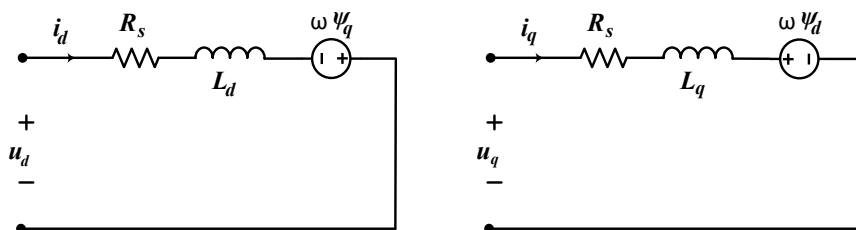


Figure 2-1: Equivalent circuit model of a PMSM in dq-frame neglecting the mutual inductance between d- and q-axis.

$$\frac{d\Omega}{dt} = \frac{T_e - T_L - B\Omega - T_s}{J} \quad (2-8)$$

$$\frac{d\theta}{dt} = \Omega$$

where T_L is the load torque applied on electric machine shaft, B indicates viscous damping co-efficient, T_s is the static friction torque and J indicates rotating inertia.

Iron core losses are also obtained using the FEM simulations and the results are shown in Figure 2-16(f). As shown below, the losses are calculated at a fixed rotor frequency and then scaled at different rotor frequencies

$$P_{Fe}(I_d, I_q, f_2) = \frac{k_h f_2 + k_c f_2^2}{k_h f_1 + k_c f_1^2} P_{Fe}(I_d, I_q, f_1) \quad (2-9)$$

where $P_{Fe}(I_d, I_q, f_1)$ represents the 2-D look-up-table of core losses calculated at rotor frequency f_1 from FEM. k_h and k_c are hysteresis and eddy current coefficients of the iron material and $P_{Fe}(I_d, I_q, f_2)$ is the scaled core loss at rotor frequency f_2 . k_h and k_c are equal to 128 and 0.74 for the core material used in the electric machine. Implementing the iron core losses in the dynamic model will result into an algebraic loop. Therefore, the core losses in PLECS are implemented as a torque loss as follows

$$T_{Fe}(I_d, I_q, f_2) = \frac{P_{Fe}(I_d, I_q, f_2)}{\Omega} \quad (2-10)$$

where $T_{Fe}(I_d, I_q, f_2)$ is the loss torque and Ω is the mechanical speed.

2.4.2 Inverter

A 2-level VSC with SiC MOSFETs is used as the inverter and modeled, as shown in Figure 2-17. The DC-link voltage is 800 V, and the switching frequency is 20 kHz. The switching transients are neglected in modeling the semiconductor switches as they are not the focus. Furthermore, a thermal description is added in PLECS to model the losses of the switches. Switching loss energy is implemented as a look-up table of drain-source current, the voltage across the switch, and junction temperature. The switching loss energy for a junction temperature of 25°C is shown in Figure 2-18(a). It is assumed that the turn-on/off losses are equal since only the total switching loss is of interest. Conduction losses are similarly implemented as a voltage drop across the MOSFETs during conduction. The look-up table of turn-on voltage drop as a function of drain-source current and junction temperature is presented in Figure 2-18(b). The voltage drops for current through the MOSFETs in either direction are assumed to be the same. The switching and conduction losses are average using a periodic impulse and periodic average block, as shown in Figure 2-17. The averaging time is selected to be 1000 times of the switching period.

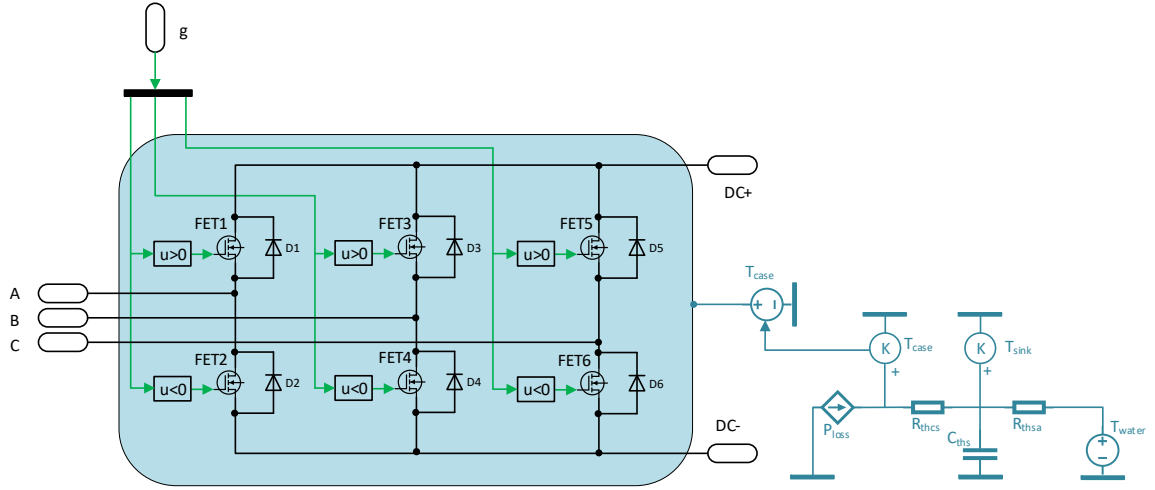


Figure 2-17: Inverter model implemented in PLECS/Simulink

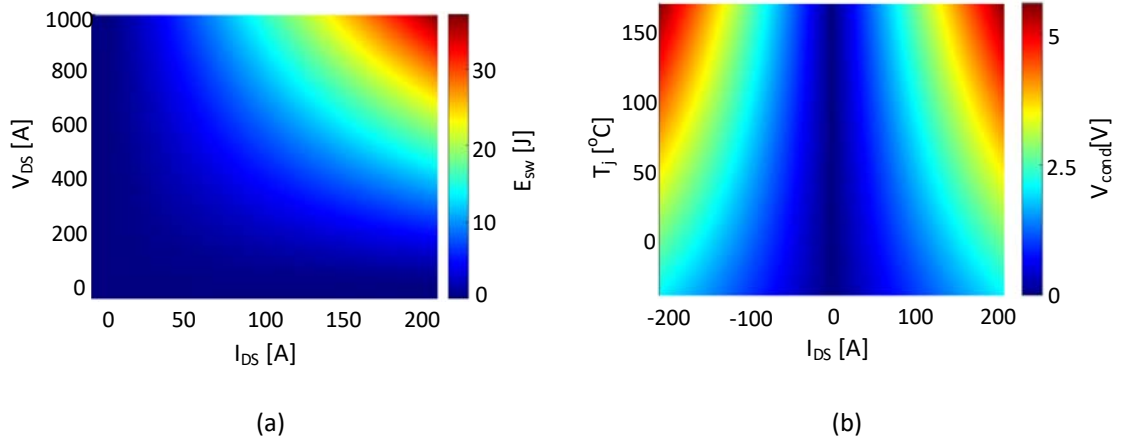


Figure 2-18: Thermal description of the MOSFETs a) switching loss energy b) voltage drop during conduction mode

A four-element-based foster network is used to model the heat transfer from the junction of the MOSFETs to the case. The values used in the modeling are presented in Table 2-7. The averaged losses are used to drive a simplified thermal model representing heat transfer from case to cooling medium (water), as shown in Figure 2-17. R_{thcs} represent the thermal resistance of the grease between the case and the baseplate of the MOSFETs. R_{thsa} represents the thermal resistance between the grease and cooling medium and is calculated as

$$R_{thsa} = \frac{1}{hA} \quad (2-7)$$

where h is heat transfer co-efficient and A is the total surface area of the cooling channel. The heat transfer coefficient depends on the coolant temperature and flow rate. The thermal capacitance of the heat sink C_{ths} is estimated as

Table 2-7: Four element foster network used to model the junction to case thermal network of the MOSFETs

Node	Thermal resistance	Time constant
1 (case)	0.0156	0.00206
2	0.0908	0.0317
3	0.0052	6.52×10^{-5}
4 (junction)	0.0464	0.279

Table 2-8: Reference values of parameters used for thermal model from case to cooling medium

Parameters	Symbol	Values	Unit
Heat transfer co-efficient	h	2279.21	$WK^{-1}m^{-2}$
Total surface area of cooling channel	A	0.0604	m^2
Mass of heat sink	m	1.36	kg
Specific heat capacity	C_p	910	J/K/kg

$$C_{ths} = mC_p \quad (2-8)$$

where m is the heat sink's mass and C_p is the specific heat capacity. A constant temperature source is used to simulate the coolant temperature. Reference values of these parameters are obtained from [48] and are presented in Table 2-8.

2.4.3 Machine control

A cascaded control strategy is used. A speed controller is used in the outer loop and field-oriented control (FOC) of current in the inner loop. The torque demand from the speed controller and rotor speed is used in the current reference calculation block, which contains a look-up-table based current reference in the entire torque-speed range of the machine. The look-up-tables of d- and q-axis currents are calculated using copper loss minimization. The iterative method discussed in [49] is adapted for the PMSM. First, an optimization space is defined around a start point with d- and q-axis currents as coordinates. Then the electromagnetic torque and terminal voltage are calculated from the flux linkage model of the PMSM. It is followed by filtering the result based on torque reference and maximum terminal voltage. Finally, the operating point with the minimum cost is used as a start point for the next iteration. The optimized value is obtained when the optimization space becomes smaller than a given dimension.

The FOC and speed controller gains are selected by shaping the close loop transfer function to be equivalent to a low-pass filter [47]. The speed controller's and FOC's bandwidths are chosen as 15 rad/s and 1500 rad/s, respectively. A sine-pulse width modulator (PWM) with a

third harmonic injection is used to generate gate pulses from the voltage references of FOC. A measurement-processing block is used to process and sample the measurements, and the sampling frequency is chosen as the same as the switching frequency.

2.4.4 Transmission

A high-speed gearbox with three-stage speed reduction is used as transmission. The gearbox is modeled using an ideal gear with the final speed reduction ratio connected to rotating inertia. The inertia is calculated as an equivalent by converting the inertia of each gear stage to the electric machine side. Equivalent inertia referred to the motor side can be calculated as below using the conservation of energy,

$$J_{eq} = J_1 + \frac{(J_2 + J_3)}{k_1^2} + \frac{(J_4 + J_5)}{k_1^2 \cdot k_2^2} + \frac{J_6}{k_{final}^2} \quad (2-9)$$

where J_1 to J_6 and Ω_1 to Ω_6 represent the inertia and angular speed of each gear wheel respectively. k_1 and k_2 are the speed reduction ratio of first and second stage. k_{final} is the total gear ratio with all the three stages. The equivalent inertia and final gear ratio of the gear box are mentioned in Table 2-9. The estimated efficiency of the gearbox is shown in Figure 2-19. On the other hand, the highest efficiency is located around the electric machine's base speed and maximum power operating regions. The loss torque component is obtained from the efficiency map and implemented as a look-up-table to drive a torque source representing

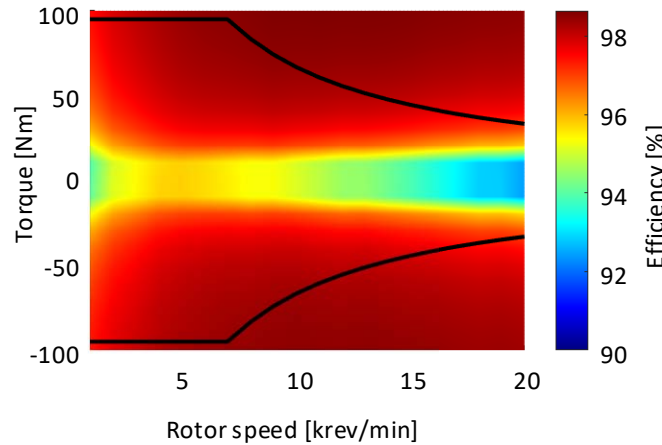


Figure 2-19: Estimated friction torque of gearbox

gear losses in simulation. The torque loss at different speeds and electric machine torques are then interpolated.

2.4.5 Vehicle load

One dimensional vehicle model approximating the vehicle body as a rigid lumped mass around its center of gravity can be used to calculate the force on the wheel [38]. The force on the vehicle's center of gravity is estimated using (2-1). It is converted to torque and used as a

Table 2-9: Parameters used in the modelling of gear box and road load

Parameters	Symbol	Values	Unit
Equivalent inertia of the gear box	J_{eq}	8.2448×10^{-4}	kgm^2
Final gear ratio	k_{final}	14.0517	
Mass of one wheel	m_w	20	kg
Mass of drive shaft	m_{shaft}	6	kg
Radius of drive shaft	r_{shaft}	30	mm

controllable torque source reference. The linear vehicle speed is calculated using the wheel rotational speed, neglecting wheel slip. The traction force required to accelerate the vehicle is implemented by converting linear to rotational motion and using an inertia load. The rotational equivalent of linear inertia of a vehicle is estimated as

$$J_v = m \cdot r_w^2 \quad (2-11)$$

The inertia of the wheel and drive shaft is then added to calculate total inertia on the drive shaft.

$$J_{wheel} = 2 \cdot m_w \cdot r_w^2 \quad (2-12)$$

$$J_{shaft} = m_{shaft} \cdot r_{shaft}^2$$

where J_{wheel} is inertia of all four wheels combined, m_w is mass of each wheel, J_{shaft} is the total inertia of two drive shafts, m_{shaft} is mass of each shaft and r_{shaft} is radius of the shaft. The same shaft inertia is used for all four vehicles in the simulations. On the other hand, the wheel inertia varies due to the differences in wheel radius, while the wheel mass is the same for all four vehicles. The key parameters used to model the vehicle load in the simulation are listed in Table 2-9.

2.5 Drive cycle analysis

Drive cycle simulations using worldwide harmonized light vehicles test cycles (WLTC) are performed to estimate the operating efficiency of the drivetrain in real-world driving. Fixed time step simulations with a step size of $1 \mu\text{s}$ are used, which results in a total simulation time of approximately 32 hours. The complete drive cycle is divided into four parts and the results of each parts are shown separately in Figure 2-20 to Figure 2-23 for the light vehicle. In the figures, six subplots are shown. The first subplot from the top presents the vehicle's reference and actual linear speeds. It is followed by electromagnetic torque on the electric machine shaft and road load in the second subplot. The third shows copper and iron-core losses of the electric machine. The losses of the inverter – conduction and switching – and junction

temperature of the semiconductor are shown in the fourth subplot. The fifth plot presents the transmission losses. Finally, the efficiency of the entire drivetrain is presented in the sixth subplot.

It can be observed from the first subplot in all the four figures that the speed controller does an excellent job in following the speed reference of the drive cycle. The maximum error between the reference and actual speed is less than ± 0.5 km/h. As seen in Figure 2-20, the vehicle's maximum speed is less than 60 km/h during the drive cycle. This drive cycle is referred to as the WLTC low drive cycle and is characterized by frequent accelerations and braking. During WLTC medium drive cycle shown in Figure 2-21, the maximum speed is less than 80 km/h. This drive cycle also simulates frequent acceleration and braking of the vehicle like WLTC low. However, the average speed of the vehicle is higher. In the WLTC high drive cycle shown in Figure 2-22, the vehicle's maximum speed reaches 100 km/h. In this drive cycle there are fewer acceleration and braking scenarios. In addition, the acceleration and braking scenarios are more gradual. The WLTC extra high drive cycle shown in Figure 2-23 is characterized by slower acceleration and braking. This drive cycle has the highest average speed among the four vehicles. During this drive cycle, the vehicle reaches a maximum speed of 130 km/h.

The electromagnetic torque of the electric machine is calculated considering full regenerative braking in the simulations, i.e., the braking torque is provided entirely by the electric machine without assistance from mechanical brakes. It can be observed from the figures that the maximum electromagnetic torque during acceleration is between 80 to 90% of the peak torque for the WLTC low, medium, and high drive cycles. On the other hand, during braking, the maximum electromagnetic torque is around 50% of the peak torque. Furthermore, the road load is a fraction of the electromagnetic torque during all four drive cycles except during the middle period of WLTC high and extra high drive cycles. Therefore, the primary torque demand comes from the acceleration and braking of the vehicle.

In the electric machine, copper losses dominate at low speed, whereas iron-core losses dominate at medium to high speed. From (2-9), it can be observed that the iron-core losses are dependent on frequency. Since the fundamental frequency of the current will increase with speed, iron-core losses will also increase with speed. The copper losses are proportional to the square of the current amplitude. The torque is proportional to the current, as seen in (2-7). Hence, the copper losses are proportional to torque. Therefore, to optimize operating efficiency of electric machines for low-speed and high-speed driving, copper and iron-core losses should be given priority respectively. The switching losses of inverter are higher compared to conduction losses. In addition, junction temperature of the SiC MOSFETs varies between 65° to 85° C for the entire drive cycle. The transmission losses increase with speed like observed in Figure 2-19.

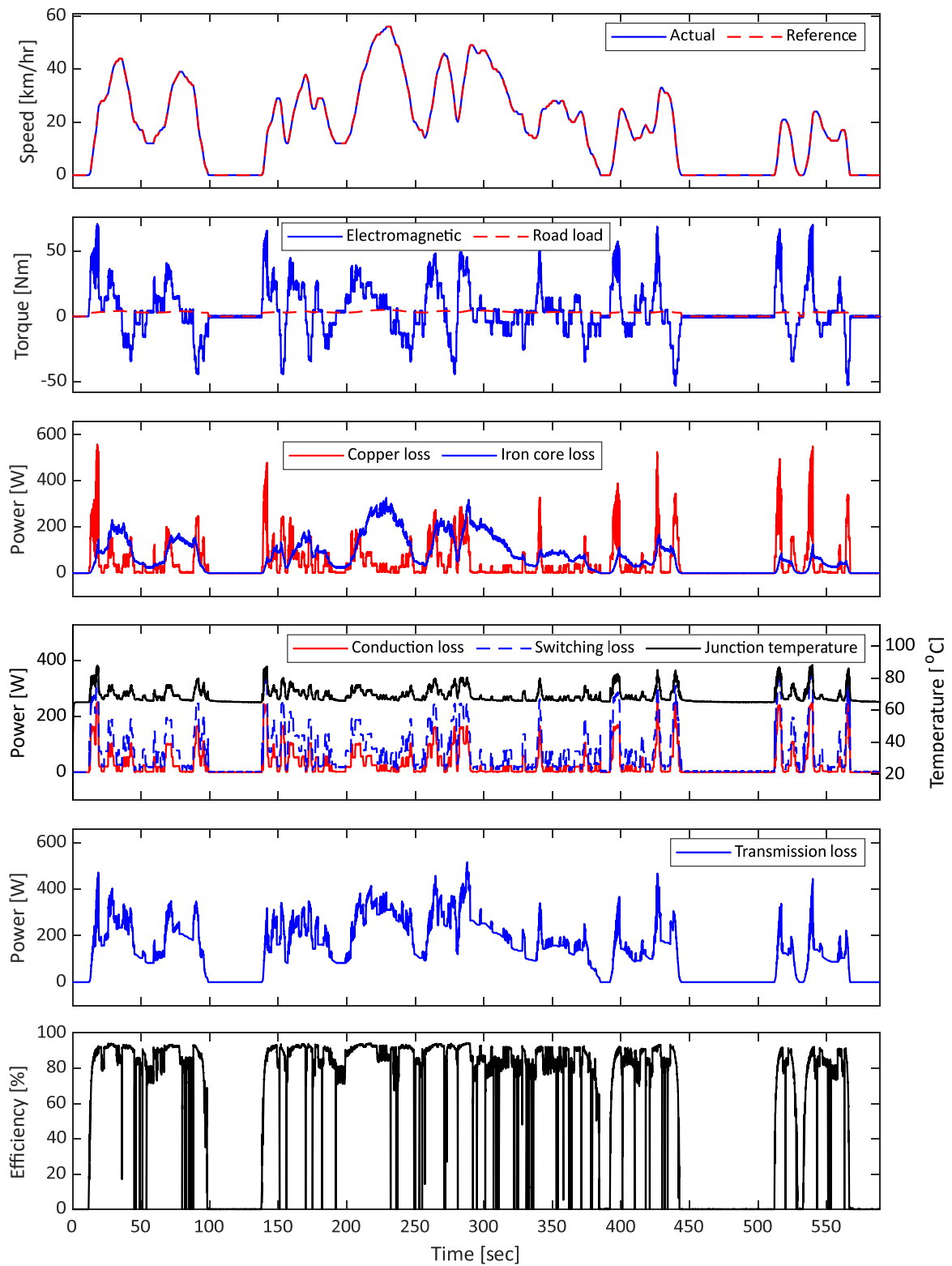


Figure 2-20: Light vehicle simulations with WLTC low drive cycle showing from top: reference and actual speed of the vehicle; electromagnetic torque and road load scaled to machine side; copper and iron losses in electric machine; switching loss, conduction loss in inverter and junction temperature of semiconductors; transmission losses and drivetrain efficiency respectively.

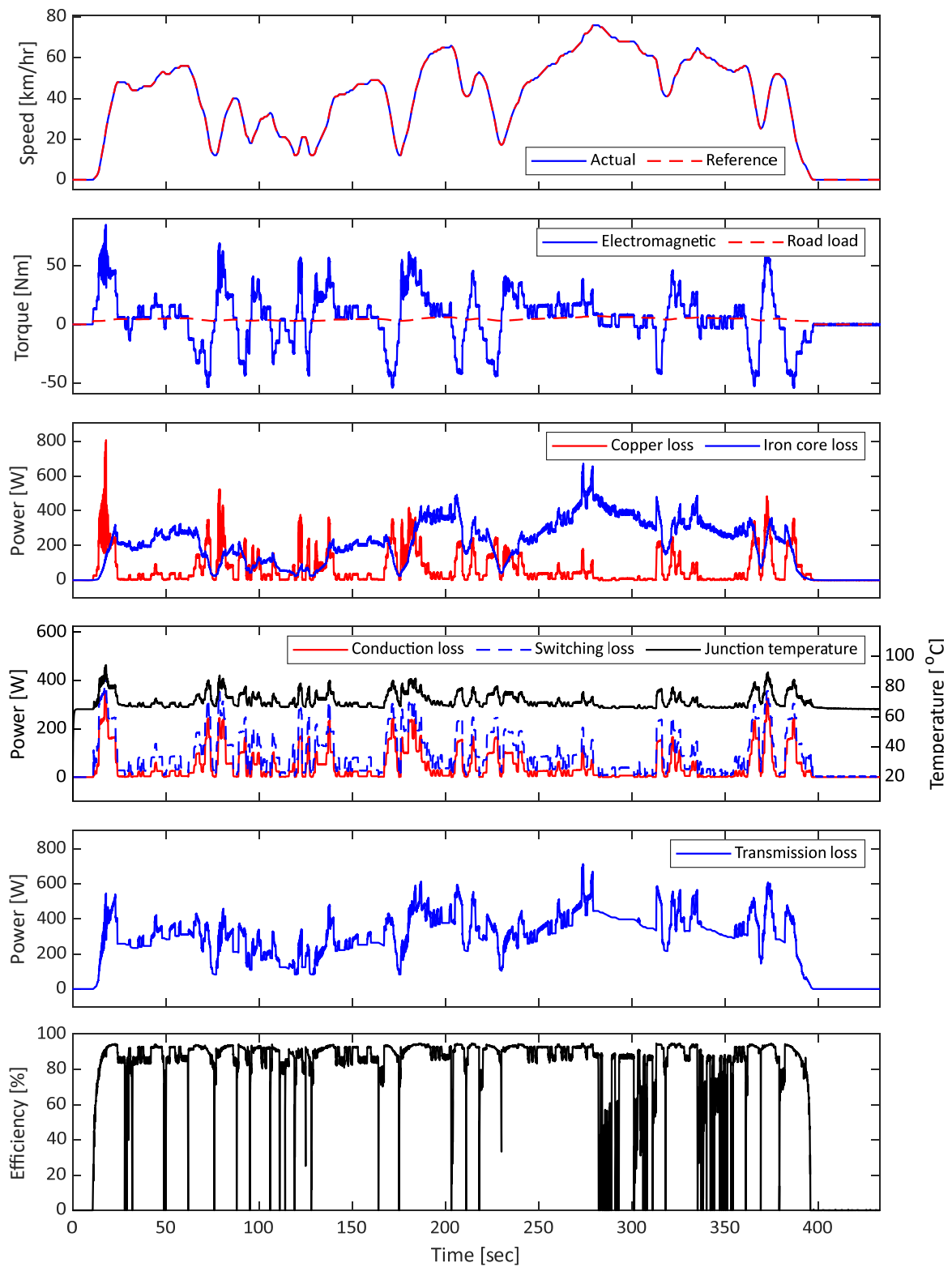


Figure 2-21: Light vehicle simulations with WLTC medium drive cycle showing from top: reference and actual speed of the vehicle; electromagnetic torque and road load scaled to machine side; copper and iron losses in electric machine; switching loss, conduction loss in inverter and junction temperature of semiconductors; transmission losses and drivetrain efficiency respectively.

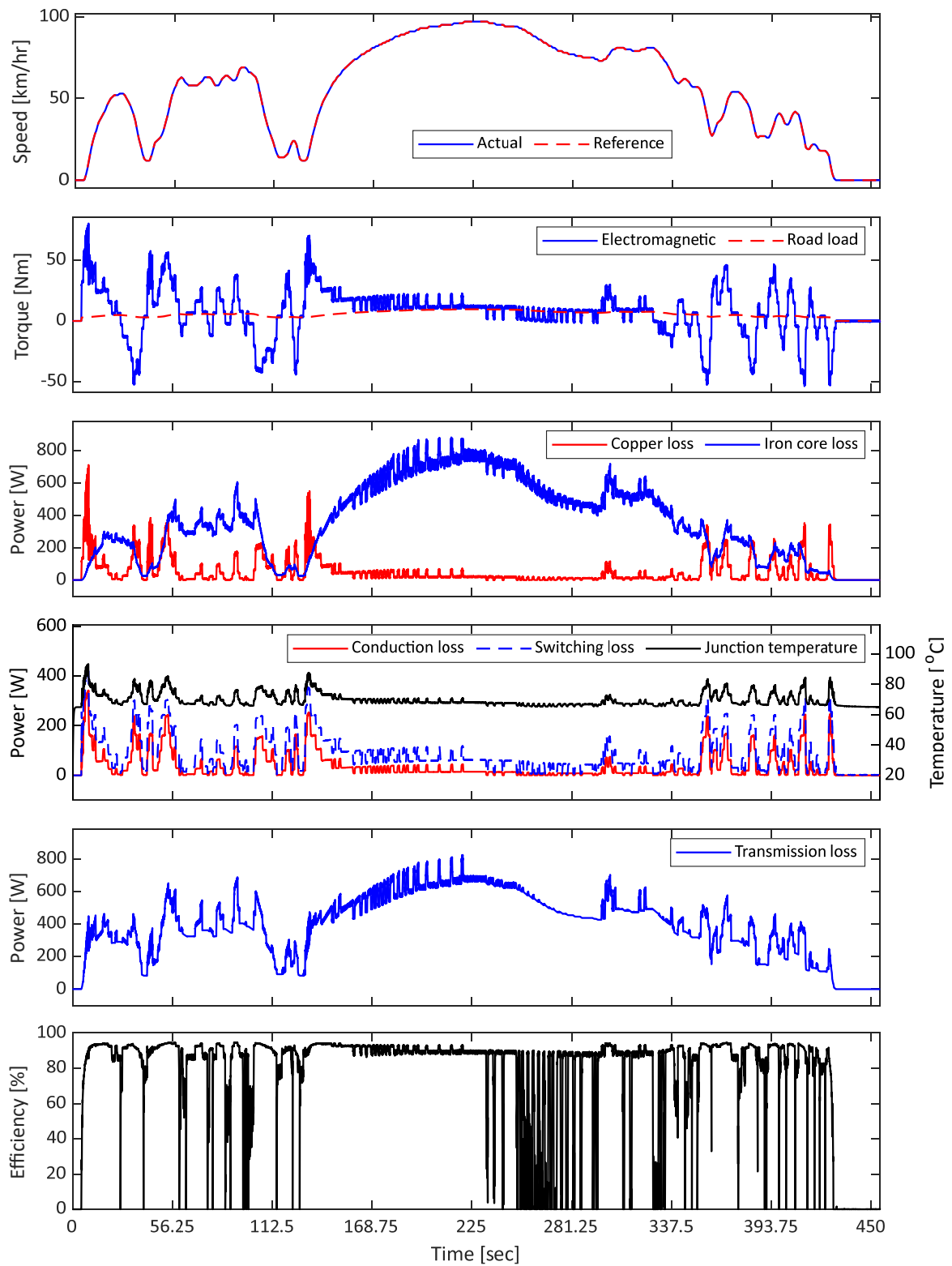


Figure 2-22: Light vehicle simulations with WLTC high drive cycle showing from top: reference and actual speed of the vehicle; electromagnetic torque and road load scaled to machine side; copper and iron losses in electric machine; switching loss, conduction loss in inverter and junction temperature of semiconductors; transmission losses and drivetrain efficiency respectively.

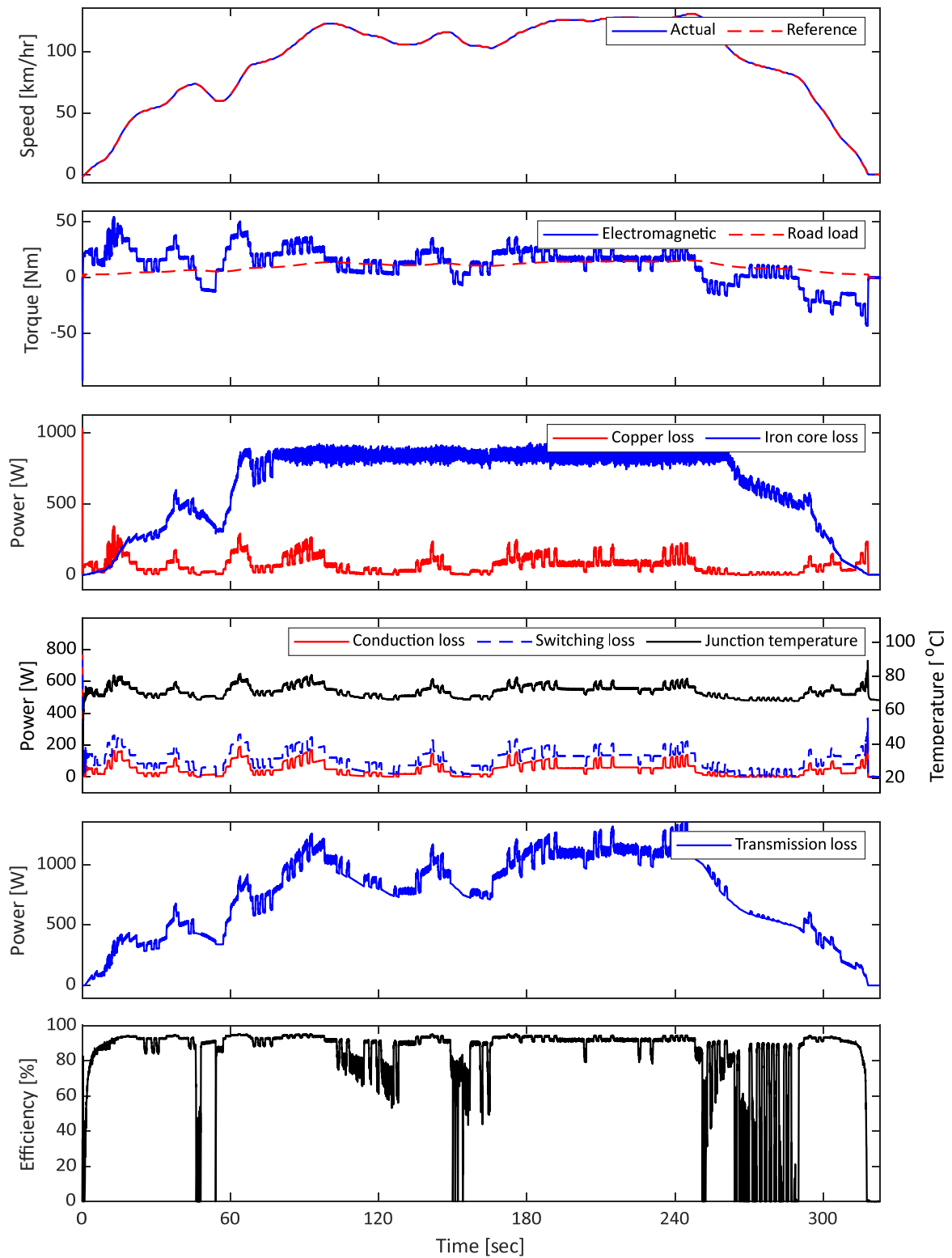
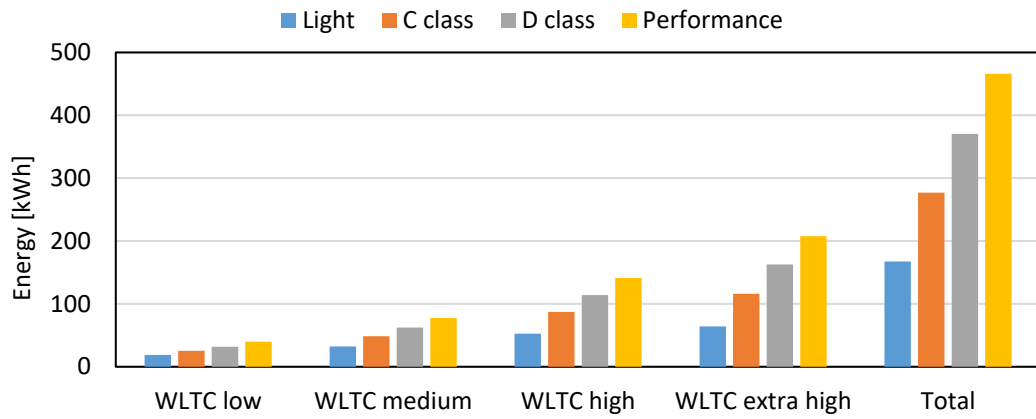


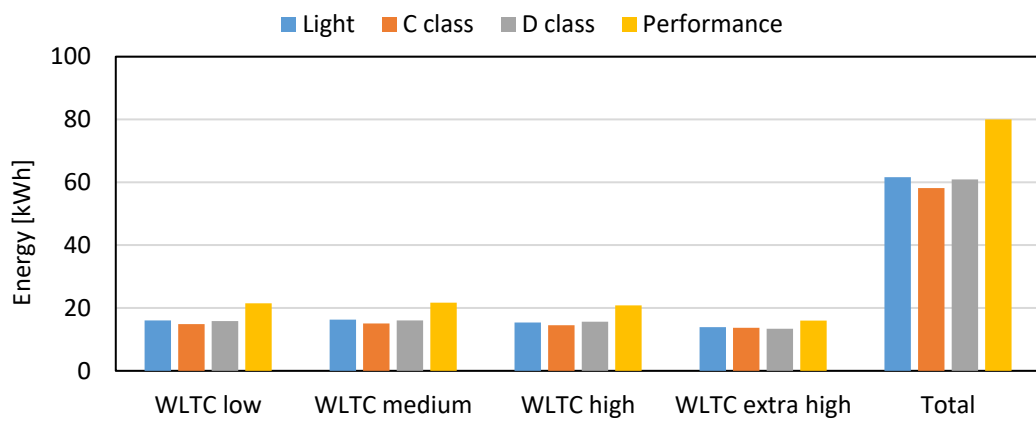
Figure 2-23: Light vehicle simulations with WLTC extra high drive cycle showing from top: reference and actual speed of the vehicle; electromagnetic torque and road load scaled to machine side; copper and iron losses in electric machine; switching loss, conduction loss in inverter and junction temperature of semiconductors; transmission losses and drivetrain efficiency respectively.

The drive cycle losses of the electric machine, the inverter, and the transmission for the four vehicles are shown in Figure 2-24 a), b), and c), respectively. The figure shows an increasing trend in the losses of electric machines and transmission for all vehicles when going from left (WLTC low) to the right (WLTC extra high). The losses in these two components are five times higher for WLTC extra high compared to WLTC low. The reason is that both electric machine and transmission losses increase with speed. Therefore, the losses show an increasing trend with speed. For the same drive cycle, an increasing trend is also observed when going from light vehicle to performance vehicle because the driving torque demand shows an increasing trend for light, C, D, and performance vehicles. The losses in electric machines and transmission are also dependent on torque. Therefore, the losses show an increasing trend from left to right for the same drive cycle in the figure. The inverter, on the other hand, does not show the above trends. The losses in the inverter reduce as the drive cycle's average speed increases because the losses in the inverter are dependent on torque. The torque demand is lower for high-speed driving of WLTC high and WLTC extra high compared to frequent WLTC low and medium accelerations and braking. When comparing the total losses of the entire drive cycle for the four different vehicles, it can be observed that the light, C class, and D class vehicles have very similar values. The performance vehicle is 30% higher than the other three. When comparing the total losses of the three components, the inverter has the lowest losses, and the transmission has the highest losses. Therefore, special attention should be given to the transmission and electric machine to optimize the drivetrain for energy efficiency.

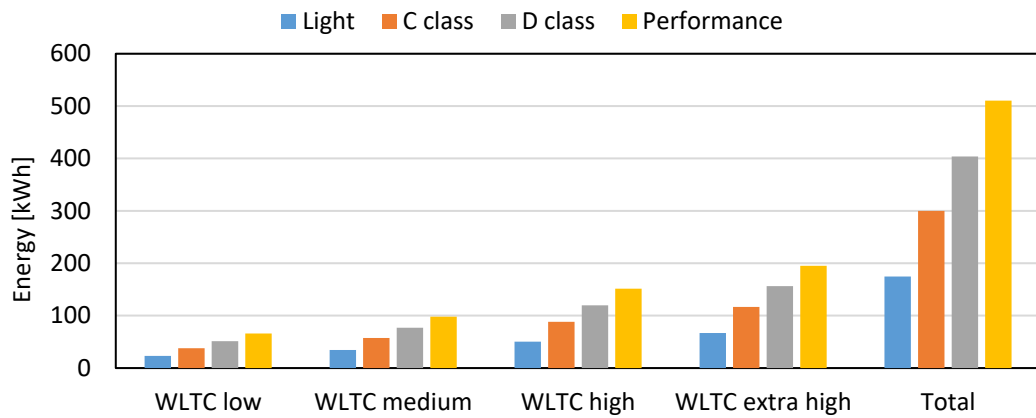
The energy consumption and average efficiency of the four vehicles for the drive cycle are shown in Figure 2-25 a) and b), respectively. The energy consumption and average efficiency for the complete drive cycle, including all the four parts, are calculated using a weightage average based on distance driven. Therefore, the values corresponding to the total are between the minimum and maximum observed for the different drive cycle parts. It can be observed from the figure that the maximum energy consumption occurs for the high-speed driving cycles, e.g., the energy consumption of the WLTC extra high is two to three times larger than for the WLTC low. It shows that more focus should be given to high-speed driving scenarios to improve the vehicle's driving range. The light, C class, D class, and performance vehicles show an increasing trend in energy consumption because the torque demand also has an increasing trend. The average efficiency of the drivetrain, as indicated in the figure, is highest for the high-speed drive cycle because the driving power is higher for such drive cycles. Therefore, the efficiency is comparatively better even with higher losses compared to low-speed drive cycles. Among the different vehicles, light vehicles have the highest average efficiency, and performance vehicles have the lowest. Since the light vehicle has the smallest drivetrain regarding torque and power, the partial load efficiency will be comparatively highest. The average total drive cycle efficiency varies by less than 3% for the remaining three vehicle types. Therefore, the standardization of the drivetrain results in a similar drive cycle efficiency for C, D class, and performance vehicles and the highest efficiency for light vehicles.



(a)



(b)



(c)

Figure 2-24: Total energy losses of a) electric machine, b) inverter and c) transmission for WLTC drive cycle considering four different vehicles.

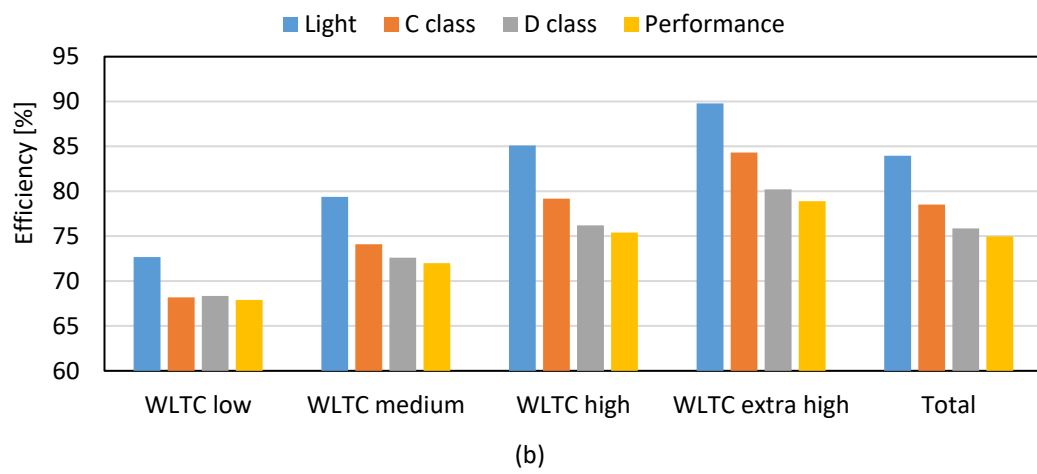
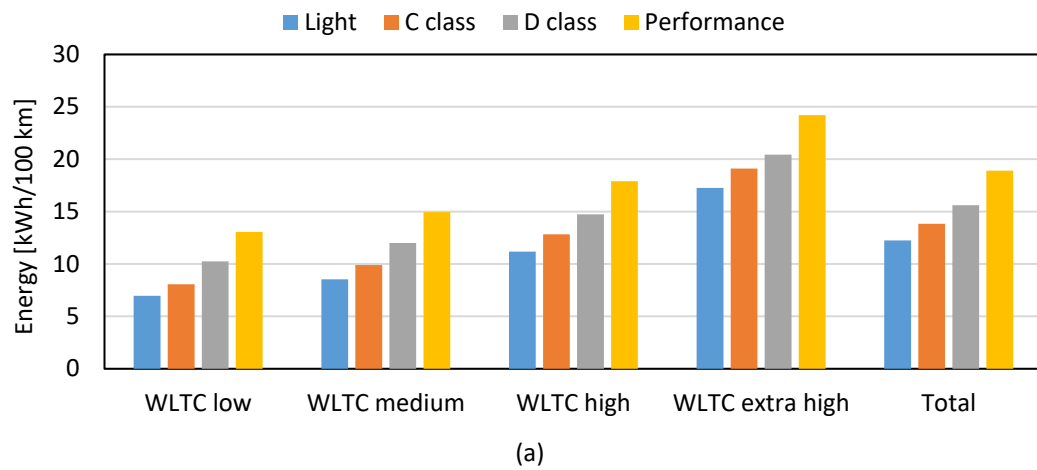


Figure 2-25: a) Total energy consumption per 100 km and b) average efficiency for WLTC drive cycle considering four different vehicles.

Chapter 3

Control of Machine Emulators

In this chapter, the model of the coupling network is derived, followed by a description of closed and open loop control of the machine emulator, and finalized with verification of open loop control using simulations. The verifications are done by comparing simulated terminal voltages and currents of the machine emulator to an equivalent PMSM drive for traction application. The comparison is performed for both steady-state and transient simulation results. A schematic of a machine emulator is shown in Figure 3-1. It consists of a VSC with a coupling network on the AC side. The inverter under test (IUT) is connected to the AC side of the coupling network that is open. The coupling network is a passive element, e.g., single-phase inductors, three-phase inductors, and transformers. The inductance of the coupling network limits the rise of current, without which the control of current is complex.

3.1 Model of coupling network

A mathematical model of the coupling network is necessary for deriving the emulator's control. The derivation of the model depends on the choice of coupling network used in the emulator. Two different coupling networks are considered in the following sections.

3.1.1 Single-phase inductor

Three single-phase inductors are the most straightforward choice for a coupling network. The emulator terminal voltage is composed of the voltage drop across the inductors and the voltage produced by the VSC. The voltage drop across the inductor consists of the resistive voltage drop and electromotive forces (EMF) due to derivatives of magnetic flux linkages and can be described as

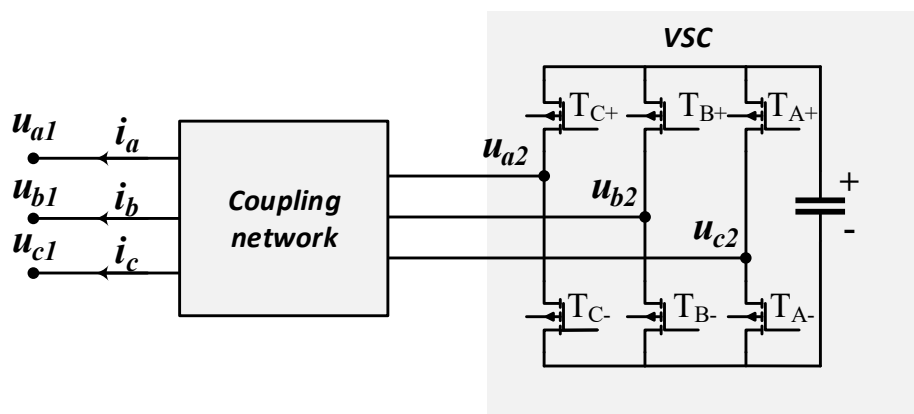


Figure 3-1: Schematic of a machine emulator

$$\begin{bmatrix} u_{a1} \\ u_{b1} \\ u_{c1} \end{bmatrix} = \begin{bmatrix} R_a & 0 & 0 \\ 0 & R_b & 0 \\ 0 & 0 & R_c \end{bmatrix} \begin{bmatrix} i_a \\ i_b \\ i_c \end{bmatrix} + \frac{d}{dt} \begin{bmatrix} \psi_a \\ \psi_b \\ \psi_c \end{bmatrix} + \begin{bmatrix} u_{a2} \\ u_{b2} \\ u_{c2} \end{bmatrix} \quad (3-1)$$

where u denotes voltages, R denotes resistances, i denotes currents, ψ denotes flux linkages, a, b, c denote phases A, B, C and 1, 2 denotes the terminals of the emulator and the VSC respectively. If the magnetic core of the inductor is operating in the linear region of the BH curve, the flux linkages can be expressed as

$$\begin{bmatrix} \psi_a \\ \psi_b \\ \psi_c \end{bmatrix} = \begin{bmatrix} L_a & 0 & 0 \\ 0 & L_b & 0 \\ 0 & 0 & L_c \end{bmatrix} \begin{bmatrix} i_a \\ i_b \\ i_c \end{bmatrix} \quad (3-2)$$

where L indicates self-inductance. The mutual components are zero since there are no magnetic couplings between the three phases when using three single-phase inductors.

In machine control, it is common to control DC quantities in the dq-frame instead of the AC quantities in abc-frame. Therefore, the model of the coupling network is also transformed to dq-frame by co-ordinate transformation. The transformation from abc-frame to dq-frame is composed of two different transformations: $abc \leftrightarrow \alpha\beta\gamma$ transformation or Clarke transformation [50] and $\alpha\beta\gamma \leftrightarrow dq0$ or the Park transformation [51]. With a combination of these two transformations, the three-phase electrical quantities can be presented in the dq-frame, and vice versa.

$$\begin{bmatrix} x_d \\ x_q \\ x_0 \end{bmatrix} = T_{abc \rightarrow dq0} \begin{bmatrix} x_a \\ x_b \\ x_c \end{bmatrix} \quad \begin{bmatrix} x_a \\ x_b \\ x_c \end{bmatrix} = T_{dq0 \rightarrow abc} \begin{bmatrix} x_d \\ x_q \\ x_0 \end{bmatrix} \quad (3-3)$$

where x denotes any electrical quantity, d denotes d-axis, q denotes q-axis, 0 denotes zero-sequence, $T_{abc \rightarrow dq0}$ denotes the $abc \rightarrow dq0$ transformation matrix and $T_{dq0 \rightarrow abc}$ denotes the $dq0 \rightarrow abc$ transformation matrix. The transformation matrices are

$$T_{abc \rightarrow dq0} = k_1 \begin{bmatrix} \cos(\omega t) & \cos\left(\omega t - \frac{2}{3}\pi\right) & \cos\left(\omega t + \frac{2}{3}\pi\right) \\ -\sin(\omega t) & -\sin\left(\omega t - \frac{2}{3}\pi\right) & -\sin\left(\omega t + \frac{2}{3}\pi\right) \\ k_0 & k_0 & k_0 \end{bmatrix} \quad (3-4)$$

$$T_{dq0 \rightarrow abc} = \frac{2}{3k_1} \begin{bmatrix} \cos(\omega t) & -\sin(\omega t) & \frac{1}{2k_0} \\ \cos\left(\omega t - \frac{2}{3}\pi\right) & -\sin\left(\omega t - \frac{2}{3}\pi\right) & \frac{1}{2k_0} \\ \cos\left(\omega t + \frac{2}{3}\pi\right) & -\sin\left(\omega t + \frac{2}{3}\pi\right) & \frac{1}{2k_0} \end{bmatrix} \quad (3-5)$$

where ω is the electrical frequency. The scaling factors k_1 and k_0 in (3-4) and (3-5) are added to the transformation in order to fit different preferences. The *amplitude-invariant*

transformation and *power-invariant transformation* are the two popular ones. In this work, only amplitude invariant transformation is used. Therefore, the scaling factors are as follows.

$$k_1 = \frac{2}{3} \quad k_0 = \frac{1}{2} \quad (3-6)$$

The flux linkage equation in the dq-frame can then be derived from the flux linkage equation (3-2) in the abc-frame

$$\begin{bmatrix} \psi_d \\ \psi_q \\ \psi_0 \end{bmatrix} = L_{dq0} \begin{bmatrix} i_d \\ i_q \\ i_0 \end{bmatrix}. \quad (3-7)$$

If we assume that the three inductors have identical inductance then, the inductance matrix L_{dq0} can be derived from above equation as

$$L_{dq0} = T_{abc \rightarrow dq0} \begin{bmatrix} L_a & 0 & 0 \\ 0 & L_a & 0 \\ 0 & 0 & L_a \end{bmatrix} T_{dq0 \rightarrow abc} = \begin{bmatrix} L_a & 0 & 0 \\ 0 & L_a & 0 \\ 0 & 0 & L_a \end{bmatrix}. \quad (3-8)$$

If the resistance of the three inductors is identical then, the voltage equation (3-1) in abc-frame can be written in dq-frame as

$$\begin{bmatrix} u_{d1} \\ u_{q1} \\ u_{01} \end{bmatrix} = \begin{bmatrix} R_a & 0 & 0 \\ 0 & R_a & 0 \\ 0 & 0 & R_a \end{bmatrix} \begin{bmatrix} i_d \\ i_q \\ i_0 \end{bmatrix} + \begin{bmatrix} 0 & -\omega & 0 \\ \omega & 0 & 0 \\ 0 & 0 & 0 \end{bmatrix} \begin{bmatrix} \psi_d \\ \psi_q \\ \psi_0 \end{bmatrix} + \frac{d}{dt} \begin{bmatrix} \psi_d \\ \psi_q \\ \psi_0 \end{bmatrix} + \begin{bmatrix} u_{d2} \\ u_{q2} \\ u_{02} \end{bmatrix}. \quad (3-9)$$

Assuming constant inductance and substitution for flux linkages in (3-9)

$$\begin{bmatrix} u_{d1} \\ u_{q1} \\ u_{01} \end{bmatrix} = \mathbf{R}_{mat} \begin{bmatrix} i_d \\ i_q \\ i_0 \end{bmatrix} + \mathbf{L}_{mat} \begin{bmatrix} \frac{di_d}{dt} \\ \frac{di_q}{dt} \\ \frac{di_0}{dt} \end{bmatrix} + \begin{bmatrix} u_{d2} \\ u_{q2} \\ u_{02} \end{bmatrix} \quad (3-10)$$

$$\mathbf{R}_{mat} = \begin{bmatrix} R_a & -\omega(L_l + L_m) & 0 \\ \omega(L_l + L_m) & R_a & 0 \\ 0 & 0 & R_a \end{bmatrix}$$

$$\mathbf{L}_{mat} = \begin{bmatrix} L_l + L_m & 0 & 0 \\ 0 & L_l + L_m & 0 \\ 0 & 0 & L_l + L_m \end{bmatrix}$$

where L_l and L_m indicate the leakage and main inductance of each phase. The coupling terms $-\omega L_a i_q$ and $\omega L_a i_d$ appear only in the d- and q-axis equations, because the zero-sequence component of flux linkage ψ_0 rotates with three times the fundamental frequency. The equivalent circuit in d- and q-axis can then be drawn for the single-phase inductor as shown in Figure 3-2.

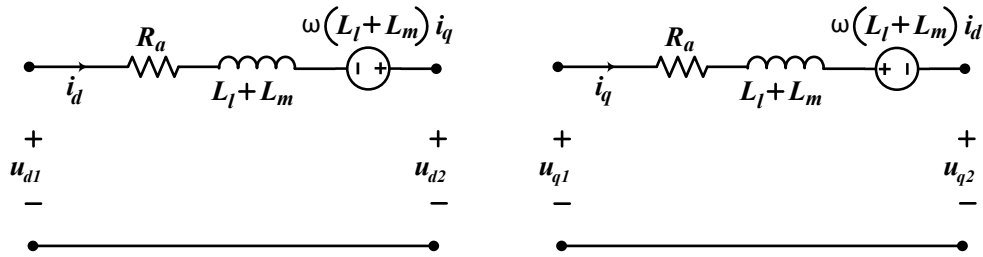


Figure 3-2: D- and q-axis equivalent circuit model of a single-phase inductor

3.1.2 Three-phase coupled inductor

A three-phase coupled inductor can be modeled in a very similar way to the single-phase inductors. The three-phase voltage equation is identical as in (3-1). The magnetic core of the inductor is assumed to operate in the linear region of the BH curve. Since there are now magnetic couplings between the three phases, the flux linkages can be expressed as

$$\begin{bmatrix} \psi_a \\ \psi_b \\ \psi_c \end{bmatrix} = \begin{bmatrix} L_a & M_{ab} & M_{ac} \\ M_{ba} & L_b & M_{bc} \\ M_{ca} & M_{cb} & L_c \end{bmatrix} \begin{bmatrix} i_a \\ i_b \\ i_c \end{bmatrix} = \mathbf{L}_{abc} \begin{bmatrix} i_a \\ i_b \\ i_c \end{bmatrix} \quad (3-11)$$

where L denotes self-inductances, M denotes mutual inductances. If we assume that the cross-sections of flux paths in the inductor shown in Figure 3-3 are uniform, then the flux from phase A will link to the other two phases equally. In addition, the direction of self and mutual flux is opposite. If the three phases have identical leakage and number of turns, the inductance matrix in (3-11) can be formulated as

$$\mathbf{L}_{abc} = \begin{bmatrix} L_l + L_m & -\frac{L_m}{2} & -\frac{L_m}{2} \\ -\frac{L_m}{2} & L_l + L_m & -\frac{L_m}{2} \\ -\frac{L_m}{2} & -\frac{L_m}{2} & L_l + L_m \end{bmatrix} \quad (3-12)$$

where L_l and L_m indicate the leakage and main inductance of each phase.

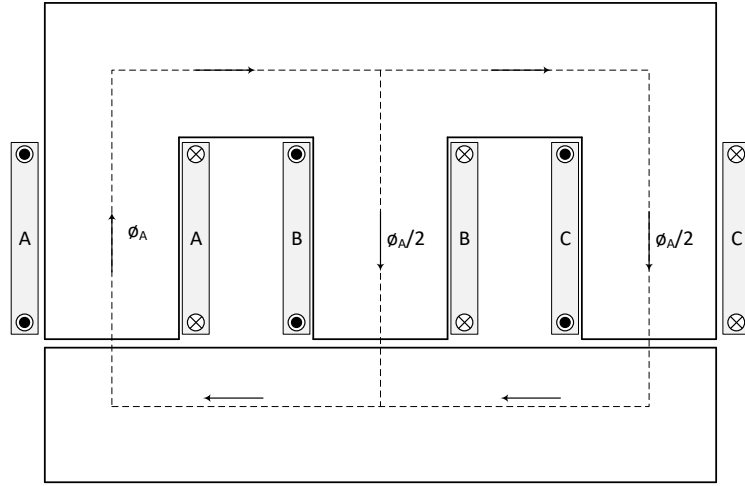


Figure 3-3: Cross-section of a three-phase coupled inductor

Now, flux linkage equation in the dq-frame can then be derived as

$$\begin{bmatrix} \psi_d \\ \psi_q \\ \psi_0 \end{bmatrix} = \begin{bmatrix} L_l + \frac{3}{2}L_m & 0 & 0 \\ 0 & L_l + \frac{3}{2}L_m & 0 \\ 0 & 0 & L_l \end{bmatrix} \begin{bmatrix} i_d \\ i_q \\ i_0 \end{bmatrix}. \quad (3-13)$$

Due to the magnetic coupling, the flux linkages in the d- and q-axis are enhanced. If saturation of the iron-core is neglected, the per phase inductance of a three-phase inductor for the same core and copper volume is 50% higher than that of a single-phase inductor. In addition, the zero-sequence component of the main flux gets canceled if the three phases are assumed to be symmetric. Therefore, only the leakage inductance contributes to the zero component of the flux linkage. However, this will cause a more significant zero component of current in the case of three-phase inductors when compared to single-phase inductors.

If the resistances of the three phases are identical, the voltage equation in dq-frame, then can be described as

$$\begin{bmatrix} u_{d1} \\ u_{q1} \\ u_{01} \end{bmatrix} = \mathbf{R}_{mat} \begin{bmatrix} i_d \\ i_q \\ i_0 \end{bmatrix} + \mathbf{L}_{mat} \begin{bmatrix} \frac{di_d}{dt} \\ \frac{di_q}{dt} \\ \frac{di_0}{dt} \end{bmatrix} + \begin{bmatrix} u_{d2} \\ u_{q2} \\ u_{02} \end{bmatrix} \quad (3-14)$$

$$\mathbf{R}_{mat} = \begin{bmatrix} R_a & -\omega \left(L_l + \frac{3}{2}L_m \right) & 0 \\ \omega \left(L_l + \frac{3}{2}L_m \right) & R_a & 0 \\ 0 & 0 & R_a \end{bmatrix}$$

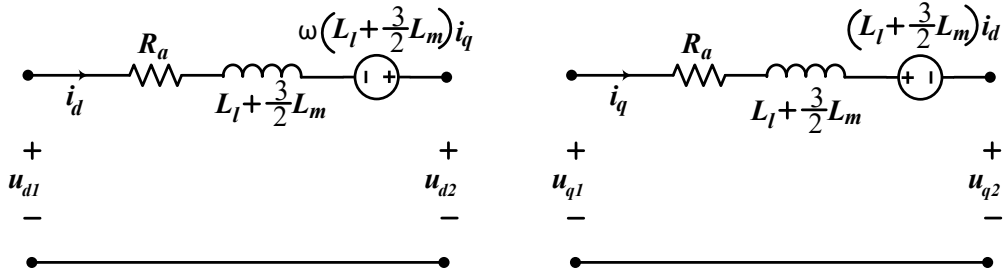


Figure 3-4: D- and q-axis equivalent circuit model of a three-phase inductor

$$\mathbf{L}_{mat} = \begin{bmatrix} L_l + \frac{3}{2}L_m & 0 & 0 \\ 0 & L_l + \frac{3}{2}L_m & 0 \\ 0 & 0 & L_\sigma \end{bmatrix}.$$

The equivalent circuit in d-and q-axis can then be drawn for the three-phase inductor as shown in Figure 3-4.

3.2 Control of machine emulator

The control of a machine emulator can be implemented in two ways: open loop and closed loop. Both methods have their respective advantages and disadvantages. In the following sections, the two control methods are described.

3.2.1 Open loop control

As the name suggests, open loop control of a machine emulator is characterized by the lack of a feedback control loop. A schematic of a machine emulator with this control is presented in Figure 3-5. The setup consists of an inverter under test (IUT) connected to an emulator VSC via a coupling network. In the open loop control, the measured three-phase currents and the interpolated flux linkages of the electric machine are used to calculate the electromagnetic torque according to (2-7). Next, rotor speed and angle can be obtained via (2-8). The voltage reference of the emulator VSC in the dq-frame can then be calculated using the dq-model of the machine and the coupling network as follows

$$\begin{aligned} u_{d2} &= i_d(R_s - R_{CN}) + L'_d \frac{di_d}{dt} - \omega \psi'_q \\ u_{q2} &= i_q(R_s - R_{CN}) + L'_q \frac{di_q}{dt} + \omega \psi'_d \\ \psi'_d &= \psi_d - L_{CN}i_d \quad ; \quad \psi'_q = \psi_q - L_{CN}i_q \\ L'_d &= L_d - L_{CN} \quad ; \quad L'_q = L_q - L_{CN} \end{aligned} \tag{3-15}$$

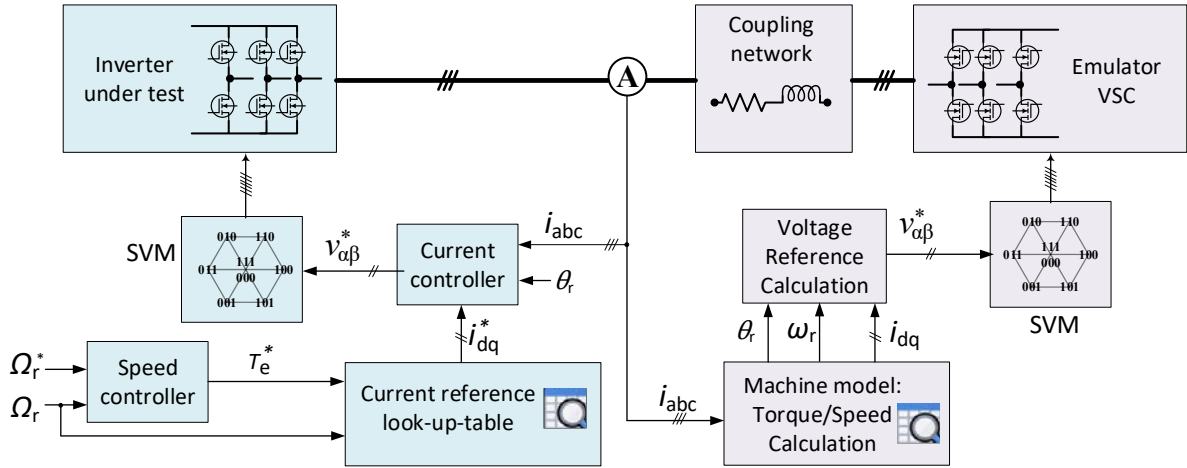


Figure 3-5: Schematic of a machine emulator with open loop control

where u_{d2} and u_{q2} are the voltage reference of the emulator VSC in dq-frame. In addition, L'_d , L'_q are fictitious d- and q-axis incremental inductance compensating for the coupling network inductance and ψ'_d , ψ'_q are the fictitious d- and q- axis flux linkages after compensating for the induced emf in the coupling network. R_{CN} and L_{CN} are the resistance and inductance of the coupling network in the dq-frame. The calculated voltage references are then used to generate gate pulses to control the emulator VSC.

The open loop control of the emulator can provide an inexpensive and flexible test method for laboratory verification of the IUT. It can be observed from (3-15) that the model equations need to be solved once per switching period. Therefore, the control of the emulator can be implemented using inexpensive DSPs. In addition, standard current measurements can be used to control the emulator. Furthermore, the open loop control of the emulator provides two possibilities in selecting VSC to build the emulator. Firstly, a standard 2-level VSC with similar ratings, e.g., voltage, current, and maximum switching frequency, as IUT can be used. Secondly, the same VSC used as IUT can be implemented inside the emulator [14], [18]. Therefore, testing IUTs with different power ratings and topology, e.g., multi-level, multi-phase, mainly requires prototyping an appropriate coupling network.

The control method has some disadvantages. The voltage references used to control the emulator VSC depends on the parameters of the coupling network. Therefore, such a control method is sensitive to parameter estimation of the coupling network. Since the derivatives of the currents are obtained from the measured currents instead of estimation from the machine model, phase current ripple in this control method will be purely determined by the switching frequency of the emulator VSC, duty cycle, and inductance of the coupling network. Consequently, this control method can only be used to emulate the fundamental component of the voltage and current effectively.

3.2.2 Closed loop control

A closed loop control is characterized by the presence of a feedback loop. Schematic of a closed loop control of a machine emulator is presented in Figure 3-6. In this approach, PWM

voltages of the three phases are measured. The measured voltages are used to estimate current derivatives in dq-frame using the model of the machine as below

$$\begin{bmatrix} \frac{di_d}{dt} \\ \frac{di_q}{dt} \end{bmatrix} = -\mathbf{L}_{\text{mat}}^{-1} \mathbf{R}_{\text{mat}} \begin{bmatrix} i_d \\ i_q \end{bmatrix} + \mathbf{L}_{\text{mat}}^{-1} \begin{bmatrix} u_d + \omega \psi_q \\ u_q - \omega \psi_d \end{bmatrix} \quad (3-16)$$

$$\mathbf{L}_{\text{mat}} = \begin{bmatrix} L_{dd} & L_{dq} \\ L_{qd} & L_{qq} \end{bmatrix}$$

$$\mathbf{R}_{\text{mat}} = \begin{bmatrix} R_s & 0 \\ 0 & R_s \end{bmatrix}.$$

Integration of the current derivatives provides the current reference for a current control loop inside the emulator. In the closed loop control, the measured three-phase currents are used together with the reference currents generated from the machine model, to form a feedback loop. The output of the current controller provides voltage reference which are used to generate gate pulses to control the emulator VSC. The torque of the machine is calculated using interpolated flux linkages of electric machine and estimated currents. The rotor speed and angle are calculated as in open loop control.

Since a current controller is used to obtain the voltage reference, the closed loop control is not as sensitive to coupling network parameter estimation errors as the open loop control. In addition, the derivatives of the current are calculated the using machine model. When combined with a high bandwidth current control, this will result in a current ripple that is a better representation of the ripple obtained with a real machine. Therefore, a closed loop control method may be more suitable when emulating higher order harmonics of the machine.

The switching frequency of the inverter used in automotive applications can be from 5-20 kHz which means voltage sensors with bandwidths of 0.5-2 MHz or higher will be necessary. In addition, field-programmable gate array (FPGA) based I/O boards may be required for

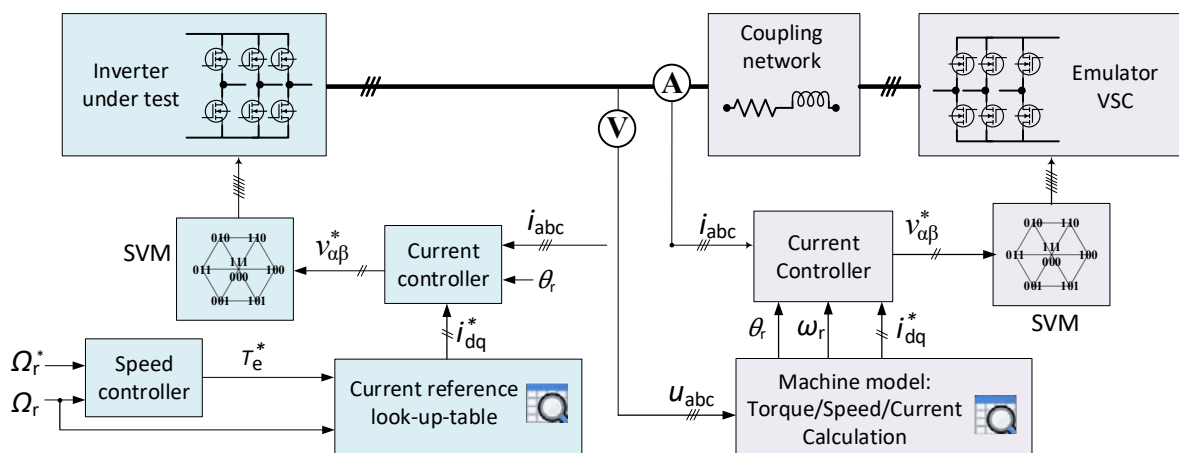


Figure 3-6: Schematic of a machine emulator with closed loop control

sampling of the measured voltages. The measurement of PWM voltages is also prone to noise and may require special considerations such as analog filters. In addition, the current controller inside the emulator will experience a current control conflict with the current controller used to control of IUT. A solution to resolve this conflict is to use a higher bandwidth for the current controller inside the emulator [16]. Therefore, the switching frequency of the emulator VSC may need to be higher than the VSC especially when testing IUTs with high bandwidth current control. Furthermore, if the current derivatives in (3-16) are not assumed to be linear, then the derivatives need to be solved for each sampled voltage. Therefore, the control of the emulator may need to be implemented using FPGAs. Hence, a closed loop control may result in a complex and expensive solution for laboratory testing of inverters.

3.3 Verification of open loop control

The schematic of the power-hardware-in-the-loop test bench considered in this work is shown in Figure 3-7. It is modeled in PLECS/Simulink to verify the open loop control method. It consists of two identical VSCs connected on the AC side via a coupling network. Three single-phase inductors are used as coupling network. One of the VSC represent the IUT while the other is used to model the machine emulator. DC links of the IUT and the VSC inside the emulator are connected back-to-back to the same DC supply. Therefore, during experiments a smaller rated power supply can be used to test full rated conditions as only the loss in the setup needs to be supplied. Selected parameters of the IUT and the coupling network used in simulations are listed in Table 3-1. The inductors are modeled with constant inductances without considering the effect of saturation. The common- DC link connection between the IUT and the emulator VSC will result into circulating common-mode currents consisting of DC,

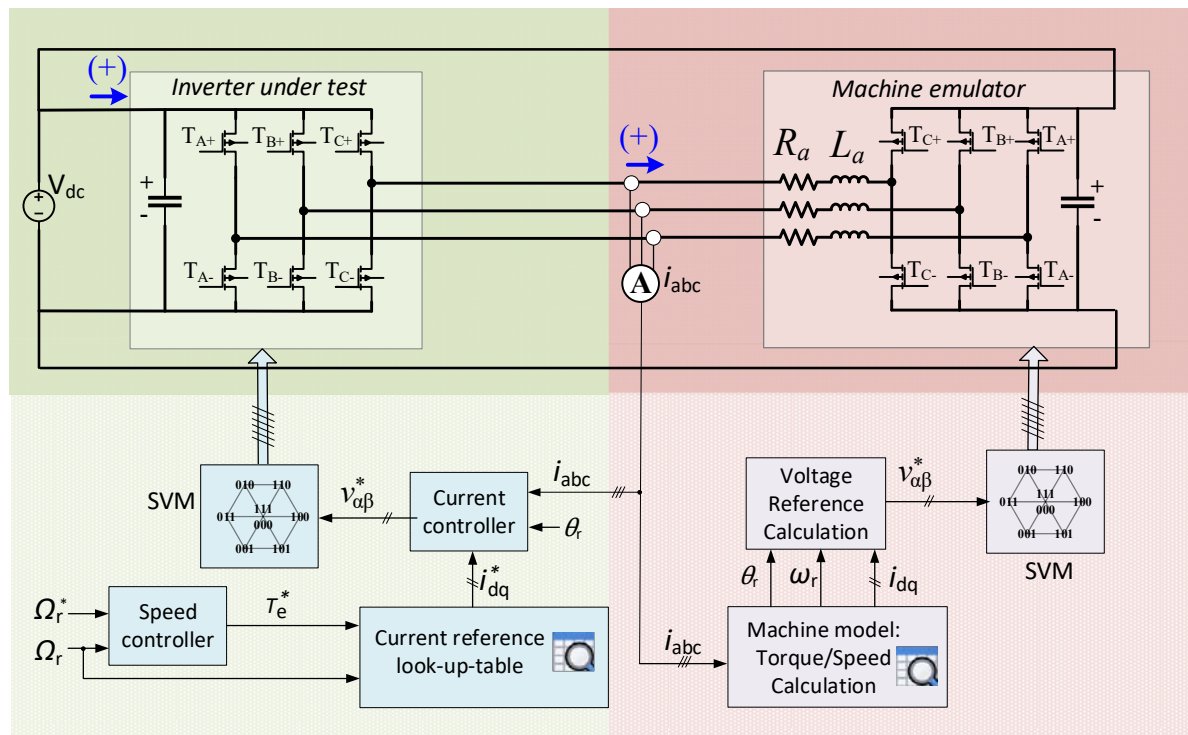


Figure 3-7: Schematic of the back-to-back power-hardware-in-the-loop test bench considered for modeling

low-frequency, and high-frequency components, [14] [18]. In the simulations, a PI controller regulates DC and low frequency components of the common-mode currents [52], [48].

To compare the machine emulator in simulation, an equivalent PMSM drive intended for traction application is also modeled in PLECS/Simulink. The PMSM is driven by the same VSC which is used as IUT in the PHIL test bench. The key parameters of the modeled PMSM are listed in Table 3-1. It is an 8 pole 48 slot 60 kW machine with interior permanent magnets in the rotor and hairpin windings in the stator. The dynamic model of the machine is implemented as described in Chapter 2. The flux linkages and inductances as shown in Figure 3-8 and Figure 3-9 respectively are obtained from the FEM model of the machine. The dependency of resistance on frequency and temperature is ignored in modeling of the simulation of PMSM drive and control of emulator in PHIL test bench. Thus, it will not influence the results. In addition, the static friction torque is neglected in the modeling as it is more relevant in experiments.

The control of the IUT when simulated with PMSM is the same as presented in the Figure 3-7. It has a cascaded structure with PI-based speed controller in the outer loop and a field oriented current controller in the inner loop. The bandwidth of the current controller and

Table 3-1: Parameters of the IUT, coupling network and PMSM

Parameter	Value	Unit
IUT		
DC link voltage	360	V
Switching frequency	20	kHz
Current controller bandwidth	1000	rad/s
Speed controller bandwidth	20	rad/s
Coupling network		
Resistance	13	mΩ
Inductance	0.4	mH
PMSM		
Maximum torque (for 30 s)	200	Nm
Peak power (for 30 s)	60	kW
Pole pair	4	
No load d-axis inductance	0.43	mH
No load q-axis inductance	1.3	mH
Stator resistance	55.4	mΩ
End winding leakage inductance	6.64	μH
Rotor inertia	0.047	kg/m ²
Viscous damping constant	0.000893	Nms/rad
Maximum rotor speed	9000	rpm

speed controllers are listed in Table 3-1. The gains of the current and speed controllers are selected using loop-shaping as described in [47]. In loop-shaping, the response of the closed loop system with controller and the plant is shaped as a first order low pass filter with the selected bandwidth. Current reference look-up-tables are used to calculate the current references. The current reference look-up-tables are generated dq-model of the PMSM as described in [53]. The look-up-tables used in the simulation are presented in Figure 3-10. It

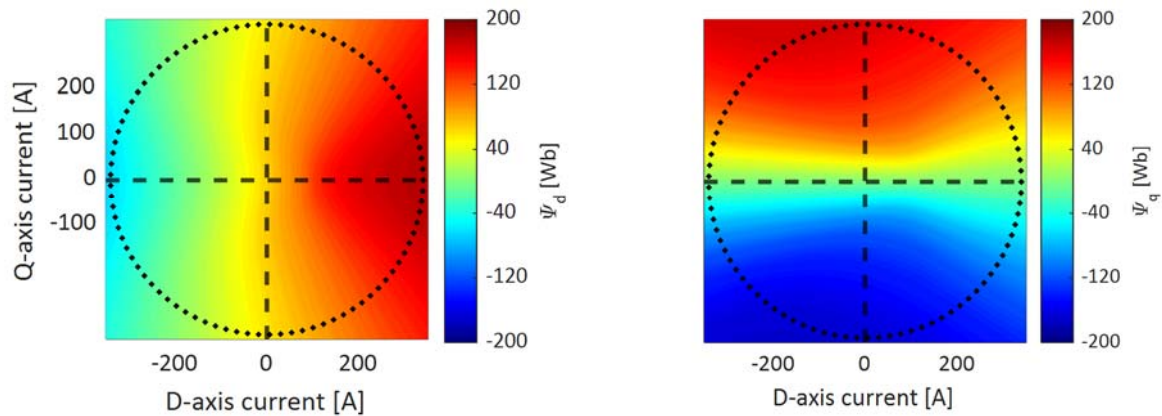


Figure 3-8: D- (a) and q-axis (b) flux linkages of a PMSM calculated from FEM model.

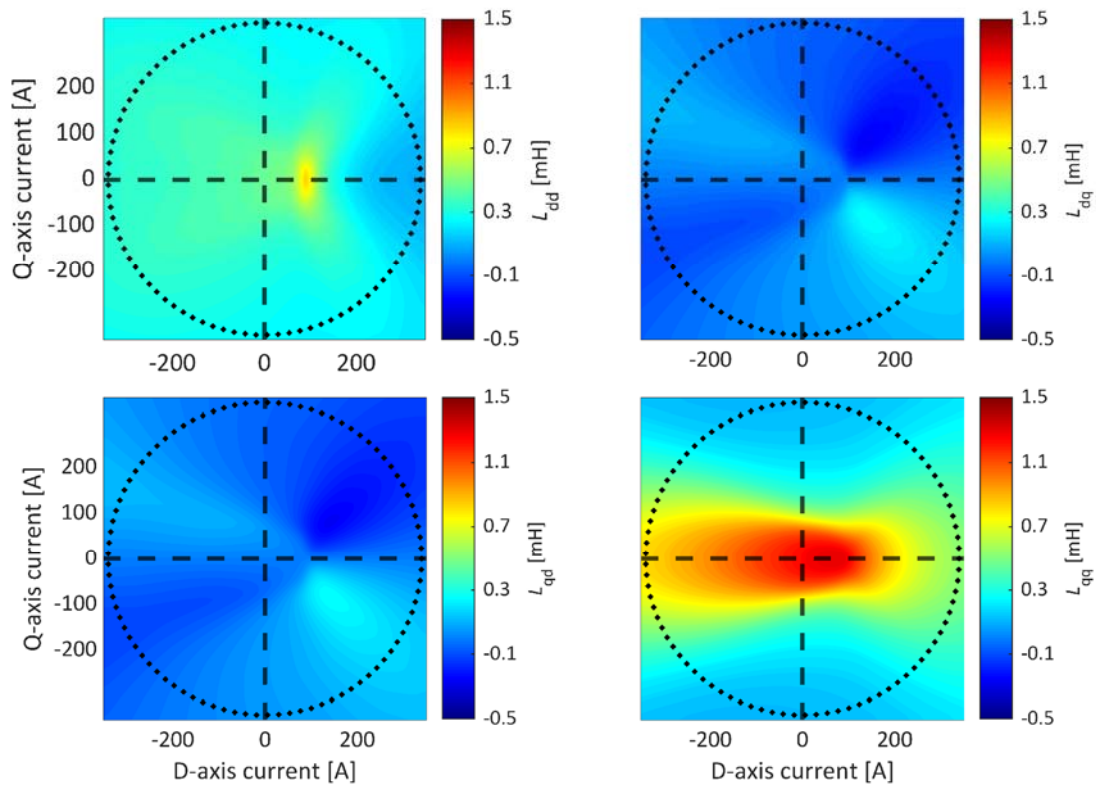


Figure 3-9: Incremental inductance of a PMSM calculated using flux linkages from FEM model.

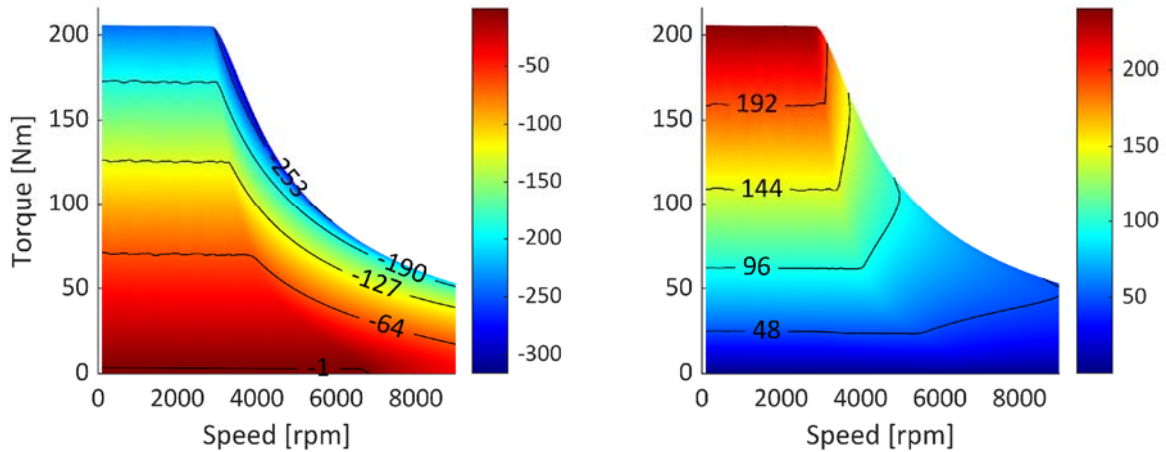


Figure 3-10: D-and q-axis current reference look-up-tables of the PMSM in motor mode. The unit of current is Ampere.

should be noted that even though the results of the motor mode of operation are presented, the conclusions are applicable to generator mode as well.

3.3.1 Steady state performance

Simulation results of IUT when simulated with a machine emulator are compared to simulation of IUT with PMSM. Two different cases are presented in Figure 3-11 and Figure 3-12. The results shown in Figure 3-11 corresponds to peak torque operation of the machine with steady-state rotor speed of 750 rpm and load torque of 180 Nm. Similarly, the results in Figure 3-12 corresponds to peak power operation of the machine with steady-state rotor speed of 3000 rpm and load torque of 160 Nm. Lower cases are used for variables when denoting instantaneous quantities while upper case for fundamental or average. Four subplots are shown in the figure: phase current, line voltage, active and reactive power supplied by IUT. The powers are calculated using instantaneous three phase voltage and currents. The line voltage shown in figure is derived from phase voltage measurement.

In Figure 3-11, steady-state phase currents look very similar. The amplitude of fundamental component of the phase current when simulated with emulator is 0.5 % higher. Some difference in the two currents can be observed around zero crossing when the amplitude is between 100 A to -100 A. The line voltage between the two simulations also has very small difference. The amplitude of the fundamental component of voltage when tested with emulator is again higher by 1.5 %. Similarly, the active and reactive power also differ by a small amount between the two simulations. The average active and reactive power in the emulator test is 0.6 % and 0.2 % higher compared to the simulation with a PMSM. Overall, the difference between the emulator and drive are very small and barely noticeable in the figure. The common-mode current observed in simulation is presented in Figure 3-12 (a). The amplitude of the common-mode current is 4.5 % of the fundamental component. The common-mode controller is effective in eliminating the DC component. However, the 3rd harmonics are still present which has an amplitude of 10 A.

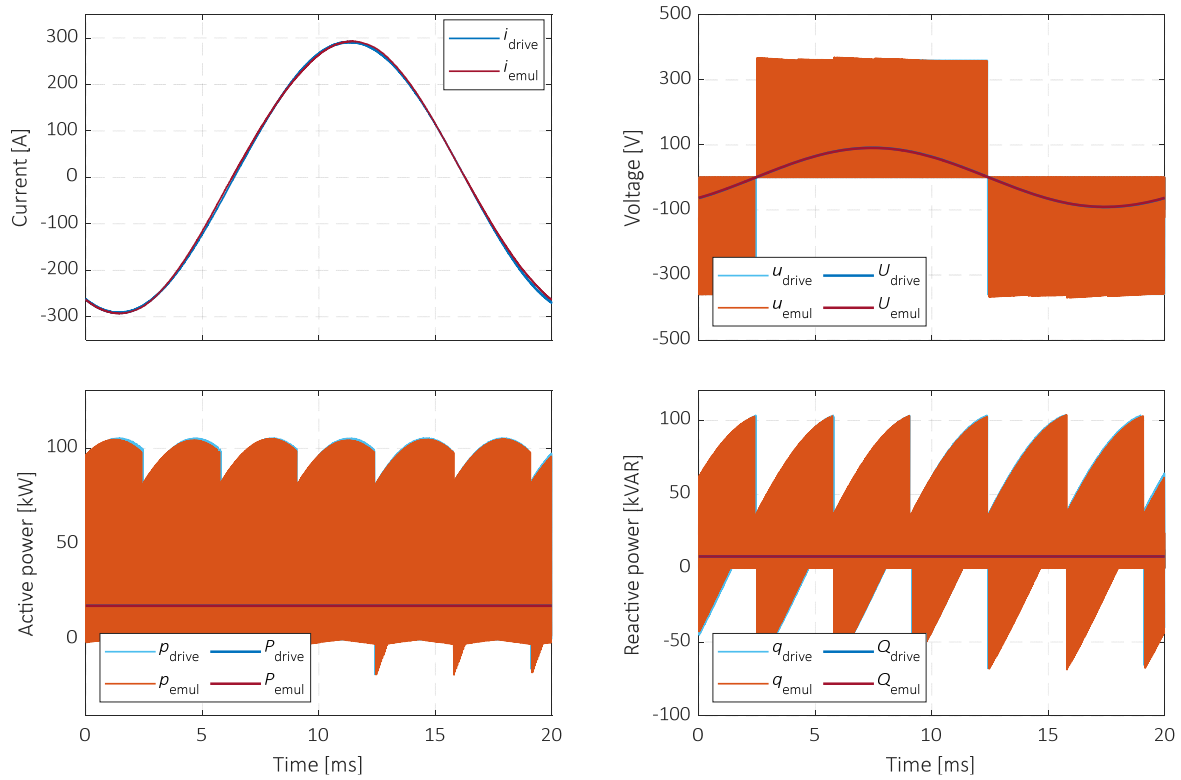


Figure 3-11: Comparison of steady state simulation results of IUT when simulated with PMSM and emulator for an operating point at 750 rpm and 180 Nm.

In Figure 3-12, the difference in phase currents looks higher than the previous case. However, the fast Fourier transform (FFT) shows that difference between the fundamental component of the phase currents of the emulator and drive are almost zero. It can be observed in the figure that the phase current in emulator is more distorted compared to the drive because the phase current in case of the emulator has higher harmonics. The common-mode current for this operating point is shown in Figure 3-12 (b). It can be observed that compared to Figure 3-12 (a), the common-mode current is almost four times higher. The common-mode controller is effective in eliminating the DC component. However, the 3rd harmonics are still present which has an amplitude of 40 A. The higher common-mode current explains the higher harmonic content of the emulator current. The line voltage in the two simulations has a similar characteristics as earlier operation point. The difference in the fundamental component between the two simulation is around 2 %. Similarly, the average active and reactive powers between the two simulations differ by 0.4 % and 2 % respectively. The small differences in between the two simulations are due to the presence of common-mode currents. In the two operating points discussed, the maximum amplitudes of common-mode current w.r.t to the fundamental phase currents are 4.5 % and 19 %. Although, the amplitude of the current between the two operating point is similar, the amplitude of the fundamental component of line voltage is higher in the second operating point. It shows that the common-mode current is directly depended on the applied voltage. Therefore, it will have a larger influence on the voltage and currents as the fundamental frequency of the current or the rotor speed increases. The common-mode currents could be eliminated completely in

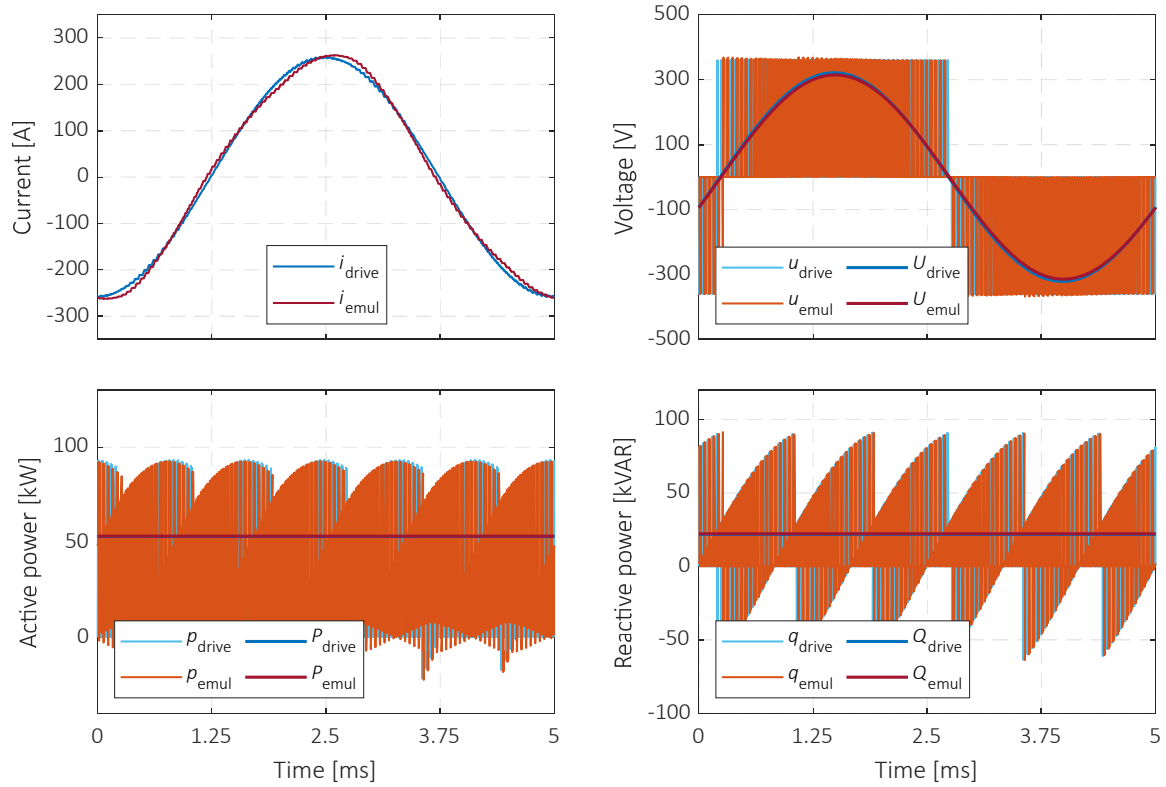


Figure 3-12: Comparison of steady state simulation results of IUT when simulated with PMSM and emulator for an operating point at 3000 rpm and 160 Nm.

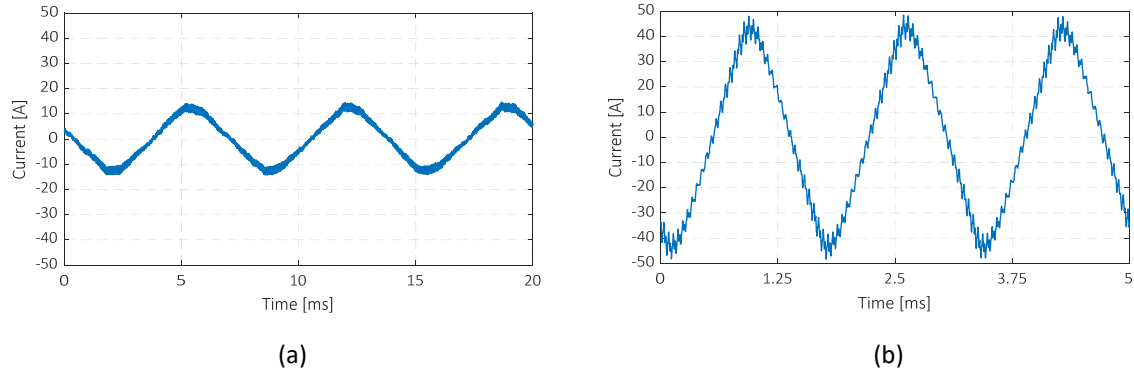


Figure 3-13: Common-mode current observed in simulations of the two operating points: a) 750 rpm and 180 Nm and b) 3000 rpm and 160 Nm.

simulation by modeling a common-mode choke. However, that would prevent in understanding the limitation of the common-mode controller utilized.

Further simulations are performed at various operating points of the machine. The results of these simulations are summarized in Figure 3-14. A difference in phase voltage or current will affect the active and reactive power supplied by the IUT. Therefore, a comparison of active and reactive power between the emulator and the PMSM drive can be used to characterize the performance. The average active and reactive power supplied by the IUT when tested with PMSM and machine emulator are compared. Simulations are performed for various load torque and three different speeds: 750 rpm, 3000 rpm and 4500 rpm. The difference in the

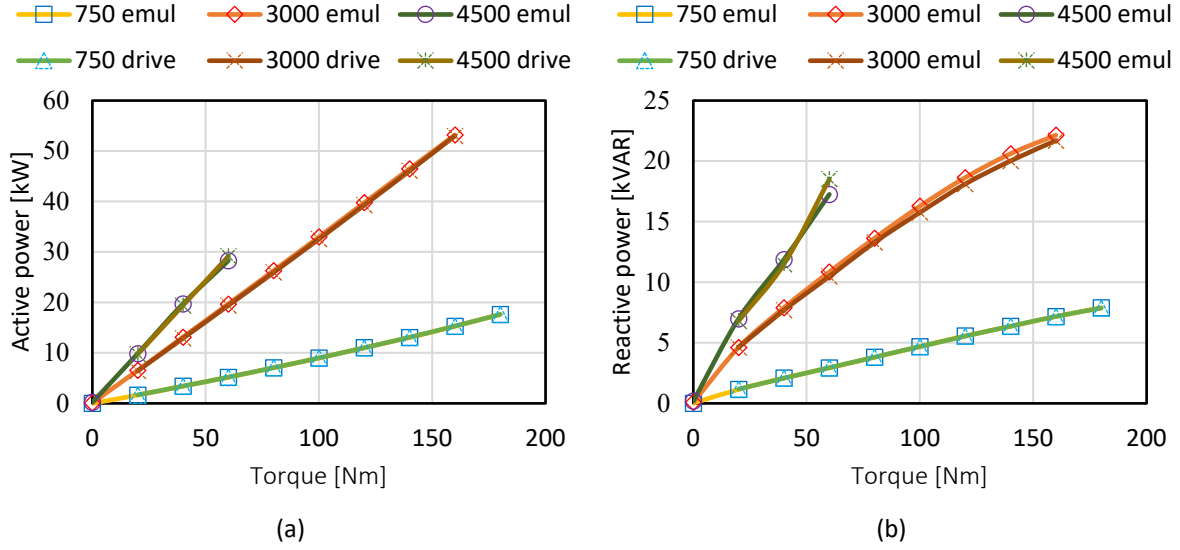


Figure 3-14: Steady state comparison of average a) active and b) reactive powers between simulation of IUT with PMSM and machine emulator for various operating points of the machine

average active power consumption between the two simulations in steady state is less than 2 % for all the operating points. However, the reactive power consumption differs slightly higher, almost 3.5 %. The higher difference in reactive power consumption can be attributed to the common-mode currents shown earlier because the common-mode current does not result into active power consumption.

3.3.2 Dynamic performance

The dynamic performance of the emulator is evaluated, and the results of the simulations are presented in Figure 3-15. In simulations, first rotor speed is ramped by applying a speed reference at 0.05 s followed by a load torque step at 1 s. The steady-state rotor speed and load torque are 3000 rpm and 160 Nm. A similar approach as earlier is followed. The IUT simulations with PMSM are compared to that from emulator setup. In the figure, first subplot from top presents a comparison of rotor speed. The speed reference is indicated by 'ref', rotor speed of the PMSM by 'drive' and estimated rotor speed of the emulator by 'emul'. Second subplot from the top presents electromagnetic torque and load torque. The legend marked 'load' represents load torque reference while 'drive' and 'emul' indicate electromagnetic torque of the PMSM and calculated torque in the emulator, respectively. Third and fourth subplot show d- and q-axis currents and d- and q-axis voltage references of the IUT current controller. Since losses of the VSC are not modeled, voltage references and actual voltages at the terminals can be assumed to be identical. In the figure, legends ' i_{DD}' ', ' i_{qd}' ', ' u_{dd}' ' and ' u_{qd}' ' are currents and voltages of the IUT when simulated with the PMSM. Similarly, ' i_{de}' ', ' i_{qe}' ', ' u_{de}' ' and ' u_{qe}' ' are when simulated with the emulator. A fifth subplot shows amplitude of voltage vector and maximum available phase voltage. ' U_{IUT}' ' and ' U_{Emul}' ' are amplitudes of the voltage of the IUT and VSC inside the emulator.

In Figure 3-15, the rotor speeds between the two simulations are almost identical. The difference in rotor speed between the two simulations is less than ± 2 rpm which is very small.

Similarly, the torques in the two simulations also look very similar with a small error which is less than ± 2 Nm. The d- and q-axis currents between the simulations also vary like the torques. The maximum differences between the two d- and q-axis currents are less than ± 3 A. The d-axis currents have slightly higher difference than q-axis. On the contrary, the d- and q-axis voltages deviate slightly higher. The difference between the two d-axis voltages is around ± 6 V and the q-axis voltages around -8 V to 4 V. The amplitude of the voltage vectors in both the emulator and IUT are below the maximum available voltage. The small differences in voltage and currents could be the result of the common-mode currents as explained earlier.

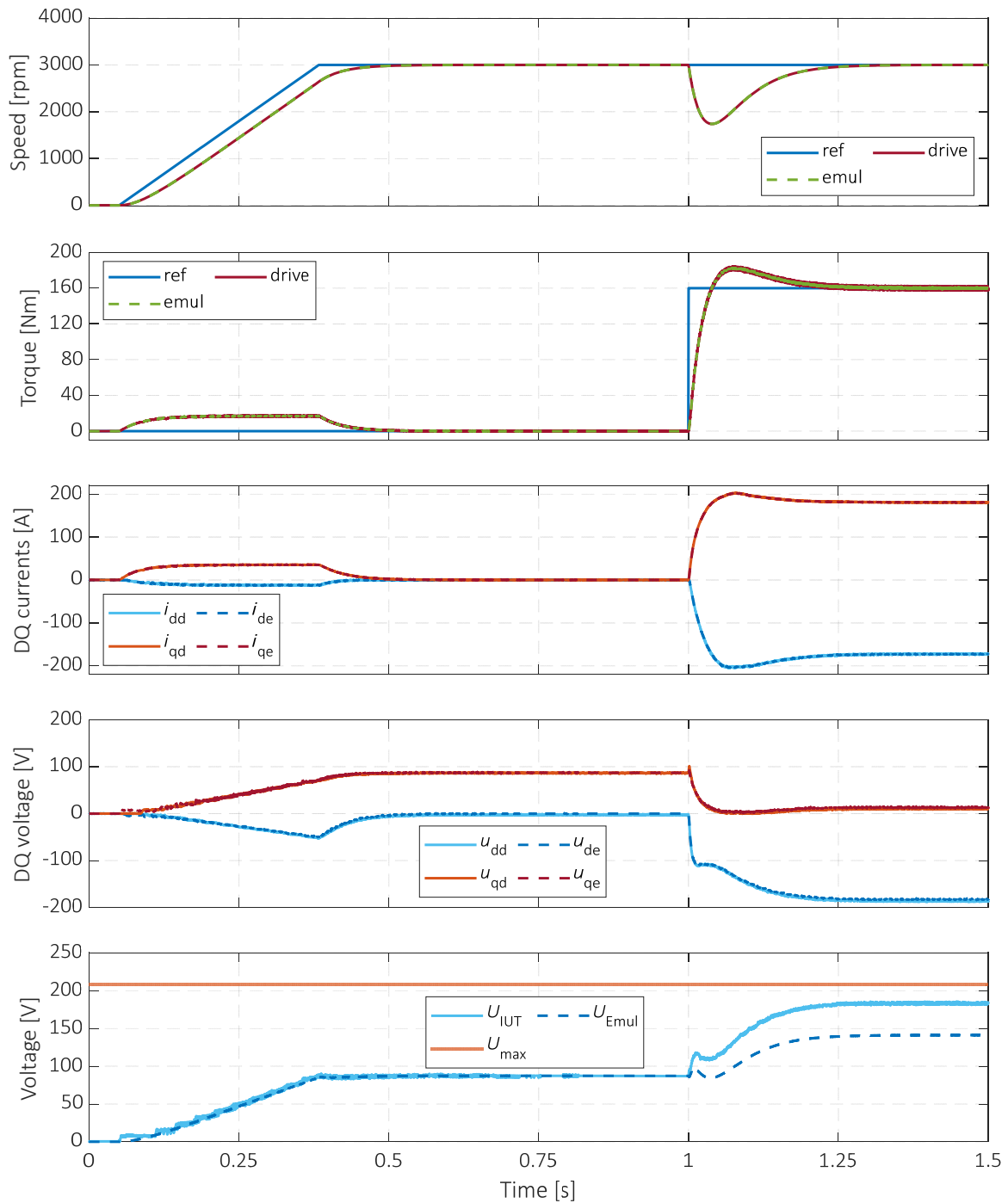


Figure 3-15: Comparison of simulation results when the IUT is simulated with PMSM and emulator. A speed reference of 3000 rpm is applied at 0.05 sec followed by a load torque step of 160 Nm at 1 sec.

Chapter 4

Experimental Evaluation of a Machine

Emulator

A machine emulator is built by prototyping two voltage source converters and three single-phase inductors. The design of the single-phase inductor is discussed. It is followed by a brief description of the voltage source converter. Then experimental results from the test bench are compared to simulations of the inverter with a PMSM. Both steady-state and dynamic performance is analyzed. Furthermore, the challenges associated with open loop control are discussed as well. The measurements from a PHIL test bench are also compared to a physical machine in a dynamometer test bench.

4.1 Coupling network

Three single-phase inductors are considered as coupling network. Design requirements of the single-phase inductor are presented in Table 4-1. The requirement for inductance is the same as used in simulations in Chapter 3. In simulations, the inductance was considered constant. However, the inductance will change due to saturation of the iron-core. Therefore, it is very important to limit variation of the inductance to avoid challenges in control of the emulator VSC. The maximum RMS current of the inductor is limited to 10 A/mm^2 which eliminates the need to consider forced convection or liquid cooling of the inductors. The maximum frequency is selected based on the emulated machine which is the same PMSM presented in previous chapter.

A core with a uniform cross section as shown in Figure 4-1 is used. It can be observed from the figure that the core consists of two parts with "I" shaped upper section and "E" shaped lower section. The air gap is placed in the middle leg for ease of prototyping. Laminated silicon

Table 4-1: Design requirements of the inductor

Parameter	Value	Unit
DC-link voltage	360	V
Maximum fundamental frequency	600	Hz
Maximum RMS current (for 30 s)	230	A
Maximum current density (for 30 s)	10	A/mm ²
Inductance	0.4	mH

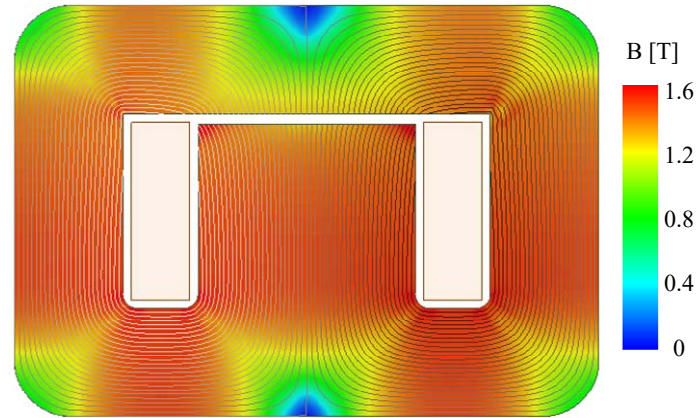


Figure 4-1: 2-D cross section of the single-phase inductor showing the flux density distribution and flux lines calculated using FEM with maximum RMS currents in the coil.

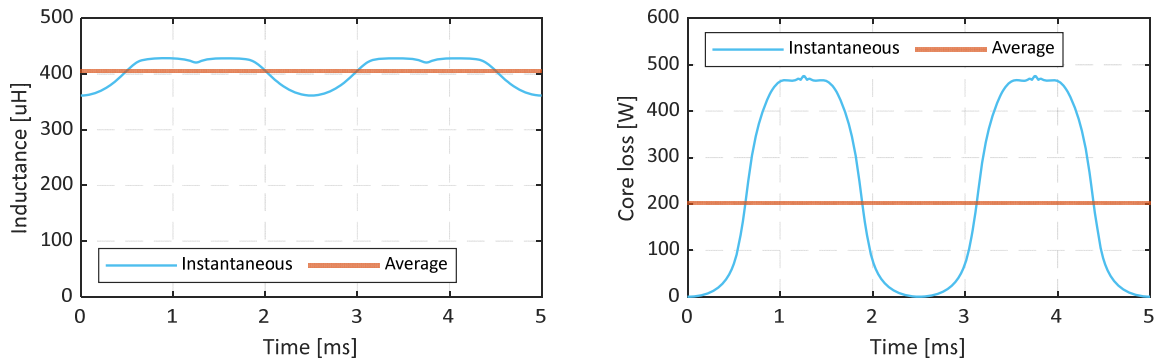


Figure 4-2: Inductance and core loss calculated from FEM with maximum RMS currents in the coil (230 A) and fundamental frequency of 200 Hz.

steel (SURA M235-35A) is used to keep iron-core losses low. A basic analytical design of the inductor is performed to estimate the overall dimensions. A more detailed design is performed using FEM simulations in Ansys Maxwell. Air gap length and number of turns are varied to reduce the peak-to-peak inductance while meeting the design requirement for average inductance. The flux density distribution and flux lines calculated from FEM at maximum RMS current in the coil are also shown in the figure. It can be observed that the maximum flux density in the core is around 1.6 T. The material of the core has a saturation flux density of 1.8T. Therefore, the maximum flux in the core is limited to 1.6T. In addition, the saturation of the core is uniform in most parts except at the corners and the middle of the two sections. As can be seen, the coils are enclosed by the core. Flux produced by the coil is divided equally between the two outer legs.

Instantaneous and average inductances calculated from FEM for maximum RMS current in the coils are shown in Figure 4-2. The fundamental frequency of current is 200 Hz. The average inductance is around 0.4 mH with a peak-to-peak variation of 16 %. The variation of inductance is caused by the variation of relative permeability of the core material w.r.t flux density. The variation of the inductance is found to be inversely proportional to the airgap length. However, increasing the airgap will lead to an increased reluctance which will reduce the inductance of the coil. Therefore, the peak-to-peak variation is inversely proportional to

the core size. Core loss are calculated for two fundamental periods and the result of the second period are shown in the figure. The core loss varies from 0 to 475 W with an average of 200 W. The core losses and the copper losses will influence the thermal performance of the inductor. Therefore, it is necessary to minimize the total losses.

The parameters of the inductor from the design are presented in Table 4-2. The average inductance at both no-load and full load meet the design requirements. The fill factor of Cu is low to make it easier to wind the coil by hand. The total loss of the inductor at the maximum operating frequency are around 1.2 kW. The total mass of the inductor could be reduced if forced cooling was considered.

The prototyped inductor is shown in Figure 4-3. The inductor core is shown in Figure 4-3(a) and the final assembled inductor with the coil is shown in Figure 4-3(b). Litz wire are used in

Table 4-2 Parameters of the final inductor design considered for prototyping

Parameter	Value	Unit
Length of core	80	mm
Width of core	210	mm
Height of core	148	mm
Air gap	3.6	mm
Wire diameter	6.8	mm
Number of turns	13	
Fill factor of Cu	28.4	%
Inductance at no load	0.4	mH
Average inductance at 230A RMS	0.4	mH
Core loss at 230A RMS and 600 Hz	964	W
Phase resistance	3.21	mΩ
Cu loss at 230A RMS	170	W
Mass of Cu	1.11	kg
Mass of iron	16.4	kg



Figure 4-3: Prototyped inductor a) core, b) core assembled with coil in housing

to make the coils because these wires have low ac losses. Therefore, the dependency of resistance of the coils on frequency can be neglected in control. Paper insulation is used between the coils and the inductor core as shown. The two sections of the core are fastened using a metal tie clip. The assembled inductor is housed inside a steel box to reduce electromagnetic interference (EMI) issues resulting from the non-shielded coils.

4.2 Voltage source converter

A 2-level voltage source converter with SiC based XM3 half-bridge power module is prototyped. The design of the VSC is presented in [48]. The prototyped VSC is shown in Figure 4-4 with some key parameters listed in Table 4-3. The VSC is liquid cooled as can be seen in the figure. Current sensors with voltage-based output are used for measurement of phase current. However, during the control of the emulator external high bandwidth sensor are used due to EMI in current measurement. The same control strategy with identical control parameters as used in simulations is implemented.

4.3 PHIL test bench

Table 4-3: Parameters of the prototyped voltage source converter

Parameter	Value	Unit
DC-link voltage	360	V
Switching frequency	20	kHz
Maximum RMS current	320	A
Power module	CAB425M12XM3	

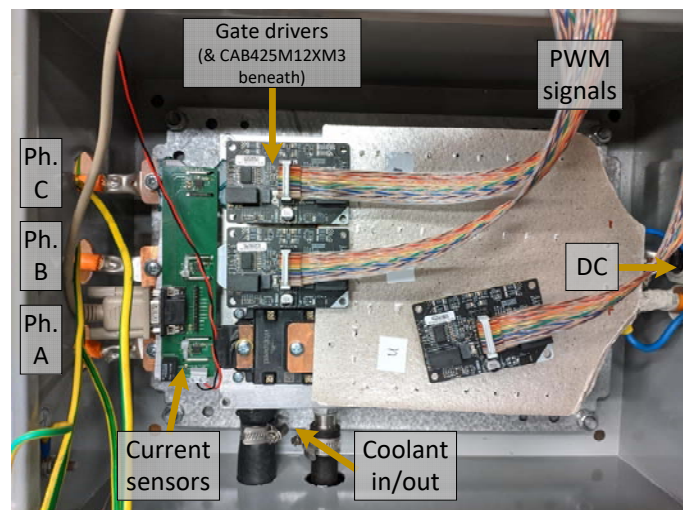


Figure 4-4: Prototyped 2-level voltage source converter with SiC based XM3 half-bridge power modules.

The machine emulator is tested by prototyping a PHIL test bench as shown in Figure 4-5. The test bench schematic is the same as that used in simulations. It consists of two identical VSCs connected back-to-back to the same DC link. As mentioned, this puts less requirement on the power supply since only the loss in the setup needs to be supplied by the power supply. Two

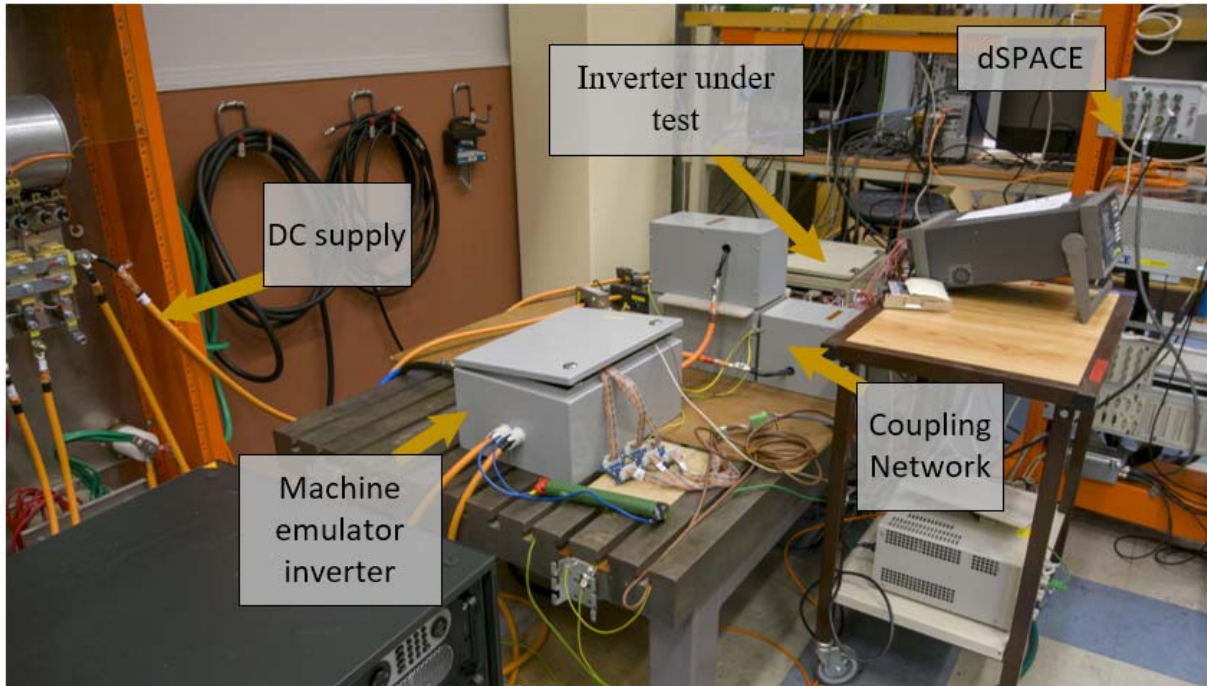


Figure 4-5: The back-to-back PHIL test bench used for experimental evaluation of machine emulator

sets of the VSC are shown in Figure 4-5. One of the VSC is used as IUT while the other VSC is used in the machine emulator and is referred to as the machine emulator inverter in the figure. Control of IUT and emulator are implemented with the same real-time processor RT1005 from dSPACE. This eliminates the need to synchronize the control of the two VSCs. In addition, speed and angle information can be exchanged within control blocks. External current sensors are used for current measurement as mentioned before and are shared between the emulator and IUT. Measurement results of IUT from test bench are compared to simulation of IUT with the 60 kW PMSM presented in the previous chapter.

Unlike in simulations, a slightly different control method is used for reducing the common-mode currents in experiments. First, the same PI controller as used in simulation is used to regulate the DC and low frequency components of the common-mode currents [52], [48]. The reason is that it was found to be effective in eliminating the DC component in simulations. Second, a modified space vector modulation (SVM) is used to regulate the higher frequency components. In the modified SVM, the dwell times of zero vectors are adjusted accordingly to reduce the zero-sequence currents [48].

4.3.1 Steady-state performance

In Figure 4-6, steady-state oscilloscope measurement from PHIL test bench is compared with simulation of the PMSM drive. The rotor speed and load torque are 3000 rpm and 100 Nm, respectively. Lower cases are used for variables when denoting instantaneous quantities while upper case for fundamental or average. Four subplots are shown from top: phase current, line voltage, active and reactive power supplied by IUT. The powers are calculated using instantaneous phase voltage and phase currents measurement on three phases. The line voltage shown in figure is derived from phase voltage measurement.

Steady-state phase currents look almost identical with the maximum difference in amplitude of less than 6 A or 3.5%. The measured current is higher than the one in simulation because the active power in measurement is also higher than simulation. More specifically, the average active power in measurement is 1 kW or 3% higher than simulation. The difference in active power is due to the estimation error in phase resistance of coupling network and omission of the iron-core loss of inductor in the control.

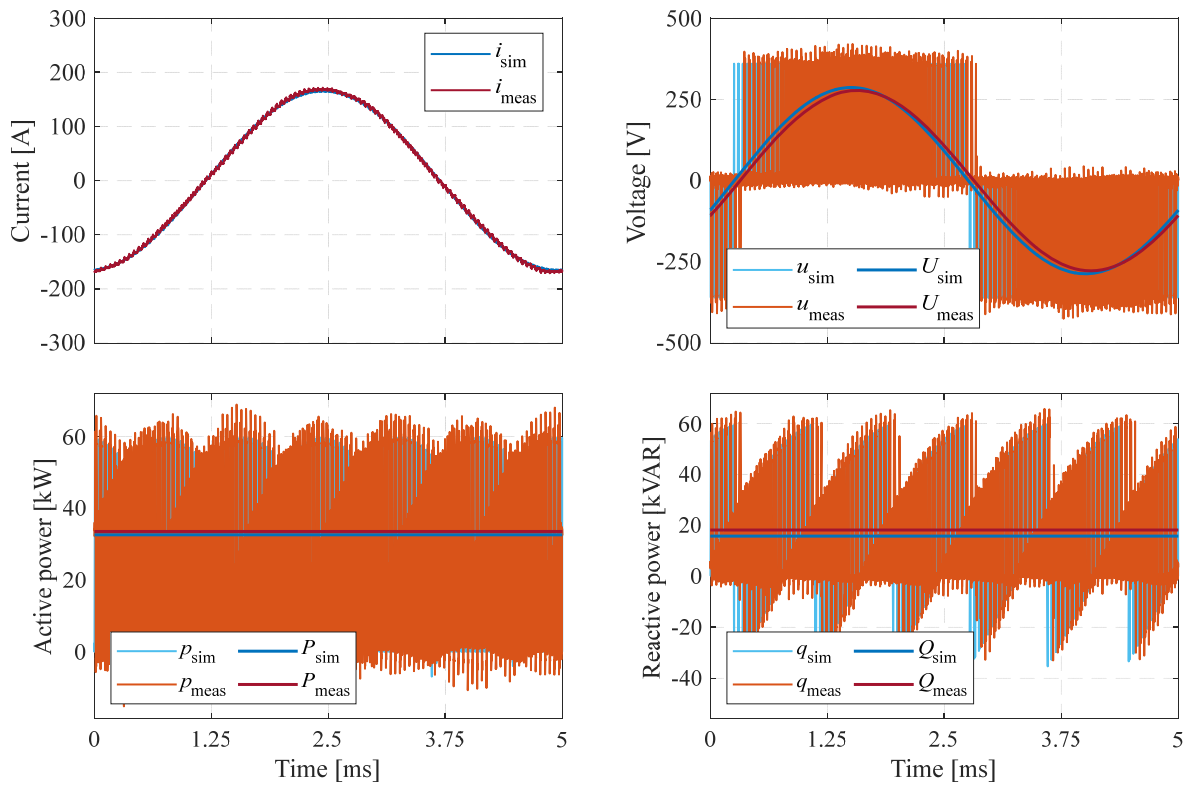


Figure 4-6: Steady state comparison of phase currents, line voltages, active and reactive powers between simulation and experimental measurement. The rotor speed and load torque are 3000 rpm and 100 Nm, respectively.

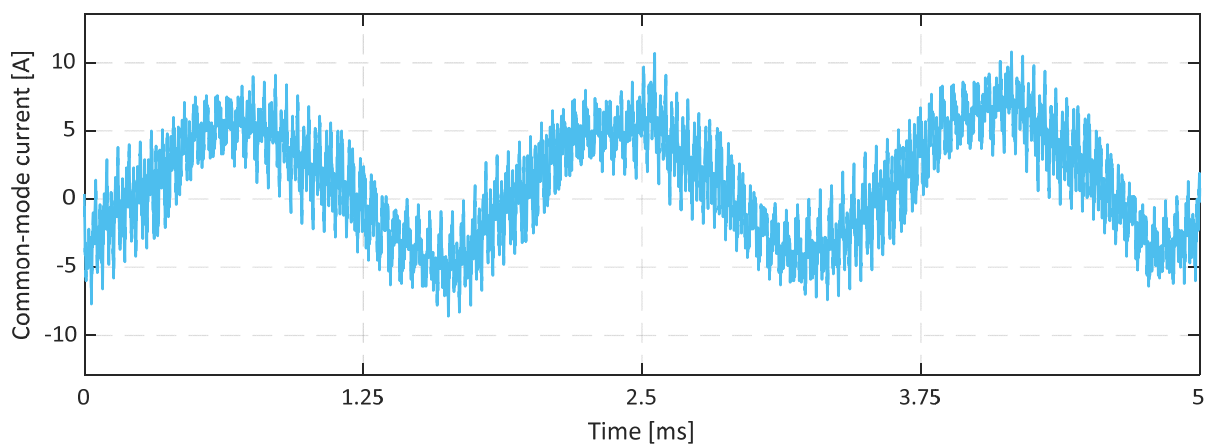


Figure 4-7: Steady state measurement of the common-mode current. The rotor speed and load torque are 3000 rpm and 100 Nm, respectively.

There are visible differences in the line voltages and the reactive powers. The line voltage in simulation is leading the measured value by almost 9° . In addition, fundamental component of voltage in simulation is approximately 9 V or 3% higher than measurement. Furthermore, the average reactive power in measurement is higher than simulation by 2.5 kVAR or 13%. The difference in phase angle between simulated and measured line voltage is due to estimation error in phase resistance and losses in inductor as mentioned above. The difference in phase angle and amplitude between simulated and measured line voltage are mainly caused by parameter estimation errors e.g., the value of inductance, resistance of the coupling network and iron-core losses. The resistance of the coupling network is very small. Therefore, the error due to parameter estimation will be quite small compared to inductance or iron-core losses. The inductance is estimated by calculating impedance using phase voltage and phase current measurements at two ends of coupling network. Measurements are performed at steady state across multiple operating points. An average value of the inductance is then used. The measurement results presented in the figure are using the corrected inductances. However, as seen, there is still some difference in amplitude. This is because the average inductance might still have small deviations from the real inductance value at each operating point. Furthermore, the omission of iron-core losses in the control of the emulator will affect the voltage accuracy. Since, the phase currents have very small error, the difference in reactive power between simulations and experiments will depend mainly on the voltages.

The common-mode current at the same operating point is presented in Figure 4-7. It can be observed that the DC component is effectively reduced and the common-mode current mainly consist of 3rd and higher order harmonics. The amplitude of the common mode current is around 2% of the fundamental current amplitude. Although the simulation at 3000 rpm was performed with 160 Nm torque, the line voltage amplitude in simulations as seen in Figure 3-12 is 20% higher than experimental results shown in Figure 4-6. However, the common mode current is much lower in comparison to simulations where the common-mode current amplitude was 19% of the fundamental current amplitude. In simulations, only the PI regulator was used. Therefore, the combination of the PI regulator and modified SVM is more effective in regulating the common-mode current amplitude.

Comparison of average active and reactive power in steady state between simulation and measurements at various torque and speed operating points is presented in Figure 4-9. Three different rotor speeds are selected: 1000 rpm, 3000 rpm and 5000 rpm. The load torque reference is varied at each speed to cover from no load to full load operation. The instantaneous power is calculated using three phase current and voltages. The active power between simulations and measurement has small error. The maximum error between the two active powers is less than 15%. The difference is due to estimation error in resistance, neglecting iron-core loss of the inductor in control and measurement inaccuracy. The error is larger for lower values of power because the losses as a percentage of the total power will be higher, and the accuracy of current and voltage measurement is lower. At higher powers above 7 kW, the error is less than 5%. However, the reactive power between simulations and measurement shows a significant difference. The maximum error in reactive power is around 21%. Unlike active power measurement, on average there is 13% error between the measurement and simulation at the different speeds. As mentioned, the reactive power is mainly affected by the voltages at the terminals of the emulator. Furthermore, the voltages

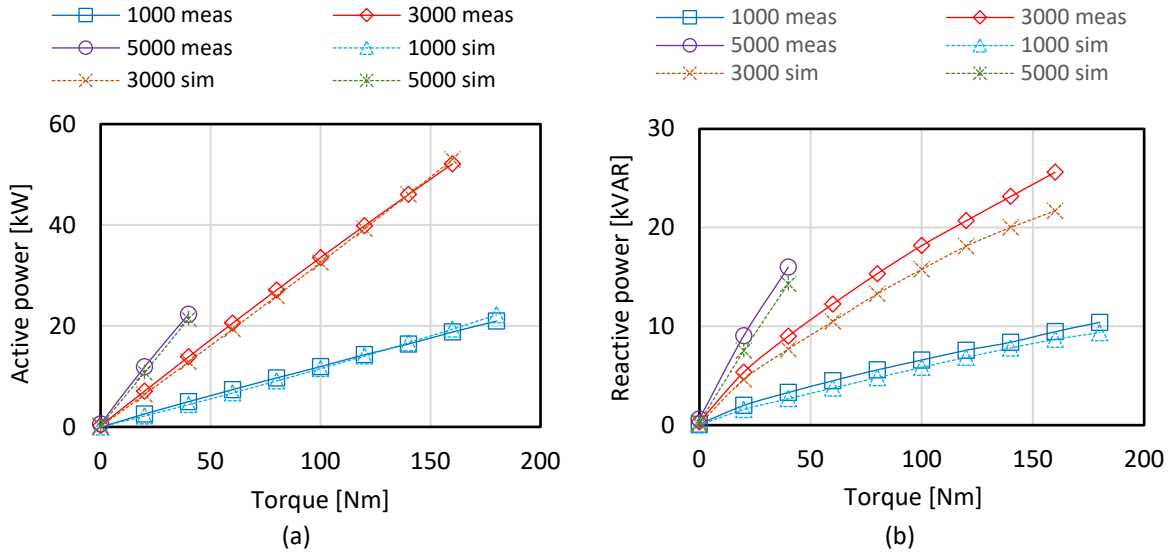


Figure 4-8: Steady state comparison of a) average active and b) reactive powers between simulation and experimental measurement for various operating points of the emulated machine.

are sensitive to estimation of coupling network parameters e.g., the value of inductance, resistance of the coupling network and iron-core losses.

4.3.2 Dynamic performance

The comparison of the dynamic performance between simulations and measurement is shown in Figure 4-9. Unlike the simulations, a ramp is used for load torque reference. The measurement results are obtained from Control Desk of dSPACE. In the figure, legends ' i_{ds}' ', ' i_{qs}' ', ' u_{ds}' ' and ' u_{qs}' ' are dq currents and voltages of the IUT when tested with PMSM in simulations. Similarly, ' i_{dm}' ', ' i_{qm}' ', ' u_{dm}' ' and ' u_{qm}' ' are referred to the measurement in PHIL test bench. D- and q-axis currents shown in figure are as seen by the current control. The d- and q-axis voltages in both simulations and measurements are controller voltage references.

It can be observed that rotor speed and torque have low frequency oscillations compared to simulations. This is mainly due to the speed controller. In addition, measured currents and controller voltages show high frequency oscillations. The prototyped inductors are not mechanically fixed to the housing as seen in Figure 4-3. Furthermore, no mechanical separators are used in the air gap. The inductor cores are fastened using a steel clamp which does not provide full mechanical damping. Therefore, the inductor cores vibrate. These vibrations can affect the equivalent airgap resulting in high frequency oscillations in currents.

Apart from the oscillations, the rotor speed in measurement lags the simulation. It is because, the torque in measurement also lags the simulation. However, it should be noted that the two results are synchronized for comparison in post processing. Therefore, the lag could be due to error in synchronization. In steady state, the simulated rotor speed is higher than measurement by a maximum of 10 rpm or 1%. However, the torque in measurement is slightly higher than simulation a maximum of 0.5 Nm or 2%. The higher torque in measurement is due to higher d- and q-axis currents. In steady-state, d- and q-axis currents in measurement

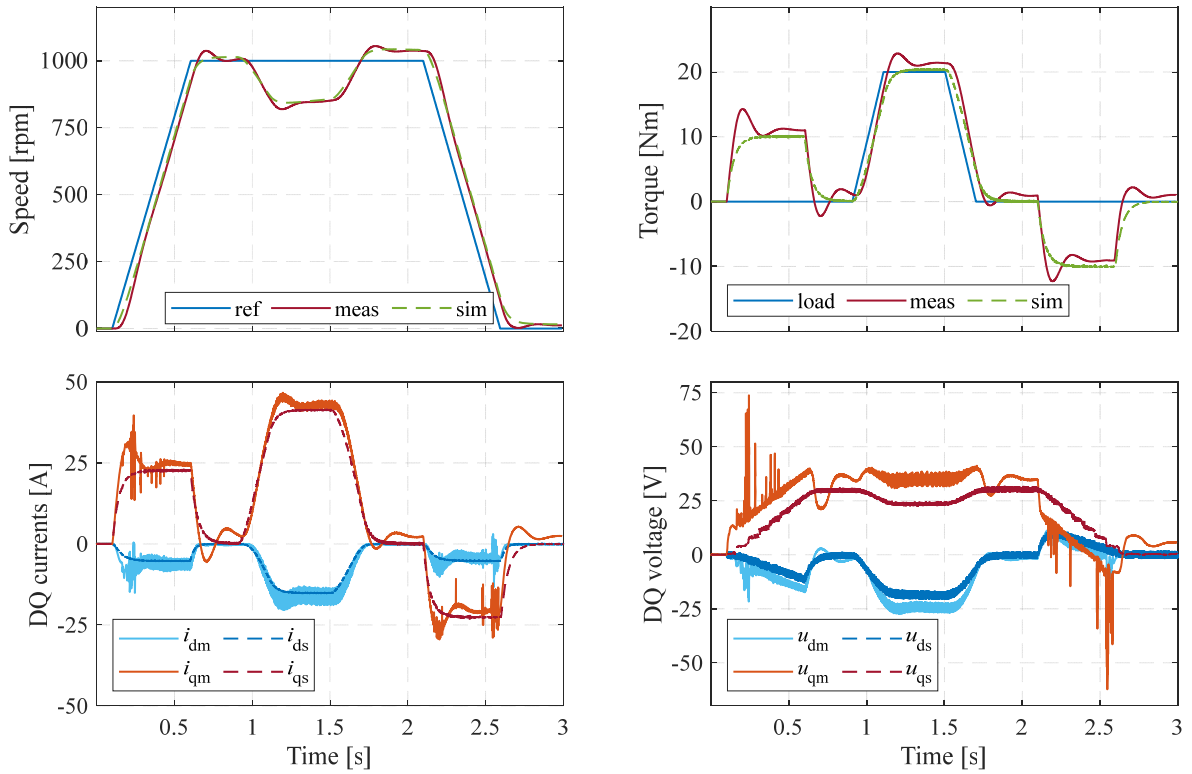


Figure 4-9: Comparison of emulated rotor speed, emulated load torque, dq-currents, and dq-voltages of controller between simulation and experimental measurement.

are 2-3% higher than simulation. The difference in steady state d- and q-axis voltages is due to mismatch of inductance estimation. As mentioned, an average value of inductance is estimated over a wide operating range which might have small deviations from the real inductance value at each operating point. Furthermore, the voltage drop across the switch is not considered in the controller. Therefore, the estimation of d- and q-axis voltages using the controller voltage reference will have error. Nonetheless, this error is small as the MOSFETs used in the inverter have very low drain-source on-state resistance of 4.6 mΩ. The maximum RMS current of the PMSM modeled in this work is 230A which results into a maximum voltage drop across the switch of 1.5V.

4.4 Comparison with a PMSM drive

The performance of the emulator in previous section is compared to simulations of a PMSM. In this section, the emulator performance is compared to a real PMSM using a dynamometer test bench as shown in Figure 1-3. A dynamometer test bench typically consists of two electric machines driven by two inverters. One of the drives is referred as traction drive and the second as load drive. The load drive is sometimes also referred as a dynamometer. The dynamometer test bench seen in Figure 1-3 is prototyped and used in the experiments. The experimental setup is presented in Figure 4-10. It consists of two identical PMSMs supplied via two identical 2-level VSCs. The traction PMSM is on the left of the image whereas the load PMSM is on the right with their respective inverters. The DC supply and a real-time processor from dSPACE for control implementation is also shown. The control of both traction and load PMSM are implemented in the same real-time processor. This allows using a single

encoder/resolver for field-oriented control. A torque transducer is also visible in the setup. However, the torque transducer is not utilized as it had severe EMI issues.

The VSCs used in the test bench are identical to that shown in Figure 4-4. In addition, the PMSMs in the dyno test bench have the same parameters as listed in Table 3-1. A back-to-back configuration is created by connecting the two DC-links of the VSCs to the same external power supply. As explained, this puts less requirements on the power supply since it needs to only supply the losses in the setup. A cascaded control strategy is used for the load machine. The outer loop consists of a speed controller whereas a field-oriented control is utilized in the inner current control loop. The current references are calculated as look-up-tables from the FEM model of the machine using Cu-loss minimization as described in section 2.4.3. The traction machine is controlled using load torque reference. Like the load machine, current reference look-up-tables are used to generate the current reference from torque reference. An identical field-oriented current controller is then utilized.

4.4.1 Flux linkage estimation

In [46], the flux linkages are calculated from steady-state experimental measurements. Various combinations of d-and q-axis currents are used in generator and motor mode to calculate the flux linkages. A specific measurement sequence is used to reduce the effect of temperature by choosing the d- and q-axis currents so that the time-averaged copper losses are almost constant. The measurements were performed at low rotor speed to minimize the effect of core loss. However, such measurements may not always be available as it requires special consideration. In addition, the measurement of core loss is necessary to use the flux linkages at a higher rotor speed. It may be difficult to separate the core losses in measurements from the total losses.

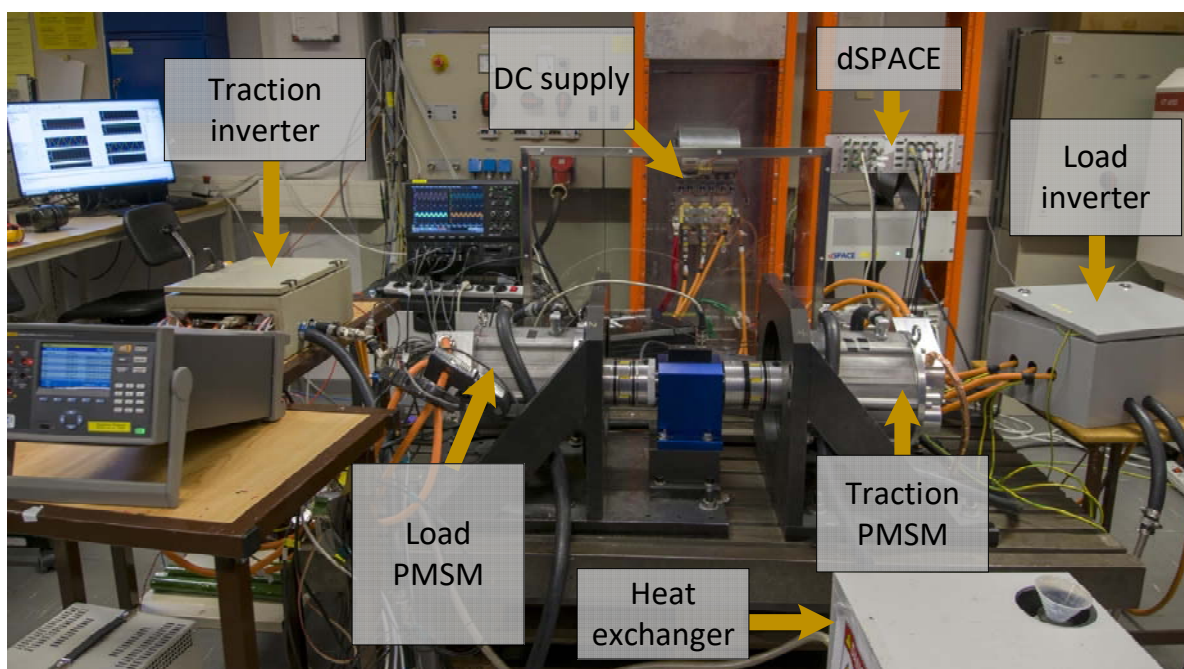


Figure 4-10: A dynamometer test bench with two identical PMSM drives

The steady-state measurement of the machine performance at various torque and speed operating point known as efficiency map is quite common [54], [55]. In [12], a method is proposed to identify machine parameters from efficiency maps. However, obtaining the efficiency maps would require measurement of shaft torque. As mentioned, direct measurement of torque in the test setup was not possible. Therefore, the flux linkages are calculated using (2-5) from steady-state measurement of currents and controller voltage references.

The d- and q-axis flux linkages of the load PMSM calculated from measurements are compared to interpolated flux linkages obtained from FEM simulations as shown in Figure 4-11. It can be observed from Figure 4-11(a) that the error between FEM and measurement is higher, around 30-50 % at low rotational speed of the machine. In addition, the error increases with torque. At low speeds and low torque, the magnitude of the back emf is small and the resistive voltage drop due to the q-axis current is dominant. Therefore, the calculation of flux-linkage is dependent on accurate estimation of resistance. At low speed and high torque, back emf is quite comparable to resistive voltage drop. Furthermore, resistance increases with temperature due to higher copper losses at higher torque and temperature was not recorded during this test. This results into the increase in error as torque increase. However, at higher rotational speed the error is significantly lower, e.g., at 2500 rpm the difference between FEM and measurement on an average is around 3 %. The reason is that the back emf is order of magnitude higher compared to resistive voltage drop at higher speed. In addition, measurement errors have less influence as the magnitude of the voltage increases.

Comparing Figure 4-11(a) and (b), the error in q-axis flux linkage at low speed and low torque is much smaller, around 20%. Since the current angle is closer to 90° at lower speed, the resistive voltage drop due to d-axis current is smaller. The error increases with torque like seen in d-axis flux linkage. As explained before, the resistive voltage drops starts becoming significant at higher torque and increased temperature due to higher copper losses. However,

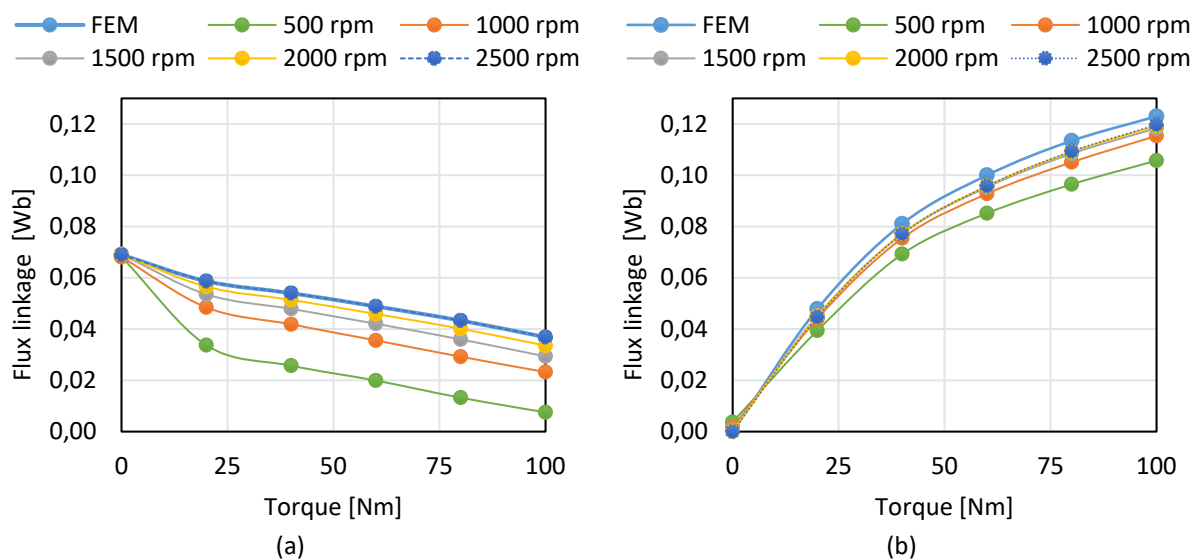


Figure 4-11: Steady state comparison of a) d-axis and b) q-axis flux linkages between FEM and experimental measurement for various torque and speed operating points of the PMSM.

since the amplitude of d-axis current is comparatively lower, the error is smaller compared to that seen in d-axis flux linkage. Like d-axis flux linkage, the measurement error is lower at higher speed, e.g., at 2500 rpm the difference between simulation and measurement on an average around 3 %. As mentioned in [46], the inverter non-idealities will result in errors in both d- and q-axis flux linkages as they are not considered in the measurement. They will have a larger influence especially at low rotational speed because the magnitudes of voltages are small. It can be observed that the flux linkages calculated using FEM simulations match well with measurements for high rotational speeds e.g., 2500 rpm. However, the comparison of the two at lower rotational speed e.g., 500 rpm is inconclusive without better measurements e.g., considering the effect of temperature on resistance and inverter non-idealities. Furthermore, the error due to core losses would need to be considered as the rotor speed increases.

4.4.2 Estimation of mechanical parameters

As explained before, the rotor speed and angle are estimated from (2-8) in the emulator. Therefore, the machine parameters such as the rotating inertia (J), viscous damping coefficient (B), and static friction torque (T_s) need to be estimated. In the experimental results the rotating inertia was estimated from the rotor design of the machine. However, when comparing the measurement results of the emulator with the PMSM in the dyno bench, the complete inertia should be used. It consists of rotating inertia of the two machine, torque transducer and bearings. Therefore, the rotating inertia needs to be estimated using experimental measurements. Similarly, B in the test bench would represent all the speed dependent mechanical losses including bearings. The estimation of viscous damping coefficient requires separation of mechanical losses from core losses which is difficult in case of PMSM. In [56], a rotor without permanent magnets is manufactured to measure the mechanical losses. Furthermore, the measurement of shaft torque is not available in the setup. Therefore, direct measurement of machine losses is not possible in the setup. The static friction torque which was neglected in the earlier measurements cannot be neglected in the dyno test bench. The static friction torque in experiments can be determined by finding the minimum q-axis current that when applied causes the rotor to start rotating. However, it is observed in measurements that the static friction torque is dependent on temperature. Hence, the measurement when repeated sequentially resulted in decreasing values of static friction co-efficient.

Therefore, the mechanical parameters in this work are estimated using curve fitting of experimental results. The results of the measurements obtained from the controller are shown in Figure 4-12. Four subplots are shown in the figure. The one from the top shows the q-axis reference and actual currents of the load machine. Similarly, that of the traction machine are shown in the second subplot. The rotor speed is shown in the third subplot. Finally, one of the phase currents of the load machine is shown in the fourth subplot. A q-axis current step is applied to the load machine while the traction machine operates with zero current references. It can be seen in the figure that at 0.5 s, the q-axis current reference is stepped up to 5 A and kept constant until it is removed at 5.5 s. This causes the rotor to accelerate until the current reference is removed. The d-axis current in the load machine is kept at zero during the whole test. The phase currents have the same amplitude as the q-axis

current but the frequency increases as the rotor speed increases. Since the d-axis current is zero, the torque can be estimated from (2-7). The d-axis flux linkage in the equation will be equal to magnet flux linkage which can be obtained by measuring the back emf at no-load. It is shown in Table 4-4. Since the current step amplitude is less than 1.5% of the maximum current and the frequency of current is low, the temperature of the magnet can be assumed to be constant. Since the q-axis current in the traction machine is zero, the load torque in the equation is zero. Then the rotor speed calculated from (2-8) can be fitted to the measurement

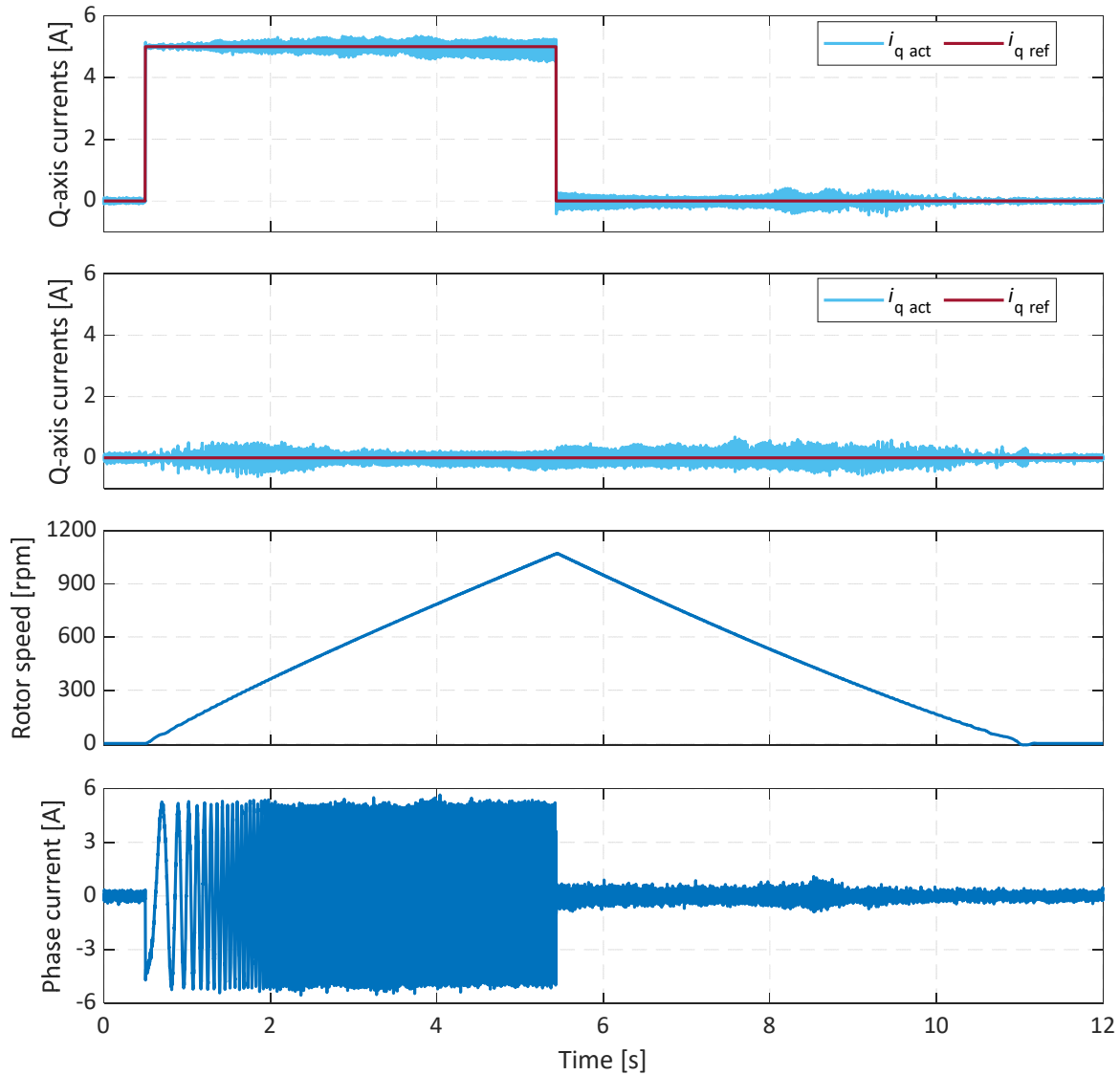


Figure 4-12: Evaluation of mechanical parameters using curve fitting. A q-current step is applied in the machine test bench.

Table 4-4: Parameters of the machine estimated from the measurements

Parameter	Symbol	Value	Unit
Magnet flux linkage	ψ_m	0.0694	Wb
Rotating inertia	J	0.047	kgm ²
Viscous damping co-efficient	B	8.93×10^{-4}	Nms/rad
Static friction torque	T_s	0.96	Nm

to obtain J , B and T_s . Since infinite solutions are possible, an optimization is used. In the optimization, the total RMS error between the calculated and measured rotor speed is minimized. The parameters obtained from the fitting are listed in Table 4-4.

4.4.3 Comparison of emulator and PMSM current and voltages

In Figure 4-13, steady-state oscilloscope measurements of the IUT when tested in PHIL test bench shown in Figure 4-5 are compared to the measurement of the IUT driving the traction machine in the dyno test bench shown in Figure 4-10. Measurement from the PHIL test bench is denoted by the subscript “Emul” and from the dyno test is denoted by the subscript “PMSM”. The rotor speed and load torque are 2500 rpm and 100 Nm, respectively. Since, the load torque is not measured in the bench, the reference torque used to control the traction machine is used. Lower cases are used for variables when denoting instantaneous quantities while upper case for fundamental or average. Four subplots are shown from top: phase current, line voltage, active and reactive power supplied by IUT. The powers are calculated using instantaneous phase voltage and phase currents measurement on three phases. The line voltage shown in figure is derived from phase voltage measurement.

The phase currents measured in the dyno test bench and the PHIL test bench are almost identical with a small difference of 2 A in the fundamental component. Since identical look-up tables are used to convert the load torque reference to current reference in both the test benches, the phase currents are almost identical. However, the actual torque in the dyno test bench should be lower because, as shown in Figure 4-11, the flux linkages estimated from the dyno test bench are lower. The line voltages on the other hand have big differences. The

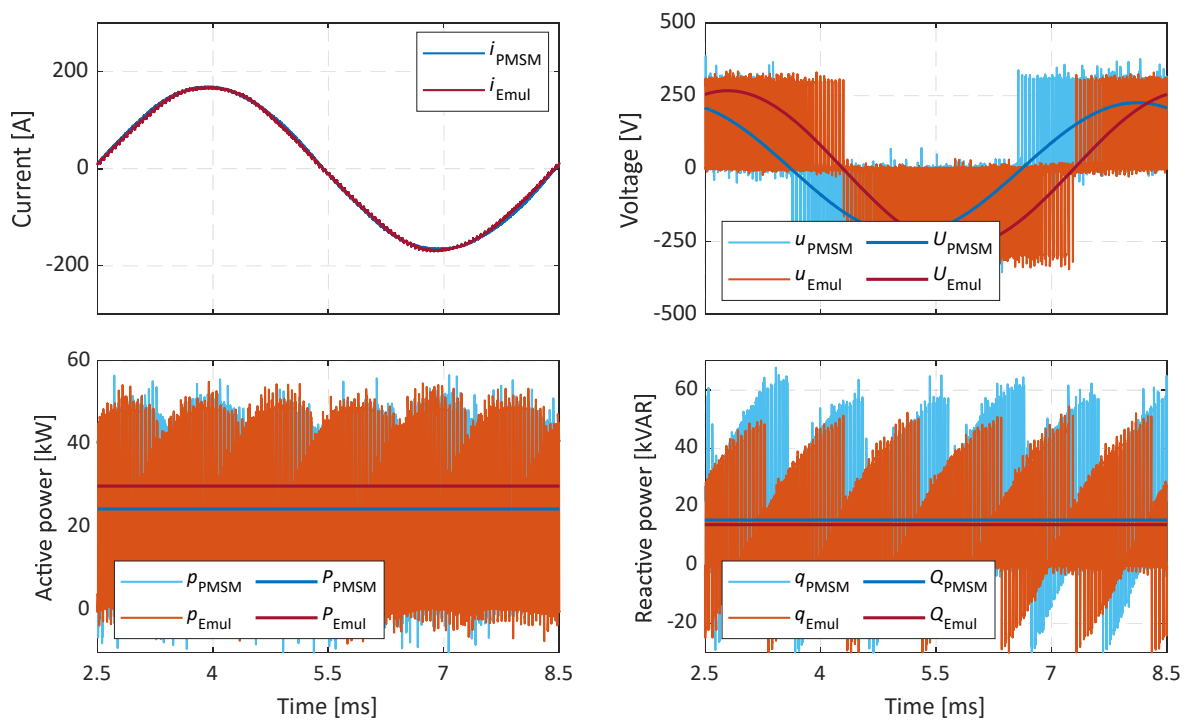


Figure 4-13: Steady state comparison of phase currents, line voltages, active and reactive powers between PMSM and emulator test bench measurement. The rotor speed and load torque are 2500 rpm and 100 Nm, respectively.

fundamental component of line voltage in the PHIL test bench is almost 16% higher than the dyno test bench. In addition, the line voltage measured in the PHIL test bench leads the line voltage measured in dyno test bench. The reason is that the flux linkages used in the PHIL test bench are generated from FEM which are overestimated as shown earlier. Therefore, the back emf will be higher in the PHIL test bench resulting into a bigger line voltage. The active power measured in the PHIL test bench is higher than the dyno test bench by 22% because the actual shaft torque in the dyno bench should be lower resulting in lower active power consumption. The active power will also be affected by the iron-core losses which are neglected in the control of emulator and the error in estimation of the copper and mechanical losses. The reactive power in the dyno test bench almost 7% higher than the emulator test bench. The reactive power depends mainly on the inductances of the machine. It shows that the inductances are underestimated in the model of the machine.

4.4.4 Steady state comparison of active and reactive power

Comparison of average active and reactive power in steady state between PHIL test bench and the dyno test bench at various torque and speed operating points is presented in Figure 4-14. Three different rotor speeds are selected: 500 rpm, 1500 rpm and 2500 rpm. The load torque reference is varied with a step size of 20 Nm from no load to 100 Nm. The instantaneous power is calculated using three phase current and voltages in both the cases. The active power in the PHIL test bench is always higher. The differences between the two setups are higher at low torque and 500 rpm. However, for speeds of 1500 rpm and 2500 rpm, the differences are on average around 8%. As explained, the differences in flux linkages were larger at low speeds and low torque and lower at higher speed and higher torque. Therefore, the estimation of torque will have a larger error at low speeds compared to higher speeds. The difference in the active power will also be influenced by the neglected iron-core losses and the estimated resistance and mechanical losses. However, the difference in the reactive power between two measurements show a different trend.

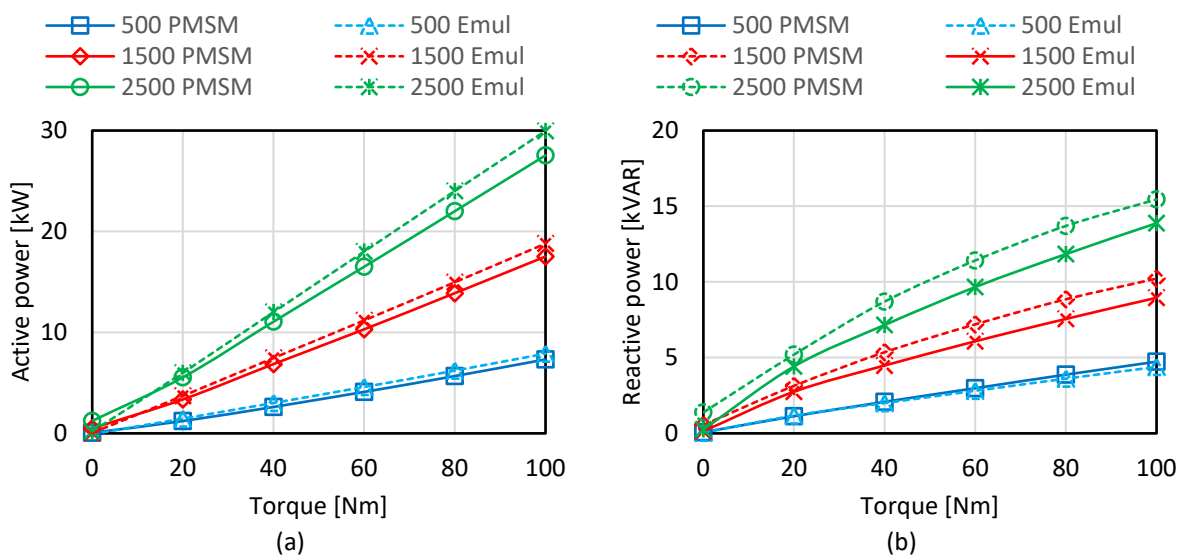


Figure 4-14: Steady state comparison of average a) active and b) reactive power between dyno test bench and PHIL test bench using experimental measurement for various torque and speed operating points of the machine.

Chapter 5

Design of a High Bandwidth Machine

Emulator

The bandwidth of the machine emulator refers to the maximum fundamental frequency of the current or the speed of the electric machine that can be emulated. First, the operating region of the machine emulator is analytically derived. It is followed by an analysis of the coupling network on the emulator operating bandwidth. A dimensioning method is proposed to size the coupling network inductance. The bandwidth of the emulator is then evaluated using simulations. The design of a high bandwidth emulator using transformers as coupling network is proposed. Simulations are used to verify the bandwidth of the proposed emulator.

5.1 Bandwidth of machine emulator

It can be seen from (3-15) that the voltage references of the emulator VSC need to account for the voltage drop across the coupling network. Therefore, the ability of the emulator VSC to produce the correct voltage could be limited especially when using a back-to-back configuration. Hence, evaluation of the bandwidth is necessary especially when the emulated machine is intended for traction or high-speed application.

5.1.1 Operating region of a machine emulator

In this section, the operating region of the emulator is analyzed in the dq-frame. The operating region of a PMSM in the dq-frame can be defined by using a voltage limit ellipse and a current limit circle [57]. A similar approach can be followed to derive the operating region of the machine emulator. The maximum phase voltage that can be produced by the VSC is given by

$$U_{\max} = \frac{U_{\text{DC}}}{\sqrt{3}} \quad (5-1)$$

where U_{DC} is the DC link voltage. Consequently, the operation of the emulator is limited by the available maximum voltage as

$$u_{d2}^2 + u_{q2}^2 = u_{s2}^2 \leq U_{\max}^2 \quad (5-2)$$

where u_{s2} is the amplitude of the voltage vector generated by the emulator VSC. In steady-state conditions and neglecting the resistive voltage drop, (5-2) can be written as

$$\psi_d'^2 + \psi_q'^2 = \left(\frac{u_s'}{\omega}\right)^2 \leq \left(\frac{U_{\max}}{\omega}\right)^2. \quad (5-3)$$

Substituting for flux linkages using (3-15) results into

$$(\Psi_m + L_d i_d - L_{CN} i_d)^2 + (L_q i_q - L_{CN} i_q)^2 \leq \left(\frac{U_{\max}}{\omega}\right)^2. \quad (5-4)$$

The above equation can be formulated as an ellipse at the boundary as

$$\frac{(i_d + I_{de0})^2}{a_e^2} + \frac{i_q^2}{b_e^2} = 1$$

$$a_e = \frac{U_{\max}}{\omega(L_d - L_{CN})} \quad b_e = \frac{U_{\max}}{\omega(L_q - L_{CN})} \quad (5-5)$$

$$I_{de0} = \frac{\Psi_m}{(L_d - L_{CN})}$$

where a_e and b_e are major and minor semi-axis and $(-I_{de0}, 0)$ is center of the ellipse. Similarly, the voltage limit ellipse of the PMSM (VLM) can be formulated as

$$\frac{(i_d + I_{d0})^2}{a^2} + \frac{i_q^2}{b^2} = 1$$

$$a = \frac{U_{\max}}{\omega L_d} \quad b = \frac{U_{\max}}{\omega L_q} \quad I_{d0} = \frac{\Psi_m}{L_d} \quad (5-6)$$

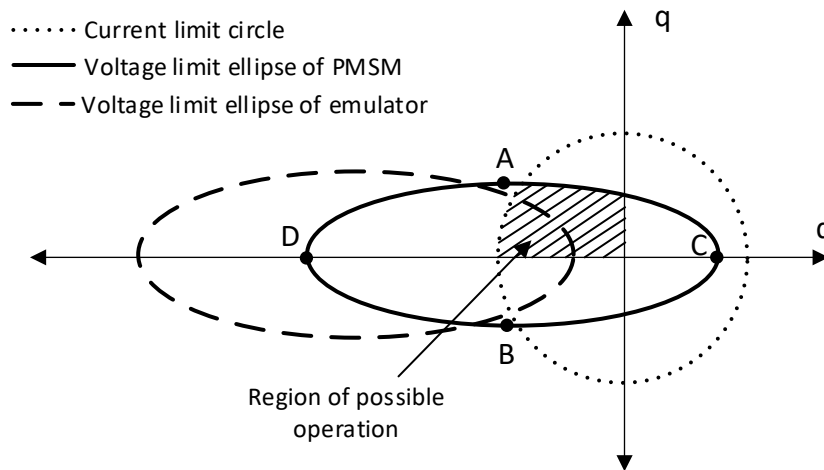


Figure 5-1: Schematic sketches of voltage limit ellipse of an emulator VSC and a PMSM along with the current limit circle.

where a and b are major and minor semi-axis and $(-I_{d0}, 0)$ is center of ellipse. The voltage limit ellipse of the emulator VSC (VLE) and PMSM are shown along with current limit circle (CLC) in Figure 5-1. As can be seen, VLE is shifted and stretched. Operation region of PMSM in dq-frame lie inside the common area between VLM and CLC in second quadrant. Similarly, operation region emulator is restricted in the common area between VLE and CLC.

5.1.2 Dimensioning of coupling network inductance

In the reviewed literature, selection of coupling network inductance has not been investigated analytically. In [14], coupling inductance was selected to be equal to leakage inductance of the armature winding on the dq-frame. As shown in [57], when using a separate DC link for emulator VSC, the bandwidth of emulator can be improved by controlling the DC link voltage. However, in the back-to-back PHIL test bench used in this work, controlling the DC link of the emulator will be limited by the voltage rating of the semiconductor switches. In this section, influence of coupling network inductance on the operating region in a back-to-back configuration with an uncontrolled DC link is discussed. In addition, a method to dimension the coupling network inductance is introduced.

The VLE at constant frequency based on various selection of inductance L_{CN} is presented in Figure 5-2. It can be seen in the figure that the selection of inductance has significant influences on shape and size of the voltage limit ellipse. For example, the voltage limit is given by two lines parallel to d- axis when the coupling network inductance is equal to d-axis self-inductance. Similarly, when it is equal to q-axis inductance, it is given by parallel lines to y-axis. To emulate the PMSM in the entire operating range, the operating area of machine must be enclosed by emulator. However, it is analytically difficult to determine the actual operating

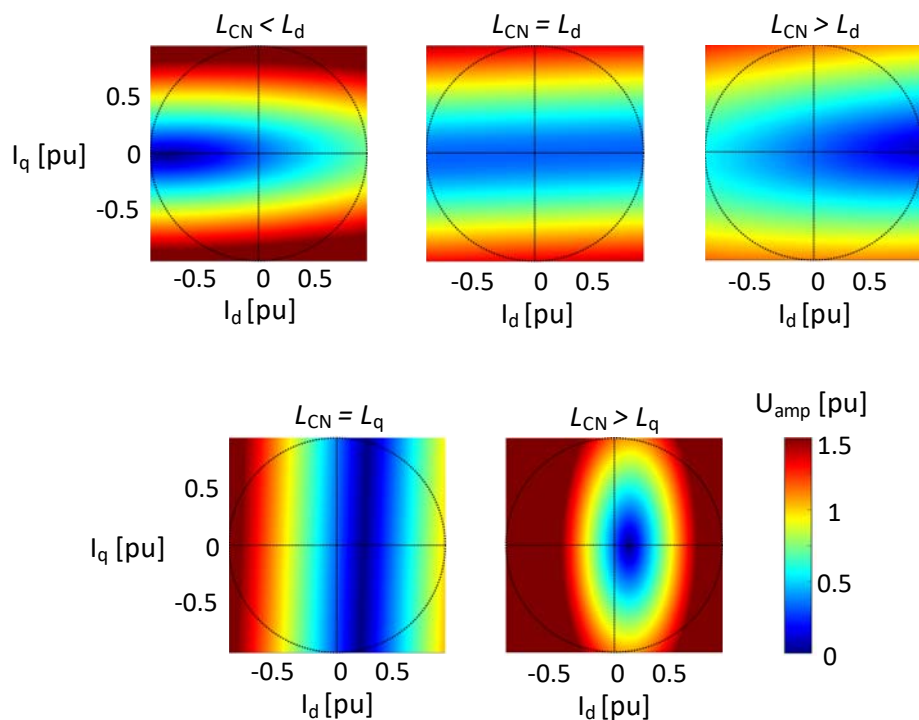


Figure 5-2: Phase voltage amplitude of an emulator VSC in dq-frame depending on the selection of coupling inductance. The dotted circle represents the current limit circle of the PMSM.

area of the machine since it is dependent on current reference selection strategy e.g., maximum torque per ampere etc. Furthermore, the inductances in (5-5) are not constant because of non-linear iron-core of the machine. Nonetheless, a sufficient condition can be derived by ensuring that the VLE encloses the VLM. This can be ensured by showing that the four points A, B, C and D in Figure 5-1 are enclosed by the VLE. The coordinates of the four points can be expressed as follows

$$A \quad (-I_{d0}, b);$$

$$B \quad (-I_{d0}, -b);$$

$$C \quad (-I_{d0} + a, 0);$$

$$D \quad (-I_{d0} - a, 0);$$

To check if a point (x_1, y_1) lies inside the VLE, the following inequality must be satisfied.

$$\frac{(x_1 + I_{de0})^2}{a_e^2} + \frac{y_1^2}{b_e^2} < 1 \quad (5-7)$$

Solving the inequality at points A and B results into following condition.

$$L_{CN} < \frac{2L_d}{\left(\frac{\omega \cdot \Psi_m}{U_{max}}\right)^2 \frac{L_q}{L_d} + \frac{L_d}{L_q}} \quad (5-8)$$

Similarly, solving it at points C and D results into following two conditions, respectively.

$$\Psi_m \omega < U_{max} \quad (5-9)$$

$$L_{CN} < \frac{2L_d}{1 + \frac{\Psi_m \omega}{U_{max}}} \quad (5-10)$$

It shows that the selection of inductance is sensitive to machine parameters and electrical frequency. Using, the inductances of the machine in the torque speed operating region, it is possible to determine the value of L_{CN} that satisfy the above inequalities. However, irrespective of the selection, point C is only enclosed if the no load back-EMF of the machine is less than maximum voltage. Nonetheless, (5-8) and (5-10) can be used as for selection of inductance.

5.1.3 Evaluation of the operating boundary

The operating boundary of the emulator can be evaluated analytically using (5-8) and (5-10). The d- and q-axis current reference of the machine are calculated in the entire operating region of the machine based on maximum torque per ampere (MTPA) control. The self-inductances and magnet flux linkage of the machine are obtained via interpolation of the inductance and flux linkage maps. Then, the maximum value of coupling network inductance that satisfy both inequalities (5-8) and (5-10), is calculated for the entire torque speed operating region of the PMSM. The ratio of the maximum value of coupling network w.r.t. the selected inductance in simulation i.e., 0.4 mH is presented in Figure 5-3. A value greater than

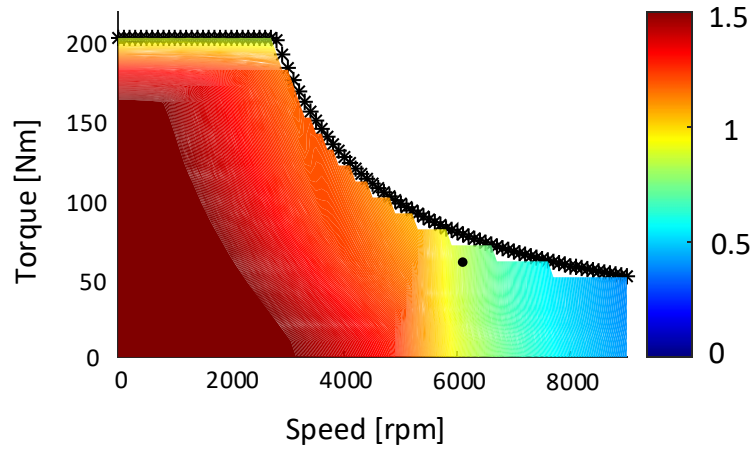


Figure 5-3: The ratio of maximum value of coupling network inductance w.r.t the value selected in simulation i.e., 0.4 mH.

one in the figure indicates that the selected inductance satisfies the inequalities. It can be observed that the inductance may limit operation of the emulator beyond approximately 6000 rpm. However, as mentioned choosing a very small inductance will increase common-mode current and may make control of current difficult. Simulations are used to verify the results shown in the figure.

The same simulation setup as presented in Chapter 3 is used. The result of the simulations is shown in Figure 5-4. The PMSM modeled in the simulation has a maximum speed of 9000 rpm as listed in Table 3-1. Therefore, an operating point around 6000 rpm and around 70 Nm, marked in Figure 5-3 with a dot, is used. In the figure, first subplot from top presents a comparison of rotor speed. The speed reference is indicated by 'ref', rotor speed of the PMSM by 'drive' and estimated rotor speed of the emulator by 'emul'. Second subplot from the top presents electromagnetic torque and load torque. The legend marked 'load' represents load torque reference while 'drive' and 'emul' indicate electromagnetic torque of the PMSM and calculated torque in the emulator, respectively. Third and fourth subplot show d- and q-axis currents and d- and q-axis voltage references of the IUT current controller. Since losses of the VSC are not modeled, voltage references and actual voltages at the terminals can be assumed to be identical. In the figure, legends ' i_{dd} ', ' i_{qd} ', ' u_{dd} ' and ' u_{qd} ' are currents and voltages of the IUT when simulated with the PMSM. Similarly, ' i_{de} ', ' i_{qe} ', ' u_{de} ' and ' u_{qe} ' are when simulated with the emulator. A fifth subplot shows amplitude of voltage vector and maximum available phase voltage. ' U_{IUT} ' and ' U_{Emul} ' are amplitudes of the voltage of the IUT and VSC inside the emulator.

The rotor speeds between the two simulations are almost identical as observed in Figure 3-15. The difference in rotor speed between the two simulations is also less than ± 2 rpm like the earlier result. The error in the torques on the other hand is slightly higher when compared to Figure 3-15, around ± 5 Nm. In addition, the ripple in the torque from the emulator setup is higher as well compared to PMSM especially between 1 s to 1.5 s. The higher difference in torque is observed after the amplitude of the voltage in emulator VSC hits the limit. The d- and q-axis currents between the simulations also vary like the torques. The maximum differences between the two d- and q-axis currents are similar as earlier, around ± 4 A. Once

again, the d-axis currents have slightly higher difference than q-axis. However, the d- and q-axis voltages deviate much more than before. The difference between the two d-axis voltages is around -20 V to 5 V and the q-axis voltages around ± 10 V. The difference between the two d-axis voltages is also visible in the figure. This happens because, the emulator VSC reaches the voltage limit as seen in the last subplot. Therefore, it can no longer produce the correct voltage at the terminals as given by (3-15). Since the IUT has a current controller, the currents have a much smaller error like the earlier case presented in Figure 3-15. In addition, same

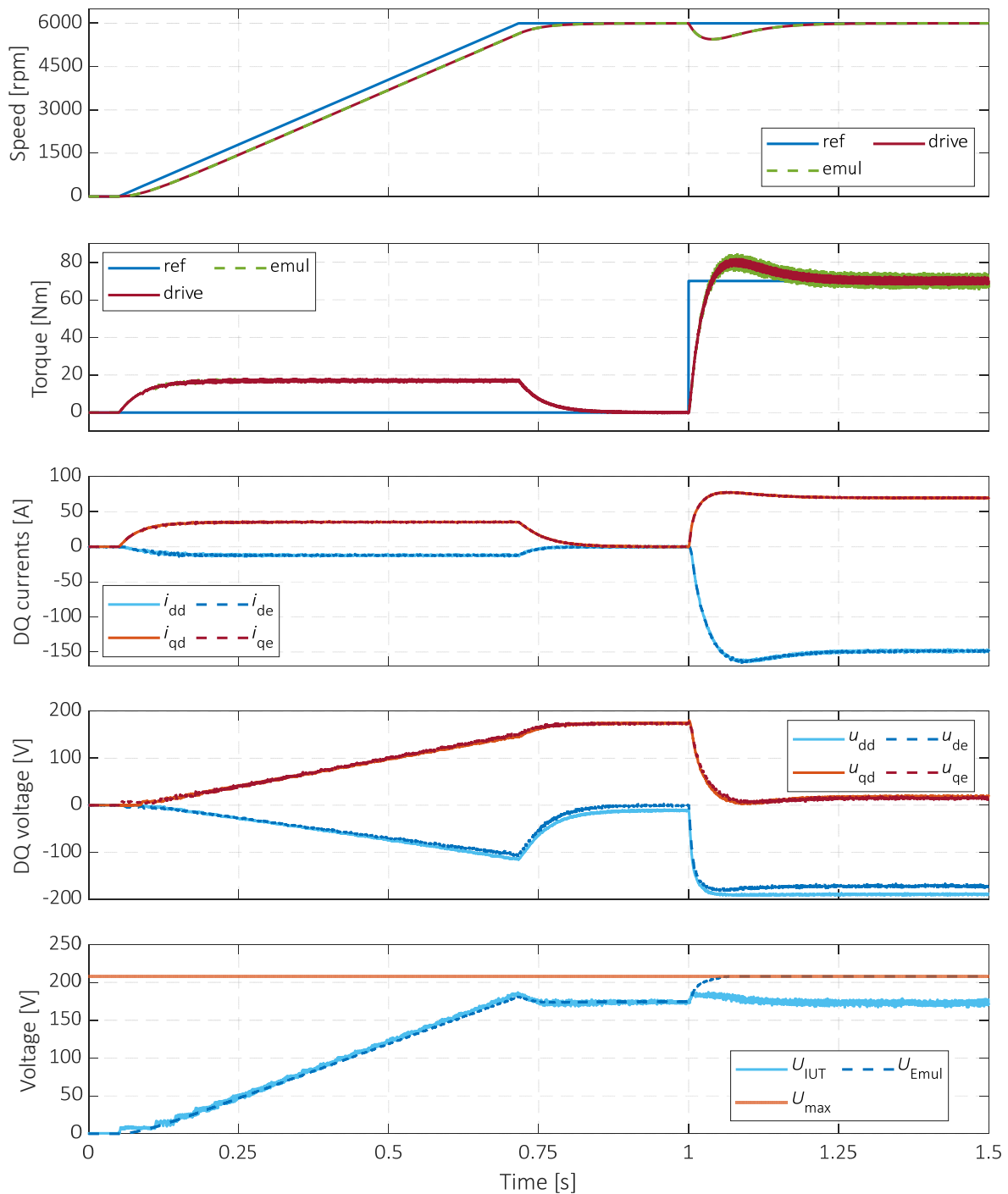


Figure 5-4: Comparison of simulation results when the IUT is simulated with PMSM and emulator. A speed reference of 6000 rpm is applied at 0.05 sec followed by a load torque step of 70 Nm at 1 sec.

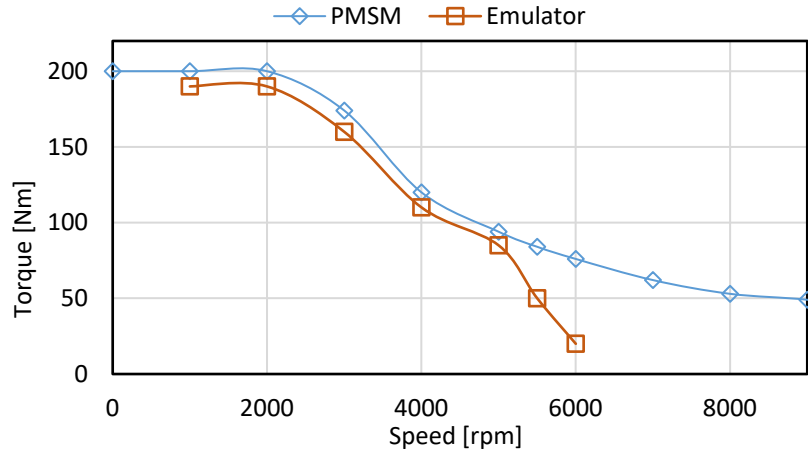


Figure 5-5: Operating boundary of the emulator obtained using simulations and the theoretical boundary of PMSM.

current reference map is used in both simulations i.e., between the simulation of IUT with PMSM and emulator. Therefore, average electromagnetic torque and consequently, rotor speed are almost identical. Figure 5-4 shows that even though same torque and speed operating point is reached when testing the IUT with PMSM and emulator, the IUT does not operate at same operating point in dq-frame. Therefore, this operating point ends up outside the operating boundary of the emulator which is determined by the maximum voltage in this case.

Further simulations are performed, and a torque speed operating boundary of the machine emulator is obtained such that the operating points in dq-frame are same when the IUT is simulated with PMSM and emulator. The emulator boundary and a theoretical PMSM operating boundary are displayed in Figure 5-5. The theoretical PMSM operating boundary is calculated using the iterative method described in [49]. To avoid speed controller oscillations in deep field weakening region, a conservative approach is used when calculating current references. The maximum DC link voltage is limited to 90% and maximum power is limited to 95% of the available peak power, namely to 324 V and 57 kW, respectively. Hence, verification of the emulator boundary is done at a slightly lower torque than the maximum available torque. It can be observed from the figure that the results of the simulations correlate well with the analytical results presented in Figure 5-3.

5.2 High bandwidth machine emulator

The bandwidth of the emulator can be increased by controlling the DC link voltage as mentioned before. However, it would require an additional DC-DC converter which leads to higher cost and complexity. Therefore, another coupling network i.e., a transformer is considered for the emulator. One advantage of using a transformer as coupling network is that it provides galvanic isolation between the IUT and emulator. Additionally, if the transformer windings are connected in star configuration and the neutral points are ungrounded, the zero-sequence component of current will be zero. If the transformer windings are connected in delta configuration, then the zero-sequence current will circulate

between the phases. Therefore, the circulation of common-mode current which is experienced in earlier setup can be avoided by using a transformer.

5.2.1 Model of three-phase transformer

A three leg three-phase transformer with an air gap as shown in Figure 5-6 is considered. Voltage equation of a three-phase transformer can be written as

$$\begin{bmatrix} u_a^1 \\ u_b^1 \\ u_c^1 \end{bmatrix} = \begin{bmatrix} R_a^1 & 0 & 0 \\ 0 & R_b^1 & 0 \\ 0 & 0 & R_c^1 \end{bmatrix} \begin{bmatrix} i_a^1 \\ i_b^1 \\ i_c^1 \end{bmatrix} + \frac{d}{dt} \begin{bmatrix} \psi_a^1 \\ \psi_b^1 \\ \psi_c^1 \end{bmatrix} \quad (5-11)$$

$$\begin{bmatrix} u_x^2 \\ u_y^2 \\ u_z^2 \end{bmatrix} = \begin{bmatrix} R_x^2 & 0 & 0 \\ 0 & R_y^2 & 0 \\ 0 & 0 & R_z^2 \end{bmatrix} \begin{bmatrix} i_x^2 \\ i_y^2 \\ i_z^2 \end{bmatrix} + \frac{d}{dt} \begin{bmatrix} \psi_x^2 \\ \psi_y^2 \\ \psi_z^2 \end{bmatrix}$$

where a, b and c indicates primary side coils, x, y and z indicates secondary side coils and 1, 2 indicates that the quantities are referred to primary and secondary side respectively. The flux linkages in the transformer are composed of self and mutual flux of primary side coil and the mutual flux due to secondary side coils and vice versa.

$$\begin{bmatrix} \psi_a^1 \\ \psi_b^1 \\ \psi_c^1 \end{bmatrix} = L_{abc}^1 \begin{bmatrix} i_a^1 \\ i_b^1 \\ i_c^1 \end{bmatrix} + L_{abczyz} \begin{bmatrix} i_x^2 \\ i_y^2 \\ i_z^2 \end{bmatrix} \quad (5-12)$$

$$\begin{bmatrix} \psi_x^1 \\ \psi_y^1 \\ \psi_z^1 \end{bmatrix} = L_{xyz}^2 \begin{bmatrix} i_x^2 \\ i_y^2 \\ i_z^2 \end{bmatrix} + L_{abczyz} \begin{bmatrix} i_a^1 \\ i_b^1 \\ i_c^1 \end{bmatrix}.$$

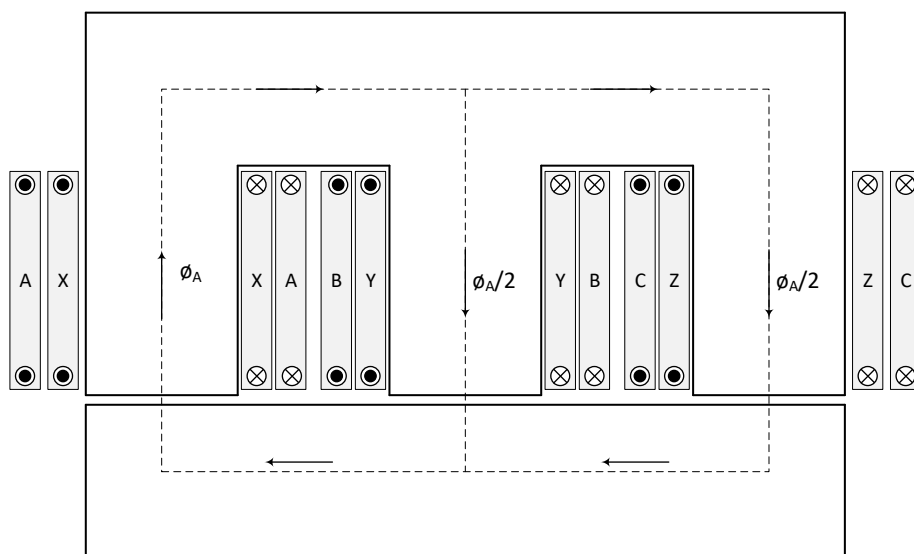


Figure 5-6: Cross-section of a three-phase transformer

The iron-core is operating in the linear region of BH curve, and the cross-sections are assumed as uniform across the transformer core. In addition, the number of turns in the primary and secondary coils are N_1 and N_2 respectively. Furthermore, the leakage in the three-phase coils is assumed to be identical. Then, the inductance matrices in (5-12) can be expressed as

$$\begin{aligned} \mathbf{L}_{abc}^1 &= \begin{bmatrix} L_a & M_{ab} & M_{ac} \\ M_{ba} & L_b & M_{bc} \\ M_{ca} & M_{cb} & L_c \end{bmatrix} = \begin{bmatrix} L_{l1}^1 + L_{m1}^1 & -\frac{1}{2}L_{m1}^1 & -\frac{1}{2}L_{m1}^1 \\ -\frac{1}{2}L_{m1}^1 & L_{l1}^1 + L_{m1}^1 & -\frac{1}{2}L_{m1}^1 \\ -\frac{1}{2}L_{m1}^1 & -\frac{1}{2}L_{m1}^1 & L_{l1}^1 + L_{m1}^1 \end{bmatrix} \\ \mathbf{L}_{xyz}^2 &= \begin{bmatrix} L_x & M_{xy} & M_{xz} \\ M_{yx} & L_y & M_{yz} \\ M_{zx} & M_{zy} & L_z \end{bmatrix} = \begin{bmatrix} L_{l2}^2 + L_{m2}^2 & -\frac{1}{2}L_{m2}^2 & -\frac{1}{2}L_{m2}^2 \\ -\frac{1}{2}L_{m2}^2 & L_{l2}^2 + L_{m2}^2 & -\frac{1}{2}L_{m2}^2 \\ -\frac{1}{2}L_{m2}^2 & -\frac{1}{2}L_{m2}^2 & L_{l2}^2 + L_{m2}^2 \end{bmatrix} \quad (5-13) \\ \mathbf{L}_{abczyz} &= \begin{bmatrix} M_{ax} & M_{ay} & M_{az} \\ M_{bx} & M_{by} & M_{bz} \\ M_{cx} & M_{cy} & M_{cz} \end{bmatrix} = \begin{bmatrix} L_{ps} & -\frac{1}{2}L_{ps} & -\frac{1}{2}L_{ps} \\ -\frac{1}{2}L_{ps} & L_{ps} & -\frac{1}{2}L_{ps} \\ -\frac{1}{2}L_{ps} & -\frac{1}{2}L_{ps} & L_{ps} \end{bmatrix} \end{aligned}$$

where L_{l1}^1 and L_{l2}^2 are primary and secondary side leakage inductances respectively. L_{m1}^1 and L_{m2}^2 is the main inductance of primary and secondary side coils. And L_{ps} is the mutual inductance between primary and secondary coils. The inductances L_{m1}^1 and L_{m2}^2 are proportional to number of turns in the phase coils.

$$\frac{L_{m1}^1}{L_{m2}^2} = \frac{N_1}{N_2} \quad (5-14)$$

The flux linkages can be first transformed to dq-frame using Clark and Park transformations.

$$\begin{aligned} \begin{bmatrix} \psi_{d1}^1 \\ \psi_{q1}^1 \\ \psi_{01}^1 \end{bmatrix} &= L_{dq0,1}^1 \begin{bmatrix} i_{d1}^1 \\ i_{q1}^1 \\ i_{01}^1 \end{bmatrix} + L_{dq0,12} \begin{bmatrix} i_{d2}^2 \\ i_{q2}^2 \\ i_{02}^2 \end{bmatrix} \\ \begin{bmatrix} \psi_{d2}^2 \\ \psi_{q2}^2 \\ \psi_{02}^2 \end{bmatrix} &= L_{dq0,2}^2 \begin{bmatrix} i_{d2}^2 \\ i_{q2}^2 \\ i_{02}^2 \end{bmatrix} + L_{dq0,12} \begin{bmatrix} i_{d1}^1 \\ i_{q1}^1 \\ i_{01}^1 \end{bmatrix} \end{aligned} \quad (5-15)$$

$$\begin{aligned}
L_{dq0,1}^1 &= \begin{bmatrix} L_{l1}^1 + \frac{3}{2}L_{m1}^1 & 0 & 0 \\ 0 & L_{l1}^1 + \frac{3}{2}L_{m1}^1 & 0 \\ 0 & 0 & L_{l1}^1 \end{bmatrix} \\
L_{dq0,2}^2 &= \begin{bmatrix} L_{l2}^2 + \frac{3}{2}L_{m2}^2 & 0 & 0 \\ 0 & L_{l2}^2 + \frac{3}{2}L_{m2}^2 & 0 \\ 0 & 0 & L_{l2}^2 \end{bmatrix} \\
L_{dq0,12} &= \begin{bmatrix} \frac{3}{2}L_{ps} & 0 & 0 \\ 0 & \frac{3}{2}L_{ps} & 0 \\ 0 & 0 & 0 \end{bmatrix}.
\end{aligned}$$

The inductance matrix $L_{dq0,1}^1$ and $L_{dq0,2}^2$ are like that of a three-phase inductor. The inductance matrix $L_{dq0,12}$ only has mutual inductance components. Therefore, there is no zero component. Moreover, if the neutral point in case of star connection is ungrounded, the zero-sequence component can be neglected. It is because the zero sequence of current in such case has no path to flow. If the resistances of primary and secondary side coils are identical to R_a^1 and R_x^2 respectively, then the voltage equations in (5-11) can written in dq-frame as

$$\begin{aligned}
\begin{bmatrix} u_{d1}^1 \\ u_{q1}^1 \\ u_{01}^1 \end{bmatrix} &= \begin{bmatrix} R_a^1 & 0 & 0 \\ 0 & R_a^1 & 0 \\ 0 & 0 & R_a^1 \end{bmatrix} \begin{bmatrix} i_{d1}^1 \\ i_{q1}^1 \\ i_{01}^1 \end{bmatrix} + \begin{bmatrix} 0 & -\omega & 0 \\ \omega & 0 & 0 \\ 0 & 0 & 0 \end{bmatrix} \begin{bmatrix} \psi_{d1}^1 \\ \psi_{q1}^1 \\ \psi_{01}^1 \end{bmatrix} + \frac{d}{dt} \begin{bmatrix} \psi_{d1}^1 \\ \psi_{q1}^1 \\ \psi_{01}^1 \end{bmatrix} \\
\begin{bmatrix} u_{d2}^2 \\ u_{q2}^2 \\ u_{02}^2 \end{bmatrix} &= \begin{bmatrix} R_x^2 & 0 & 0 \\ 0 & R_x^2 & 0 \\ 0 & 0 & R_x^2 \end{bmatrix} \begin{bmatrix} i_{d2}^2 \\ i_{q2}^2 \\ i_{02}^2 \end{bmatrix} + \begin{bmatrix} 0 & -\omega & 0 \\ \omega & 0 & 0 \\ 0 & 0 & 0 \end{bmatrix} \begin{bmatrix} \psi_{d2}^2 \\ \psi_{q2}^2 \\ \psi_{02}^2 \end{bmatrix} + \frac{d}{dt} \begin{bmatrix} \psi_{d2}^2 \\ \psi_{q2}^2 \\ \psi_{02}^2 \end{bmatrix}.
\end{aligned} \tag{5-16}$$

If the magnetizing current and core losses are negligible then the transformer currents on both sides can be related as follows

$$\begin{aligned}
\frac{i_{d1}^1}{i_{d2}^2} &= -\frac{N_2}{N_1} \\
\frac{i_{q1}^1}{i_{q2}^2} &= -\frac{N_2}{N_1}.
\end{aligned} \tag{5-17}$$

It is to be noted that in (5-11), it is assumed that the currents go into the transformer both in the primary and secondary side. Therefore, a negative sign appears in (5-17). To avoid the negative sign further, it is assumed that the current goes out of the transformer on the secondary side. The d- and q-axis equivalent circuit model of the transformer can then be drawn as shown in Figure 5-7.

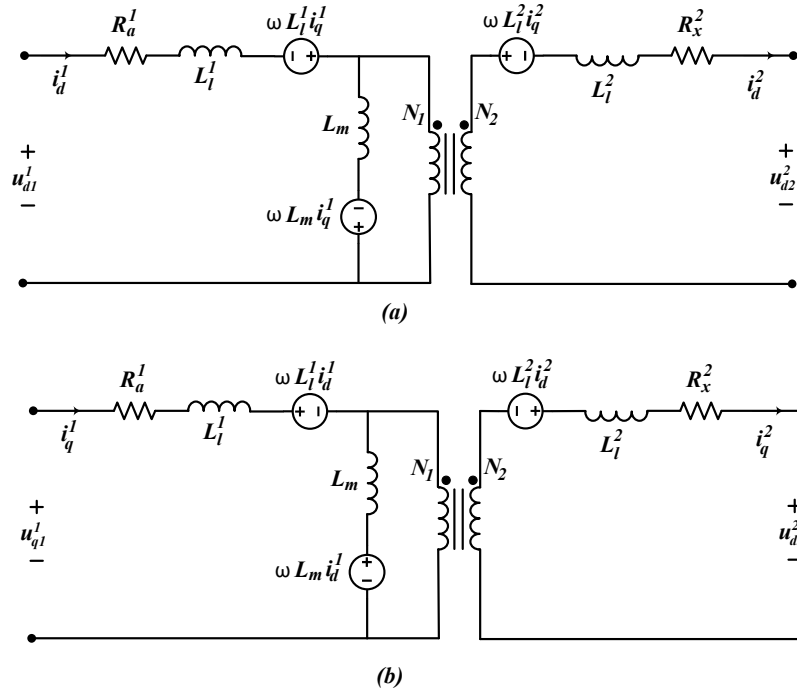


Figure 5-7: D- and q-axis equivalent circuit model of a three-phase transformer. $L_m = L_{m1}^1 + \frac{N_1}{N_2} L_{ps}$

In (5-16), there are two different currents, primary and secondary side. To obtain the model of the transformer with only primary side currents as state variable, the secondary side quantities can be referred to primary side. Using, (5-14) and (5-17), the voltage equation in (5-16) can be expressed as

$$\begin{bmatrix} u_{d1}^1 \\ u_{q1}^1 \\ u_{01}^1 \end{bmatrix} = \mathbf{R}_{mat} \begin{bmatrix} i_{d1}^1 \\ i_{q1}^1 \\ i_{01}^1 \end{bmatrix} + \mathbf{L}_{mat} \begin{bmatrix} i_{d1}^1 \\ i_{q1}^1 \\ i_{01}^1 \end{bmatrix} + \begin{bmatrix} u_{d2}^1 \\ u_{q2}^1 \\ u_{02}^1 \end{bmatrix}$$

$$\mathbf{R}_{mat} = \begin{bmatrix} R_a^1 + R_x^1 & -\omega(L_{l1}^1 + L_{l2}^1) & 0 \\ \omega(L_{l1}^1 + L_{l2}^1) & R_a^1 + R_x^1 & 0 \\ 0 & 0 & R_a^1 + R_x^1 \end{bmatrix} \quad (5-18)$$

$$\mathbf{L}_{mat} = \begin{bmatrix} L_{l1}^1 + L_{l2}^1 & 0 & 0 \\ 0 & L_{l1}^1 + L_{l2}^1 & 0 \\ 0 & 0 & L_{l1}^1 + L_{l2}^1 \end{bmatrix}$$

$$R_x^1 = R_x^2 \left(\frac{N_1}{N_2} \right)^2 \quad L_{l2}^1 = L_{l2}^2 \left(\frac{N_1}{N_2} \right)^2$$

$$\begin{bmatrix} u_{d2}^1 \\ u_{q2}^1 \\ u_{02}^1 \end{bmatrix} = \frac{N_1}{N_2} \begin{bmatrix} u_{d2}^2 \\ u_{q2}^2 \\ u_{02}^2 \end{bmatrix}$$

where all the quantities are referred to primary side. It can be observed from (5-18) that the transformer will have the lowest voltage drop when compared to three-phase or single-phase inductors. The reason is that the voltage drop across the transformer consists mainly of the leakage inductances and resistance.

5.2.2 Design of the three-phase transformer

The design requirements of the transformer are presented in

Table 5-1. The transformer is designed for a higher voltage (800V) and higher power (250 kW) application compared to the PMSM discussed earlier because this will allow the verification of the rated capacity of the VSC shown in Figure 4-4. The maximum fundamental frequency of 800 Hz is considered for design to enable emulation of electric machines with higher rotating speed than the PMSM considered earlier. The maximum The RMS current density is higher than the single-phase inductors used earlier implying that forced cooling should be

Table 5-1: Design requirements of the three-phase transformer

Parameter	Value	Unit
Turns ratio	1:1	
Maximum fundamental frequency of current	800	Hz
Maximum power	250	kW
Maximum RMS current (for 30 s)	340	A
Maximum RMS current density (for 30 s)	20	A/mm ²
Induced line voltage @ 200 Hz	800	V

considered. The turns ratio is defined as 1:1 because a different turns ratio would limit the usage of the PHIL test bench studied in this work. For example, a lower number of turns on the secondary side might improve the bandwidth by providing a step up in the voltage limit of the VSC. However, to deliver the same power, the current rating of the VSC needs to be higher than the IUT.

The main design steps followed in the design are as follows. First, a preliminary design using analytical method is performed. Then a FEM model is created in Ansys Maxwell. Using the FEM model, inductance matrix is calculated at no-load. Then, using inductance matrix at no-load (5-11) is solved to calculate the primary and secondary currents at load. The calculated currents are used in FEM to recalculate the inductance matrix. The difference between the two-inductance matrices is used to find convergence. Afterwards, the design was optimized to reduce 3rd, 5th, 7th, and 11th harmonics in line-to-line induced voltage and improve power factor and efficiency.

The flux density distribution of the transformer at maximum power is shown in Figure 5-8 for two different time instances of the fundamental period. As can be seen, the same shape of the core is used like the single-phase transformer. Because of the air gap, some fluxes fringe and complete their path through the surrounding area and back to the core so that the normal components of the fluxes are created, which are perpendicular to the core surfaces [58]. Therefore, in the design, the “I” part of the core is slightly wider than the “E” part to reduce fringing of flux close to the edges of the “I” part. The material of the core is SURA M235-35A which was used earlier for the inductors. It can be seen from the figure that the maximum flux density in the transformer is well below the saturation flux density of the material. The flux density is reduced to minimize the total core loss.

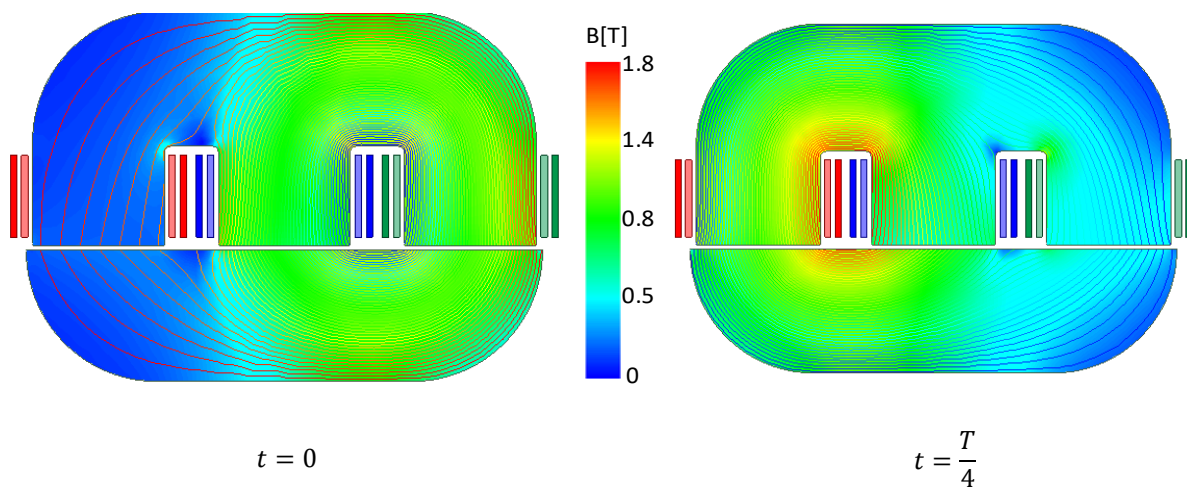


Figure 5-8: Flux density distribution and flux lines calculated from FEM of the transformer at load. For phase a and phase x, $i_a^1 = 370\cos(400\pi t)$; $i_x^1 = 370\cos(400\pi t - 3.412)$.

Table 5-2: Finalized design of the three-phase transformer

Parameter	Value	Unit
Width	410	mm
Height	260	mm
Stack length	150	mm
Minimum air gap	2.6	mm
Maximum air gap	2.7	mm
Number of turns per phase	22	
Primary phase resistance	18.6	mΩ
Secondary phase resistance	17.1	mΩ
Maximum Cu loss	6.19	kW
Iron core loss @ 200 Hz	0.84	kW
Iron core loss @ 800 Hz	5.96	kW
Mass of active material	131	kg

The parameters of the final design are presented in Table 5-2. Two different airgaps are defined in the table. The airgap in the middle section of the core is slightly higher to have more uniform distribution of flux in the three legs. The phase resistance of the primary and secondary are calculated analytically. The secondary winding occupies the inner layer whereas the primary is on the outer layer. Hence, the secondary end winding will be shorter. Therefore, the phase resistance of the secondary winding is slightly smaller than the primary. The copper losses of the transformer at full load are approximately 2% of the maximum power. The efficiency of the transformer at full load and 200 Hz operating frequency is around 97%. In comparison, the single-phase inductors had a much lower efficiency of 94.6% at full load and 200 Hz operating frequency. The efficiency of the transformer is around 95% at full load and maximum operating frequency of 800 Hz.

5.3 Verification of high bandwidth emulator

A simulation setup like the one presented in Chapter 3 is used to verify the high bandwidth machine emulator. The machine emulator is compared to simulation of the PMSM drive. Although, the transformer is designed for 250kW, the same 60 kW PMSM described in Chapter 3 is used. The reason is that the bandwidth of the emulator is related to operating frequency which can be evaluated even with the lower power machine model. PHIL test bench as shown in Figure 3-7 is modeled with a transformer as coupling network.

5.3.1 Steady state performance

Simulation results of IUT when simulated with a machine emulator are compared to simulation of IUT with PMSM in Figure 5-9. The results shown in the figure corresponds to peak power operation of the machine with steady-state rotor speed of 3000 rpm and load torque of 160 Nm. Lower cases are used for variables when denoting instantaneous quantities while upper case for fundamental or average. Four subplots are shown in the figure: phase current, line voltage, active and reactive power supplied by IUT. The powers are calculated using instantaneous three-phase voltage and currents. The line voltage shown in figure is derived from phase voltage measurement.

In Figure 5-9, steady-state phase currents have small differences. The amplitude of fundamental component of the phase current when simulated with emulator is 0.25 % higher. However, in comparison to Figure 3-11, the phase current of the emulator looks more sinusoidal because there is no common-mode current in the setup. The line voltage between the two simulations also has very small difference. The amplitude of the fundamental component of voltage when tested with the drive is higher by 1 %. Similarly, the average active powers between the two simulations differ by 1 %. However, there is a slightly bigger difference in the reactive power. Since the reactive power consumption of the magnetizing inductance is not considered in the emulator's control, the reactive power of the IUT in the case of a machine emulator is 5 % higher compared to the simulation with PMSM. The reason is that Therefore, a higher reactive power is observed in case of machine emulator. Overall, the differences are still quite small and can be acceptable.

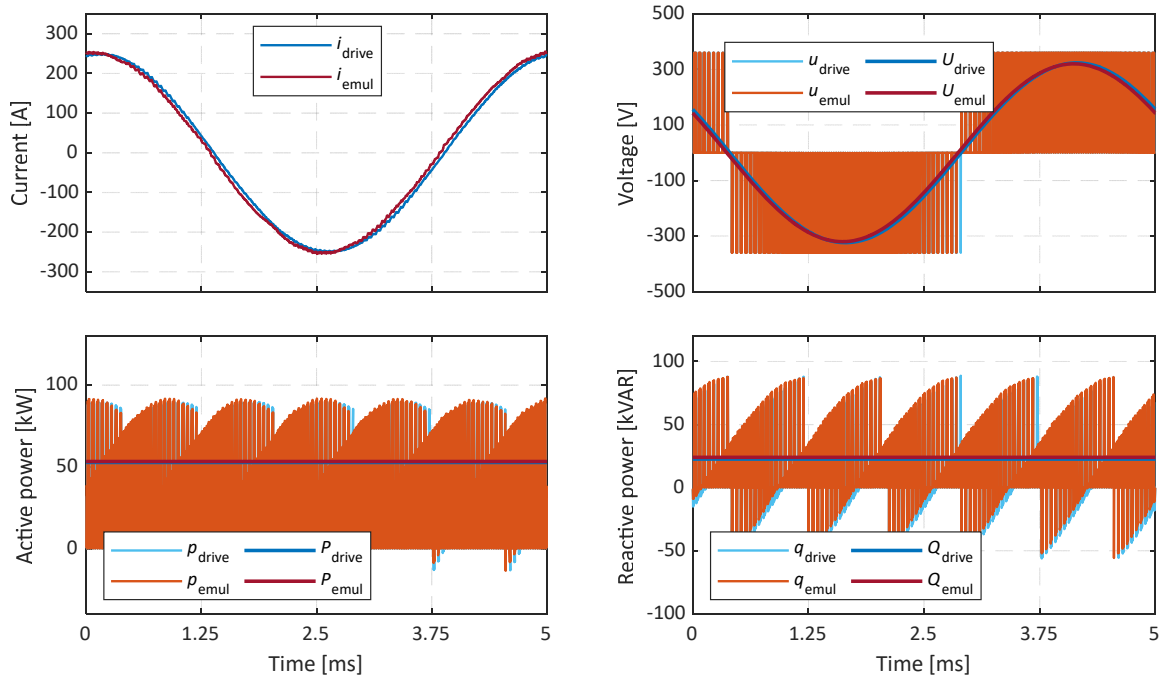


Figure 5-9: Comparison of steady state simulation results of IUT when simulated with PMSM and emulator for an operating point at 3000 rpm and 160 Nm.

5.3.2 Dynamic performance

A dynamic simulation with the same test case as shown earlier in Figure 5-4 is performed for the high bandwidth emulator. The result of the dynamic simulations is shown in Figure 5-10. The figures are organized in the same way presented earlier in Figure 5-4. In the figure, first subplot from top presents a comparison of rotor speed. The speed reference is indicated by 'ref', rotor speed of the PMSM by 'drive' and estimated rotor speed of the emulator by 'emul'. Second subplot from the top presents electromagnetic torque and load torque. The legend marked 'load' represents load torque reference while 'drive' and 'emul' indicate electromagnetic torque of the PMSM and calculated torque in the emulator, respectively. Third and fourth subplot show d- and q-axis currents and d- and q-axis voltage references of the IUT current controller. In the figure, legends ' i_{dd} ', ' i_{qd} ', ' u_{dd} ' and ' u_{qd} ' are currents and voltages of the IUT when simulated with the PMSM. Similarly, ' i_{de} ', ' i_{qe} ', ' u_{de} ' and ' u_{qe} ' are when simulated with the emulator. A fifth subplot shows amplitude of voltage vector and maximum available phase voltage. ' U_{IUT} ' and ' U_{Emul} ' are amplitudes of the voltage of the IUT and VSC inside the emulator.

The rotor speeds between the two simulations look almost identical. The difference in rotor speed between the two simulations is also less than ± 1 rpm during steady state. On the other hand, the error in the torques is slightly higher, around ± 5 Nm around 1.25 s to 1.5 s. It can be observed from the figure that the ripple in the torque from the emulator case is higher compared to PMSM in the same time interval. The d- and q-axis currents have a small error as well. The maximum differences between the two d- and q-axis currents are similar as

earlier, around ± 3 A. The d-axis currents have slightly higher difference than q-axis in the time interval of 1.25 s to 1.5 s. There is similar difference in d- and q-axis voltages between the two simulations as well. During steady state, the maximum difference in d- and q-axis voltages between the two simulations is around ± 10 V. The voltage amplitude of both the IUT and the emulator VSC are below the maximum voltage limit.

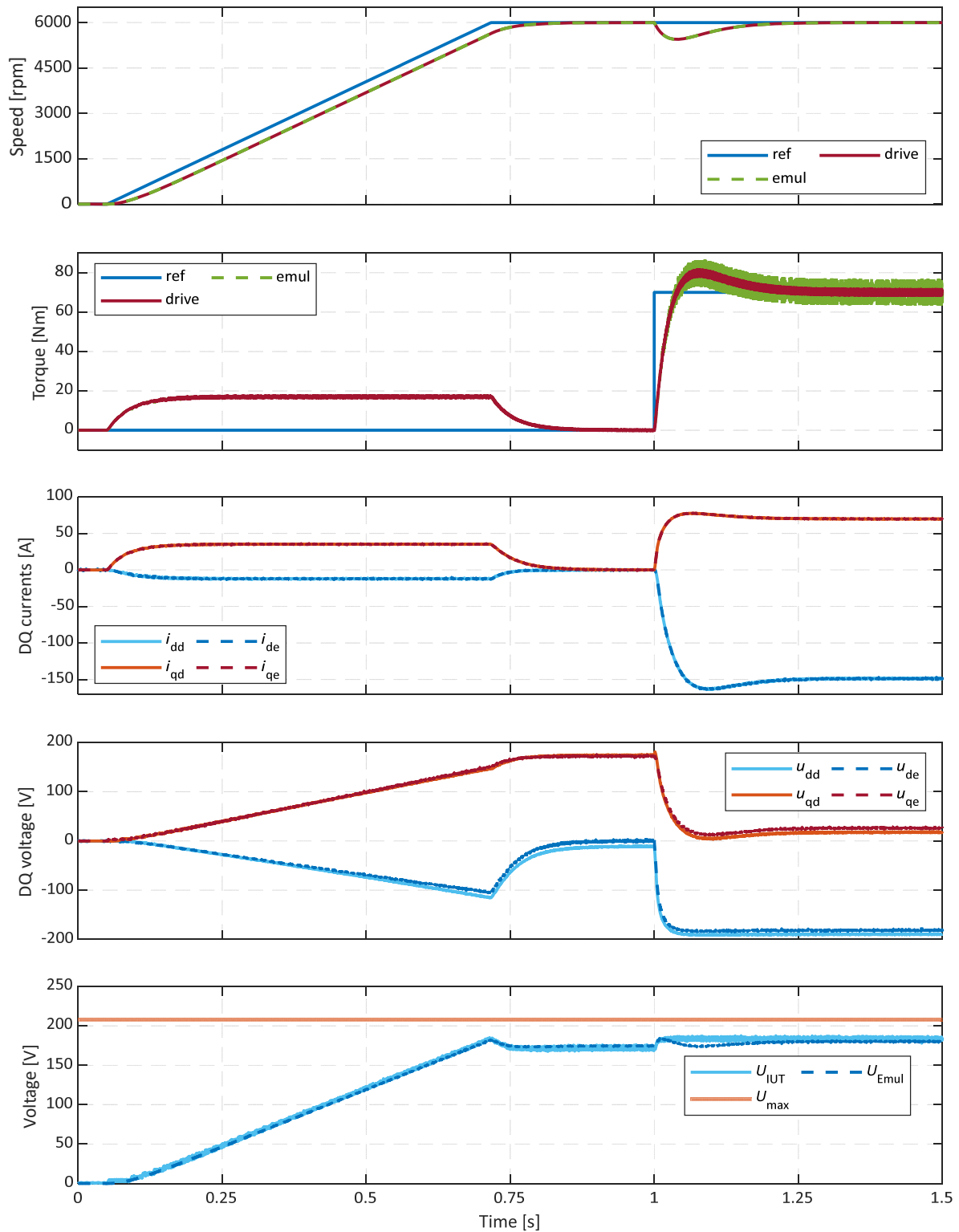


Figure 5-10: Comparison of simulation results when the IUT is simulated with PMSM and emulator. A speed reference of 6000 rpm is applied at 0.05 sec followed by a load torque step of 70 Nm at 1.2 sec.

Comparing the results shown in Figure 5-4 and Figure 5-10, it can be observed that the rotor speed and the torque are very similar for the emulator. The emulated rotor speed and the simulated rotor speed of PMSM have small differences in both the figures. In addition, similar torque ripples are observed in the two figures. The d- and q-axis currents also have very small differences in both figures when compared to PMSM. However, key differences are observed the case of d- and q-axis voltages and the amplitude of the emulator VSC. Although, there are small differences d- and q-axis voltages of the emulator case when compared to PMSM in Figure 5-10, they are smaller in comparison to the observations made in Figure 5-4. In addition, the voltage limit is not reached in the emulator VSC in Figure 5-10. Therefore, the high bandwidth emulator can reach the same operating point as the PMSM in the dq-frame.

Further simulations are performed, and a torque speed operating boundary of the high bandwidth machine emulator is obtained such that the operating points in dq-frame are same when the IUT is simulated with PMSM and emulator. The emulator operating boundaries when using transformer or single-phase inductors as coupling network are shown along with the theoretical operating boundary of the reference PMSM in Figure 5-5. To avoid speed controller oscillations in deep field weakening region, a conservative approach is used also here when calculating current references. The maximum DC link voltage is limited to 90% and maximum power is limited to 95% of the available peak power, namely to 324 V and 57 kW, respectively. Hence, verification of the emulator boundary is done at a slightly lower torque than that is given by the theoretical boundary of reference PMSM. It can be observed from the figure that the emulator using transformer as coupling network can cover the entire operating region of the reference PMSM. This is an improvement compared to the single-phase inductor case presented earlier.

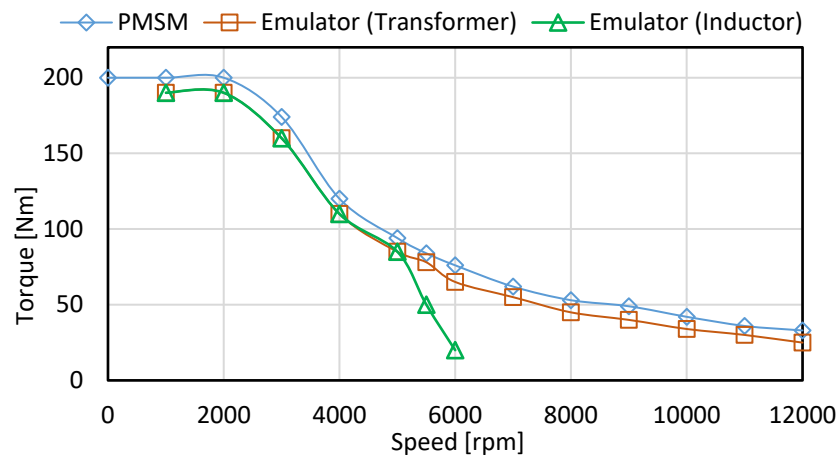


Figure 5-11: Operating boundaries of the emulator with transformer and single-phase inductors as coupling network obtained using simulations and the theoretical boundary of reference PMSM.

Chapter 6

MHIL Testing of Multi-Motor Drive System

Design and experimental evaluation of an MHIL test bench for laboratory verification of multi-motor drive systems are presented. The MHIL bench consists of a real-time simulator interfaced with a dyno test bench. First, the real-time models and the dyno test bench are introduced. It is followed by two methods, open-loop and closed, which are proposed and investigated to interface the dyno test bench and the real-time simulations. Furthermore, the interfacing methods are evaluated in experiments. Finally, an anti-slip function is verified experimentally using the MHIL test bench.

6.1 Mechanical-hardware-in-the-loop test bench

A brief description of the MHIL test bench except the interfacing strategy, which are discussed in the following section is presented in this section. A vehicle with independently drive front wheel is model using CarMaker [59] [60], which also provides a virtual testing platform to design driving cycles. The transmission in an electric drivetrain is included as part of the vehicle model. The models of remaining component i.e., electric machine and inverter together with the DC supply model are referred as electric drive model. A DC supply is modeled instead of a battery as it is not the focus off this work. The electric drive models are implemented using XSG Electric Component Models from dSPACE [61]. The dyno test bench consisting of two identical permanent magnet synchronous machines (PMSMs) is also discussed.

6.1.1 Vehicle Model

A D class BEV is selected as the reference vehicle for modeling, whose main parameters are listed in Table 6-1. The vehicle model is implemented using CarMaker which can be integrated into the MATLAB/Simulink environment. The vehicle model includes vehicle dynamics model, drive model and road model. All these models have parameters that can be set buy the user to adapt the model to a specific vehicle. A detailed description of the vehicle dynamics and the driver model can be found in [33], [59] [60]. A brief description of the different models is presented here.

The vehicle dynamics model is constructed by dividing the vehicle into five rigid bodies: four wheels and a chassis. For each of these five bodies, the motion is described using both algebraic and differential equations. The vehicle dynamics model calculates vehicle states in three dimensions i.e., longitudinal, lateral, and vertical using position-dependent and time-dependent inputs. The position-dependent inputs are provided by the road model. The road

Table 6-1: Parameters of the vehicle used in modeling

Parameter	Value	Unit
Unladen mass	1745	kg
Wheel Inertia	2.673	kg/m ²
Wheel radius	0.343	m
Aero-dynamic drag co-efficient	0.3	
Rolling resistance co-efficient	0.009	
Number of drive units	2	
Gear ratio	7	
Acceleration due to gravity	9.8	m/s ²
Air density	1.18	kg/m ³

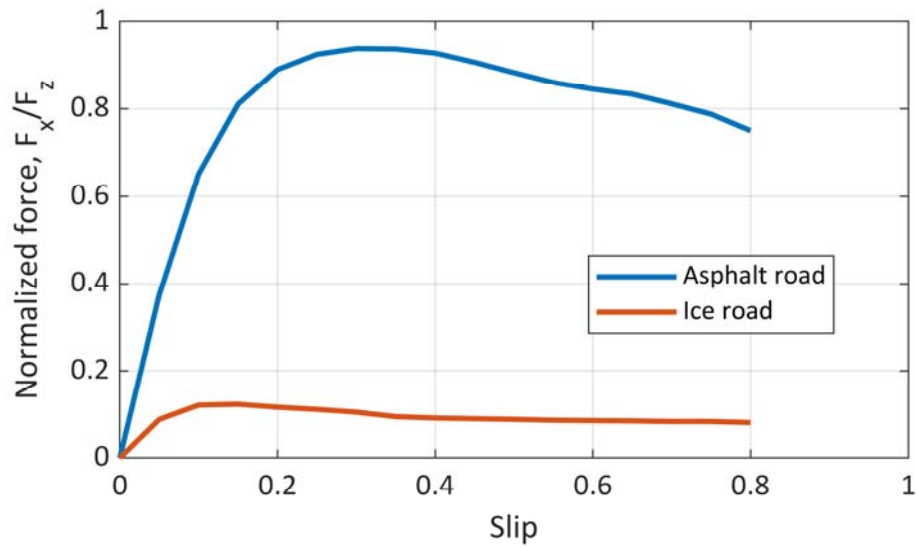


Figure 6-1: Ratio of traction force to vertical force applied on a driven wheel as a function of road friction co-efficient and wheel slip.

model describes the road conditions e.g., friction co-efficient, gradient along the driving trajectory. The time-dependent inputs are obtained from the driver model and transmission.

The drive model controls the longitudinal and lateral motion of the vehicle based on the driving mission. Different driver behaviors and driving missions can be described in the driver model for different cases. The driver model provides the brake pedal position which is used to calculate the brake torque on each wheel.

The input from transmission includes the traction torque, T_t which is used along with wheel torque, T_l and brake torque, T_b to determine the wheel acceleration as follows

$$J \cdot \frac{d\Omega}{dt} = T_t - T_l - T_b \quad (6-1)$$

where J represents the equivalent rotating inertia of the rigid mass including wheel, transmission, drive shaft and electric machine rotor. The wheel torque, T_l depends on the wheel vertical force, wheel slip, and road condition.

The normalized maximum tractive force on the wheel as a function of wheel slip is shown in Figure 6-1. It can be seen from the figure that maximum tractive force reduces with wheel slip. Furthermore, the reduction in the tractive force due to friction co-efficiency of the road is significant. The linear velocity of the vehicle is estimated considering the traction force and resistive force. Considering, only the longitudinal motion of the vehicle, the resistive force can be estimated using (2-1). The slip ratio is estimated using the linear velocity of the vehicle and the wheel.

6.1.2 Electric Drive Model

The 60 kW PMSM for which the parameters are presented in Table 3-1 is considered for modeling. As mentioned before, the electromagnetic model of the machine is implemented in using XSG Electric Component Models from dSPACE. There are some differences in the implemented model. Instead of look-up-tables of d- and q-axis flux linkages and inductance, the model is implemented using only look-up-tables of inductances because the library block used for modeling of the machine only allows input of inductance look-up-tables. The flux linkages can be calculated from the interpolated inductances as

$$\psi_d = L_{da} i_d + \psi_m \quad (6-1)$$

$$\psi_q = L_{qa} i_q$$

where L_{da} and L_{qa} are apparent inductance. The apparent inductances in dq-frame are described as follows [62]:

$$L_{da} = \frac{\psi_d^{(i_d, i_q)} - \psi_d^{(i_d=0, i_q)}}{i_d}; \quad L_{qa} = \frac{\psi_q^{(i_d, i_q)} - \psi_q^{(i_d, i_q=0)}}{i_q} \quad (6-2)$$

When the iron-core of the machine operates in the linear region, the incremental and apparent inductances are the same. Otherwise, the incremental inductance is lower than the apparent inductance as the iron-core starts to saturate. In the implemented model, the apparent and the incremental inductance are assumed to be the same. Furthermore, only look-up-tables of apparent inductances are used in modeling. The apparent inductances used in the modeling of the PMSM are presented in Figure 6-2. The electromagnetic torque of the machine can be calculated using the currents and the inductances as follows

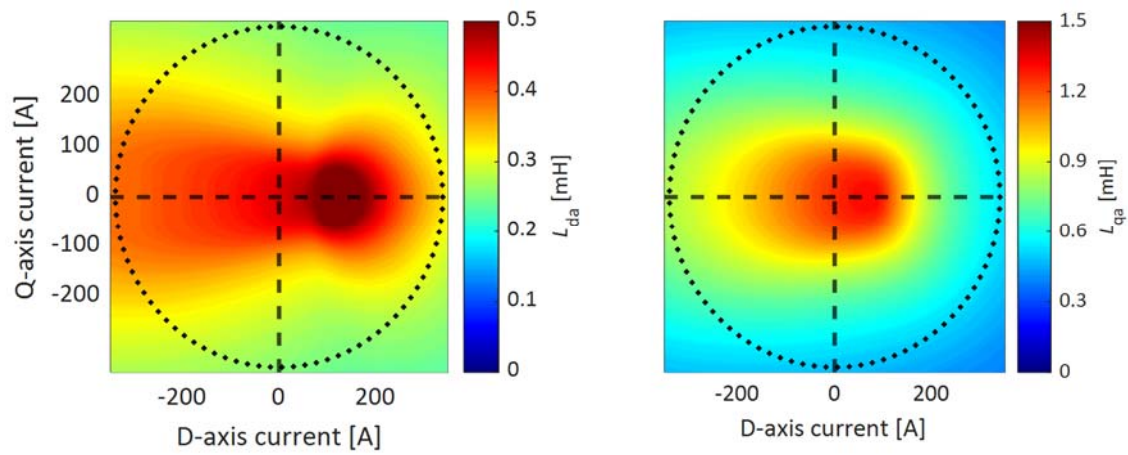


Figure 6-2: Apparent inductance L_{da} and L_{qa} of the modeled PMSM

$$T_e = \frac{3}{2} \cdot p \cdot (\Psi_m \cdot i_q + (L_{da} - L_{qa}) \cdot i_d \cdot i_q) \quad (6-3)$$

where T_e is electromagnetic torque and p is number of pole pairs.

A 2-level VSC is modeled as the inverter. The semiconductor switches are modeled as ideal switches ignoring both losses and switching transients. The inverter model generates the PWM voltages based on the gate signal from the machine control. It also calculates the current drawn from the DC source based on the three-phase current input. The machine control is implemented as described in the previous chapters.

6.1.3 Dynamometer test bench

The dynamometer test bench is very similar to the one shown in Figure 4-10. However, in this case both the PMSMs are driven by identical 2-level VSC using HybridPACK™ 1 module FS400R07A3E3 from Infineon [63]. One of the PMSM acts as traction machine while the other as load machine/dyno which emulates the behavior of one driven wheel. Like before, the controls for both the machines are implemented in the same real-time processor, DS1006 from dSPACE. The controller bandwidths are listed in Table 6-2. Since, IGBTs are used to drive the machines, the bandwidth of the current controller is slightly lower than before. As can be seen from the table, the DC-link voltage is limited to 150V. The reason is that there were some EMI issues in the bench.

Table 6-2: Parameters of the electric machine test bench		
Parameter	Value	Unit
DC-link voltage	150	V
Switching frequency	5	kHz
Speed controller bandwidth	20	rad/s
Current controller bandwidth	400	rad/s
Total inertia	0.051	kg/m ²

The references for control of the two machines depend on the interfacing strategies which are discussed in the following section. When using speed controller, a cascaded control structure is used with FOC of current in inner loop and speed controller in the outer loop. The current controller implemented in the dyno bench is identical to that in real-time simulation. The speed controller is implemented without active damping as it is observed to cause large overshoots in the speed during tests. To improve the dynamic performance of the speed controller, a feed-forward of reference torque of the traction machine is used. The controller gains are decided in a similar way before.

6.2 Interface between real-time simulations and the dyno test bench

The real-time simulator needs to be interfaced with the dyno test bench to create the MHIL test bench. The interface choice can affect the performance and suitability of the HIL method for verification. It is not discussed in detail in the reviewed literature as mentioned earlier. Therefore, various interfacing strategies are discussed and analyzed in this section. They are categorized as open-loop and closed-loop. The interfaces are discussed considering the reference vehicle with two-independently driven front wheels. Nonetheless, they can be applied to systems with other drivetrain architecture.

6.2.1 Open-loop Interface

In an open-loop interface, the real-time model provides the references for control of the machines in the dyno bench. However, there is no feedback from the bench that affects the real-time simulation. In the simulation, only one electric drive can be modeled when considering only longitudinal motion. The dyno test bench in an open-loop interface acts as an observer for the real-time simulations. The interface can be implemented using two different methods which are discussed below.

Open-loop interface method I (OLM I): In the first method rotor speed of electric machine calculated in real-time simulation is used as speed reference for control of the load machine and reference torque from the driver model is used to control the traction machine. The signal interface is shown in Figure 6-4 using solid arrows. A similar approach is followed in [34] with

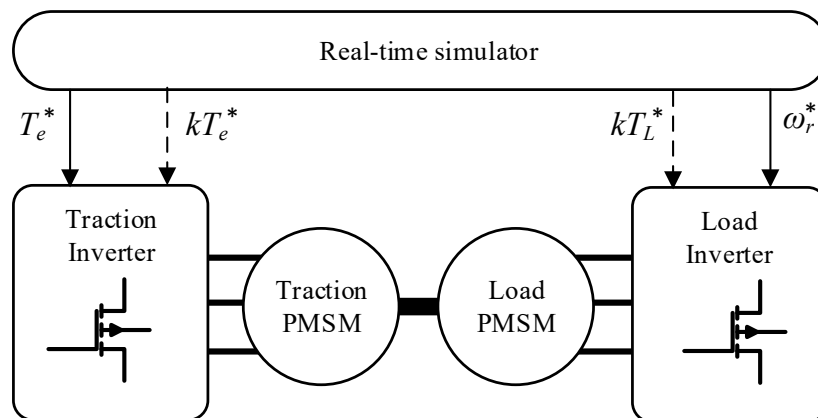


Figure 6-3: Two different methods of controlling the test bench when using open-loop interface between real-time simulator and machine test bench.

a difference that the speed and torque reference are pre calculated using vehicle simulation software.

Open-loop interface method II (OLM II): In the second method, a summation of load and brake torque on the wheel is used as reference to control the load machine and like OLM I, reference torque from the driver model is used to control the traction machine. The signal interface is indicated using dotted arrows in Figure 6-4. Since the rotating inertia in the test bench is different from the simulated mechanical system, the torque references need to be scaled such that the rotor acceleration is similar between the simulation and the bench.

The dyno bench used in this work has very small rotating inertia when compared to the simulated mechanical system e.g., wheels. Therefore, there might be large overshoots in rotor speed when both the machines are controlled using torque references. To prevent these overshoots, a large flywheel may need to be connected in the dyno bench. In addition, the scaling of the torque reference may limit verification at rated power of the drivetrain components. For these reasons, this interface is not evaluated in experiments further.

6.2.2 Closed-loop Interface

In a closed-loop interface, the real-time model provides the references for control of the machines in the dyno bench and measurements from the dyno bench are used as feedback to the real-time simulation. Therefore, this interface creates a bi-directional interaction between the real-time model and the dyno test bench. The real-time model can be scaled down by considering only one electric drive model irrespective of the vehicle motion e.g., longitudinal or lateral being considered. Like the open-loop interface, the closed-loop interface can be implemented using two different methods as well.

Closed-loop interface method I (CLM I): In the first method, the references for control of the two machines in the dyno bench are same as in OLM II. Then, the rotor speed measured in the dyno bench provides feedback to the real-time simulation. The signal interface is shown in Figure 6-4 using dotted arrows. However, the feedback of the speed can present challenges.

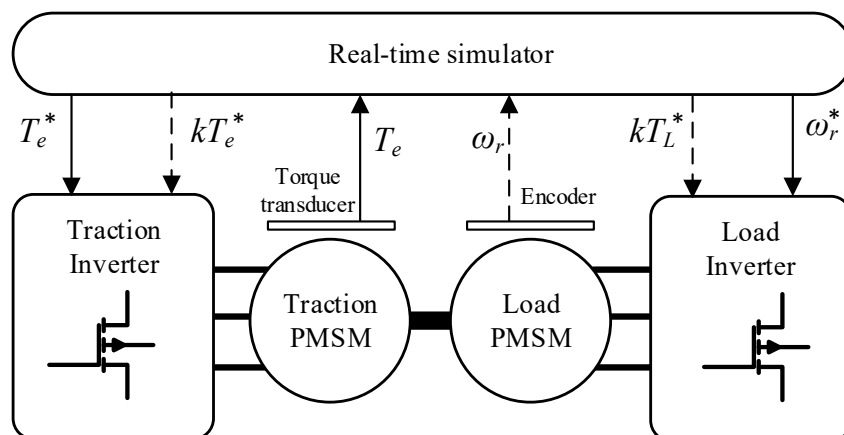


Figure 6-4: Two different methods of controlling the test bench when using closed-loop interface between real-time simulator and machine test bench.

The rotor speed feedback may result into inadvertent detection of vehicle slip in the real-time simulation because of the difference in speed of non-driven and driven wheels. It could be caused by the difference in parameters between the model and the dyno which is often difficult to eliminate. As mentioned earlier, the load torque on the wheels depends on the slip. Therefore, the rotor speed feedback can result in sustained oscillations in the dyno bench. The speed feedback can only be used when utilizing simplified vehicle model i.e., without slip calculation and multi body vehicle dynamics as done in [35] and [36]. Therefore, considering the high-fidelity vehicle model used in this work, this interface method is not used in experiments.

Closed-loop interface method II (CLM II): In the second method, the measured torque from the dyno bench is used as feedback to the real-time simulation. The signal interface is shown in Figure 6-4 using solid arrows. In this method, the torque reference from the driver model is used to control the traction machine. The feedback torque from the dyno bench is used to calculate the rotor speed in real-time simulation. Then, the calculated rotor-speed is used as speed reference for control of the load machine. This method avoids the speed oscillations. In addition, the measurement noise in the feedback will get filtered out by the mechanical model which acts as a low-pass filter. Therefore, the feedback is less prone to EMI issues. A similar approach is also used [33].

6.3 Experimental results

The MHIL test bench used for experimental verification is shown in Figure 6-5. The real-time model of the vehicle and electric drive are implemented using SCALEXIO LabBox from dSPACE. The real-time model of the vehicle is implemented using a CPU board whereas the real-time model of the electric drive is implemented using FPGA board. “PMSM 1” in the figure represents the traction machine whereas “PMSM 2” represents the load machine. The open-

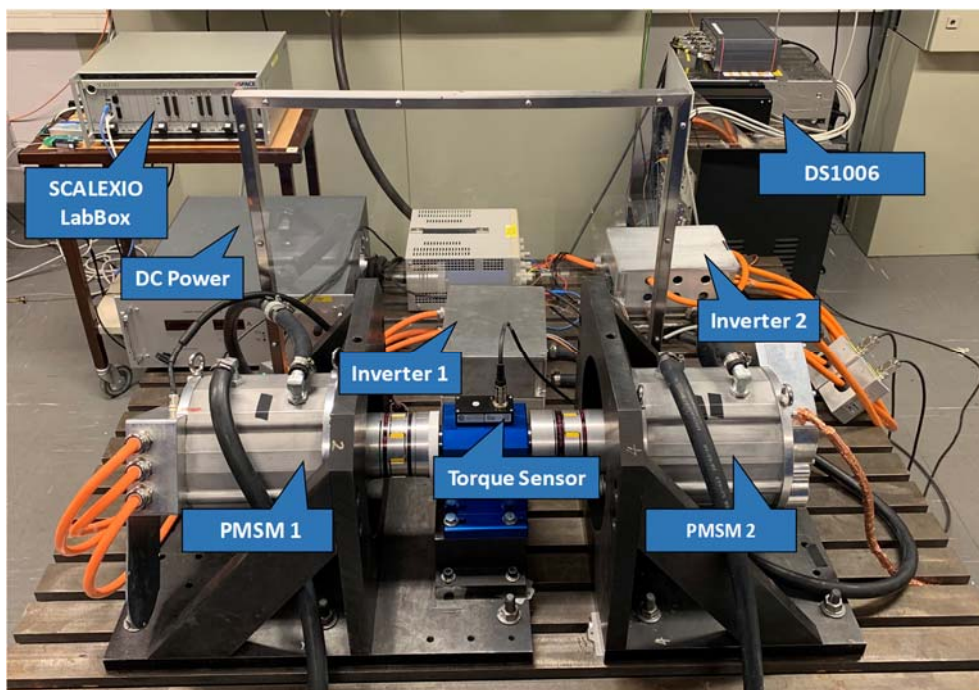


Figure 6-5: Experimental setup with machine test bench connected to real-time simulator

loop interface OLM I and closed-loop interfaces CLM II are verified experimental. In addition, the OLM I interface is also used for verification of an anti-slip control method in experiments

6.3.1 OLM 1 Interface Experimental Results

As mentioned before a vehicle with two independent driven front wheels is modeled in the real-time simulator. In addition, both front left (FL) and front right (FR) electric drivetrains models are implemented. Since, the longitudinal motion of the vehicle is studied, the results are identical for both. The traction machine in the dyno test bench emulates the FR drivetrain and the load machine emulates the FR wheel. A speed-based drive cycle is used, and the results from the experiments are presented in Figure 6-6. Five subplots are shown in the figure. The first subplot shows the vehicle speed obtained from the real-time simulation. The second subplot shows the electric machine torque. The shaft torque measured by means of a torque transducer in the dyno test is shown together with the torque obtained from the real time model. Similarly, rotor speeds and d- and q-axis currents from the dyno test bench and the real-time simulations are shown in third, fourth and fifth plots respectively.

It can be observed from the first subplot that the vehicle speed follows the drive cycle quite well. The vehicle is first accelerated from stand-still to 8 km/h followed by cruising. Then it is accelerated again to 12 km/h followed similarly by cruising. Finally, it is brought to a complete stop. The vehicle is driven on asphalt with a friction coefficient of 0.9 for the entire duration of 50 sec. The small overshoots at the end of acceleration are caused by the driver model.

In the beginning of the drive cycle, the torque measured in the bench is zero for the first few seconds. It is due to the limitation of speed control implemented in the load machine, which does not allow a low-speed ramp-up when torque is applied on the shaft. In [34], the authors added a 50-rpm offset to the speed reference to avoid a similar issue. In this work, a reduction of the reference torque is applied during the initial stage of acceleration. Therefore, the measured torque and d- and q-axis currents are zero during the start of the drive cycle.

Since mechanical losses of the machine are not modeled, the torque measured in the dyno bench is lower than in the simulation as can be seen in the second subplot. On the other hand, the d- and q-axis currents between measurement and simulations are almost identical. The reason is that identical current reference look-up tables and torque reference are used for control of machine in both cases. The rotor speed in measurement has a small delay caused by the bandwidth of the speed controller used in the test bench. At around 3 secs, it can be observed that the measured speed drops. At this point, the reference torque is enabled to the test traction machine as can be observed by the increase in the measured torque. The speed controller is implemented without acting damping. Therefore, it is influenced by a sudden change in the reference torque of the traction machine. Such deviations in the measured speed are also observed during the start of acceleration and deceleration as well as there are sudden changes of torque.

6.3.2 CLM 1 Interface Experimental Results

In this case, the FL electric drivetrains model is implemented in real-time simulator while the FR electric drivetrain and wheel are emulated using the dyno test bench. As observed in Figure 6-6, there was a difference between the shaft torque in the dyno test bench and real-time

simulation. Such difference will lead to unintended lateral motion of the vehicle when using CLM II. Therefore, a look-up table between the shaft torque and q-axis current is generated using steady-state measurements performed on the dyno test bench. Then, this look-up table is used to generate the q-axis current reference to control the traction machine in both the dyno test bench and the real-time simulation while the d-axis current reference is kept at zero.

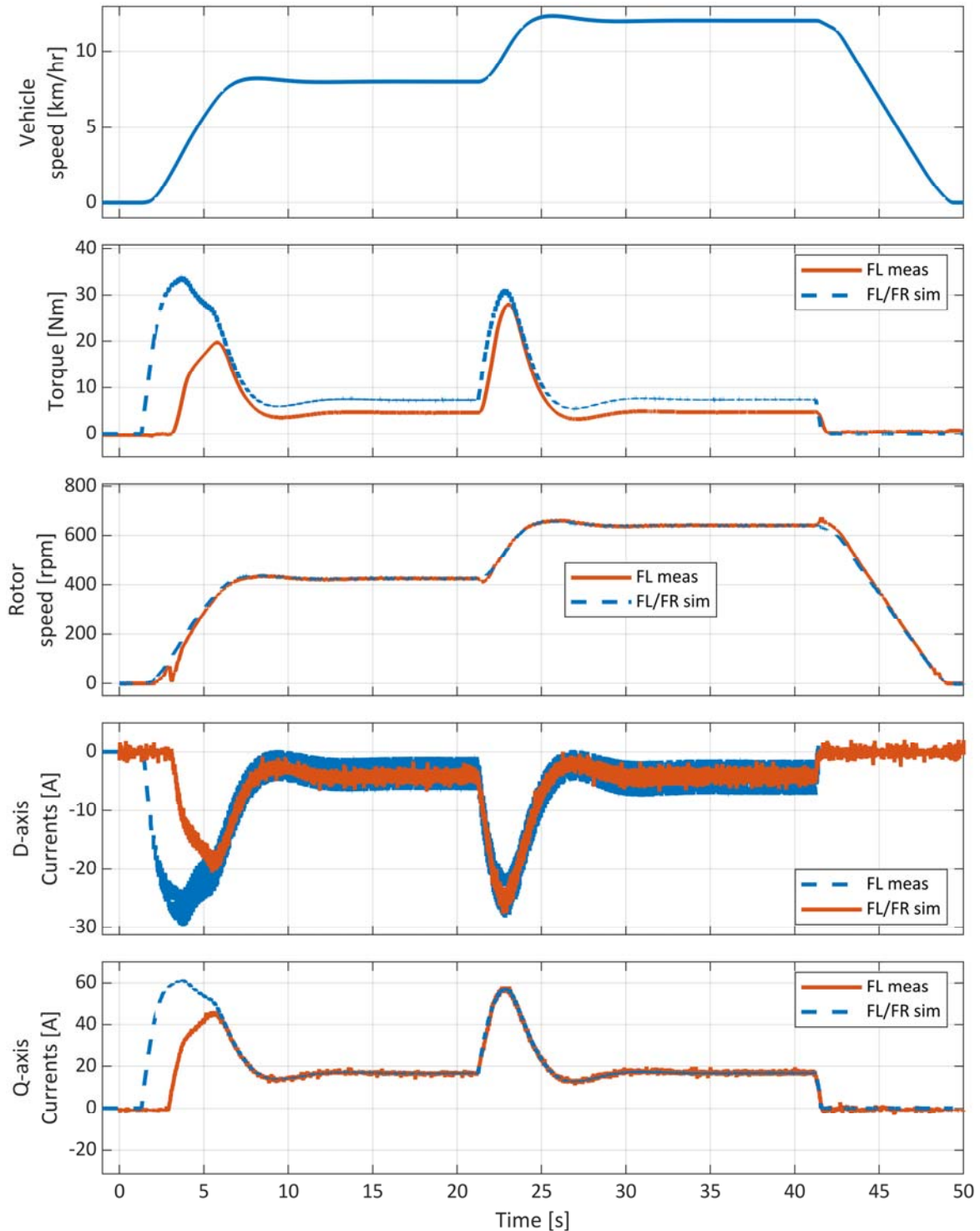


Figure 6-6: Experimental measurements with open-loop interface between real-time simulation and real test bench. Measurements from bench are compared to real-time simulations.

Due to the limitation of the speed controller discussed earlier, the torque feedback is enabled after 10 sec.

The same speed-based driving cycle presented earlier is also used here and the results are shown in in Figure 6-7. The vehicle speed in the simulation follows the drive cycle well as

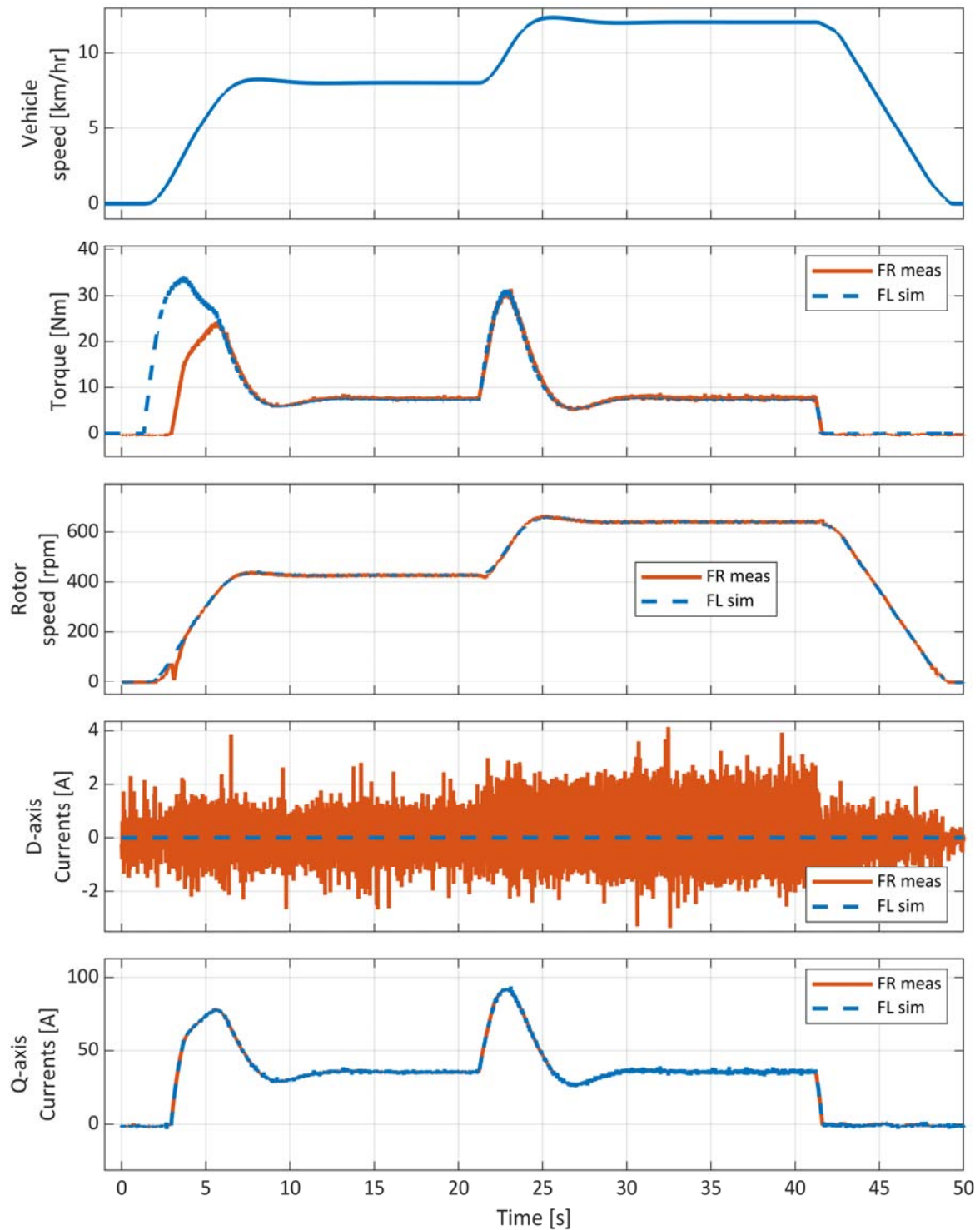


Figure 6-7: Experimental measurements with closed-loop interface between real-time simulation and real test bench.

seen in the first subplot. There are no visible differences in the vehicle speed between the two results shown in Figure 6-6 & Figure 6-7. Since identical look-up table using measured torque and q-axis current is used in the dyno test bench and the real-time simulation to convert the torque reference to current references, the mechanical losses get automatically included. Therefore, the shaft torques shown in the second subplot for both FR and FL electric machines are identical except during the initial acceleration as explained earlier. Hence, no lateral motion of the vehicle was observed during the test. The FR and FL rotor speeds in the third subplot are almost identical with some minor differences due to the speed controller. Since, the speed feedback is not used, the difference in speed will not result into slip detection in the vehicle model. Finally, the d- and q-axis currents in the last two subplots are also identical except for higher noise in the d-axis currents as observed before.

6.3.3 Anti-slip control verification using OLM 1

To demonstrate the capability of the proposed test bench, a driving scenario is created to simulate wheel slip. The drive cycle results without any control of wheel slip is presented in Figure 6-8, and Figure 6-9 presents the case when an anti-slip control is implemented to prevent wheel slip. The details of the implemented anti-slip control method are presented in [64]. The same speed-based drive cycle presented earlier is used with a slight modification. In the drive cycle, the vehicle is driven on asphalt road with a friction coefficient of 0.9 for the first 15 secs after which it enters an ice-road with a friction coefficient of 0.2.

The traction torque that can be transferred to the road is limited by the coefficient of friction. The traction torque demanded by the driver during acceleration in the ice-road exceeds this limit which causes the wheels to spin. The wheel spin can be observed by the sudden acceleration of rotor speed between 22 to 24 sec in Figure 6-8 where no wheel slip control is applied. When the anti-slip function is enabled, the reference torque is reduced when slip is detected as observed by the reduction of electric machine torque in Figure 6-9. Therefore, sudden acceleration of rotor speed is avoided, and the rotor speed follows the vehicle speed more closely. However, some acceleration of rotor speed is still observed which is due to the delay in the detection of wheel slip in the control.

Once again, five subplots are shown in the two figures in the same order as before. The vehicle speed in Figure 6-8 follows the driving cycle quite well even though there is wheel slip. This is because the vehicle speed is calculated considering vehicle mass which is comparatively much larger. In comparison, the vehicle takes longer time to reach the target speed of 12 km/h when the anti-slip control is enable as seen in Figure 6-9. The anti-slip control reduces the reference torque demanded by the drive model causing a slower acceleration of the vehicle. The reference torque is restored to the value demand by the driver model when the anti-slip control is not needed. The sudden increase in reference torque causes the vehicle speed to increase as well. It can be observed as a bigger overshoot in vehicle speed at the end of acceleration around 27 sec in Figure 6-9. The bigger overshoot causes the driver model to release the gas pedal to bring the vehicle to the target speed. This causes, the reference torque to drop to zero momentarily around 28 sec. The torque, rotor speed and d-and q-axis currents between measurement and simulation are like the results presented earlier.

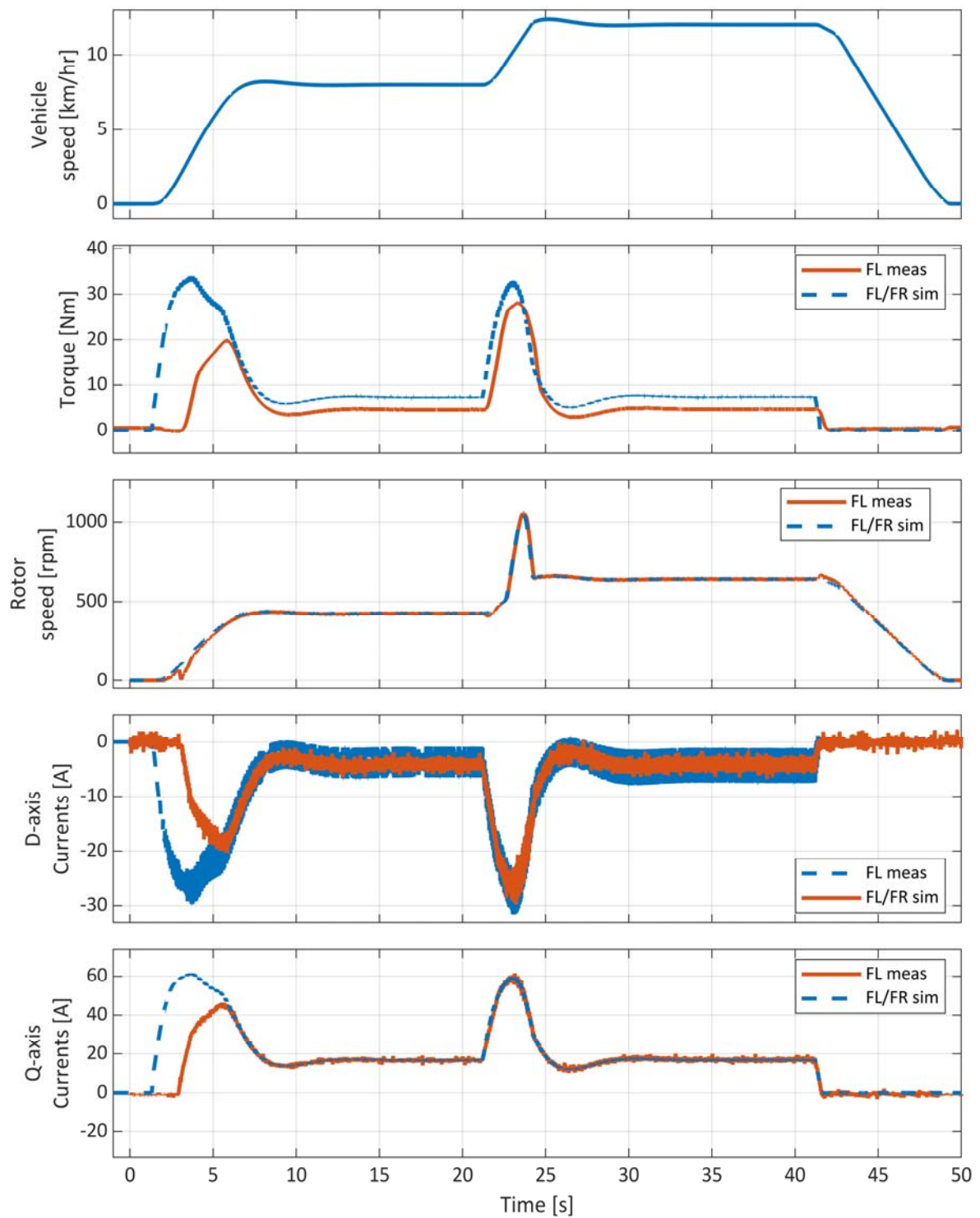


Figure 6-8: Experimental measurements showing wheel spin and lock while driving on an ice road. The anti-spin and anti-lock control strategy is disabled.

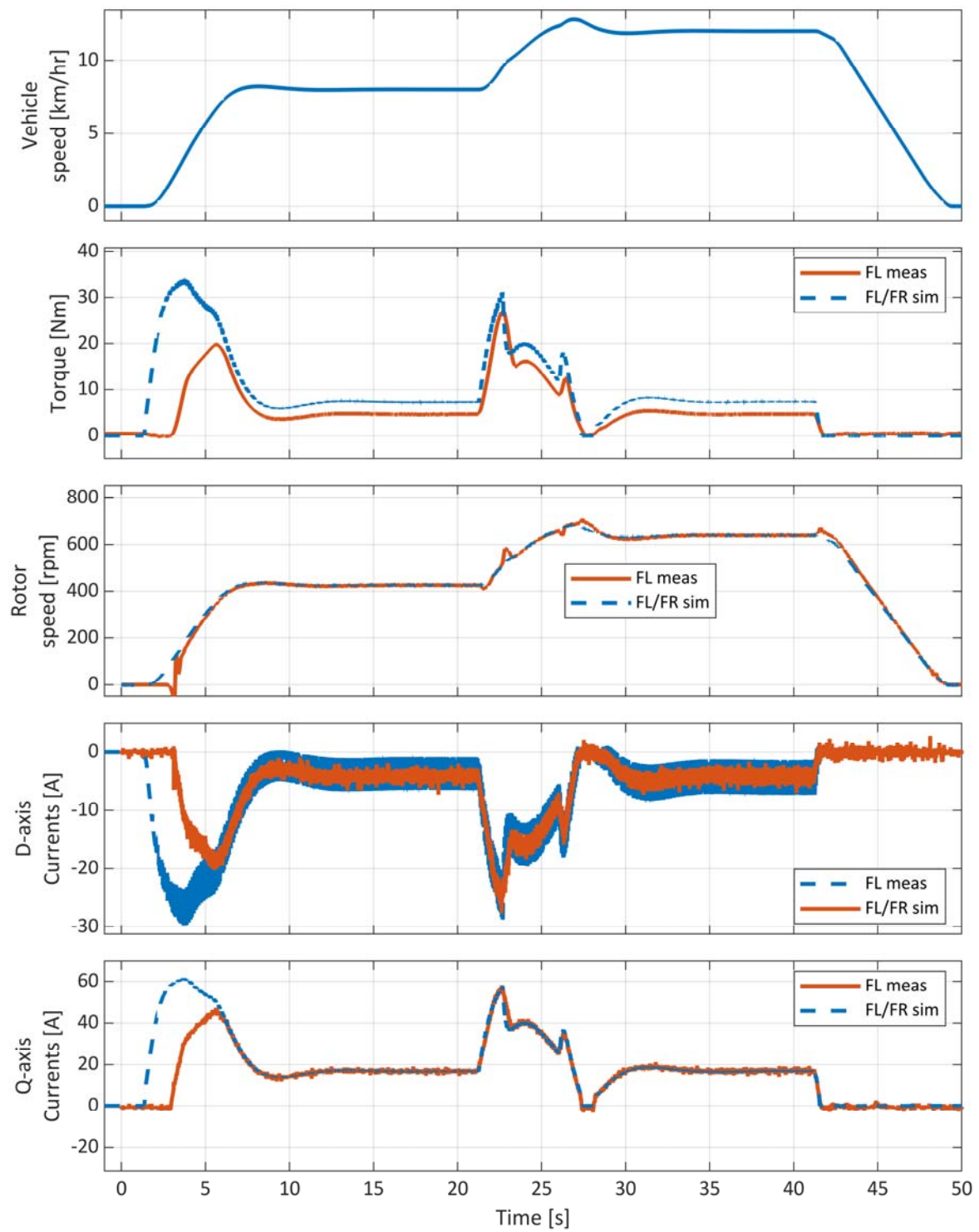


Figure 6-9: Experimental measurements showing wheel spin and lock while driving on an ice road. The anti-spin and anti-lock control strategy is enabled.

Chapter 7

Conclusions and Future Work

7.1 Conclusions

The design, modeling, and verification of a distributed drivetrain for battery electric vehicles are presented in this work. First, a standardized drivetrain is conceptualized. Then, the drivetrain concept is evaluated by simulating the drive cycle energy consumption. Two alternative methods for drivetrain verifications – PHIL and MHIL – are also experimentally evaluated.

A dimensioning method is proposed to size the standardized drivetrain's torque and power. Standardized electric machine torque and power requirements for four-passenger BEVs are derived. The electric drivetrain and road load are modeled, and drive cycle simulations are performed. The simulation results show that the electric machine and transmission have higher losses than the inverter. In addition, it is shown that the high-speed drive cycles have the highest energy consumption. Therefore, special attention should be given to optimizing the drivetrain's efficiency for high-speed driving to improve the range. Simulation results also show that the standardized drivetrain has the highest drive cycle efficiency for light vehicles. Furthermore, the driving efficiency of C class, D class, and performance vehicles vary by less than 3%.

An open loop control of a machine emulator is discussed in this work. The control method results in a flexible and cost-effective PHIL test bench since it allows the utilization of identical VSCs for IUT and the emulator. The simulation results show minimal differences between voltage and currents at the emulator terminals and modeled machine. However, common-mode currents are observed because the DC link of the emulator VSC and the IUT are connected to the same DC power source. The common-mode current is directly proportional to the fundamental component of the line voltage, and it affects the accuracy of voltages and currents at the emulator terminals.

The open loop control of the emulator is verified by prototyping a 60-kW PHIL test bench. Comparing measurements from the PHIL bench to simulations of an equivalent PMSM drive shows a more significant deviation in line voltage and reactive power. The reason is that accuracy of the voltage is dependent on the estimation of the coupling network parameters. A modified version of the common-mode current control method is used in the experiments, which shows significant improvement in the regulation of the common-mode current. The experimental results from the PHIL test bench are further compared to an equivalent dynamometer test bench. Although the phase currents between the two test benches are slightly different, significant differences were observed between line voltages and active and

reactive power. The experimental results show that the accuracy of the voltage and currents of the machine emulator depends on the machine parameters' estimation.

The bandwidth of the machine emulator is shown to be dependent on the coupling network inductance when the DC link of the emulator VSC can be controlled independently because the frequency-dependent voltage drop across the coupling network limits the capability of the emulator VSC to implement the voltage references demanded by the emulator control. An analytical method is derived to dimension the coupling network inductance and it is verified using simulations. Simulation results show that the operating boundary of the emulator is correlated to the analytical derivation. The design of a high bandwidth emulator is proposed using a transformer as a coupling network. The high bandwidth emulator is verified using simulations. Simulation results show that the emulator operating region covers the entire operating area of the modeled PMSM.

An MHIL test bench for multi-motor drivetrain systems has been designed and experimentally verified. The MHIL bench consists of a real-time simulator interfaced with a 60-kW dyno test bench. To interface the dyno test bench and the real-time simulations, two methods - open and closed loops - are proposed and investigated in experiments. The experimental results show that the proposed interface methods can be used to observe the impacts of vehicle dynamics on drivetrain performance. Overall, the capability of the proposed test method in verifying both drivetrain components and control functions is sufficiently demonstrated. Although some minor differences in the shaft torque between the real-time simulation and the dyno test bench are observed for the open-loop interface, it does not result in any unintended vehicle motion. The differences in the shaft torque can be reduced by improving the real-time models. It is implemented for the closed-loop interface because the shaft torque must be identical between the real-time simulation and the dyno test bench to avoid unintended lateral movement of the vehicle when using torque feedback.

7.2 On-Going and Future Work

The research can be extended and utilized by investigating the following research topics in future projects.

- The voltage, active power, and reactive power accuracy of the PHIL test bench can be improved by better estimation of the coupling network parameters and by including the iron-core losses in the model of the coupling network.
- Significant difference has been observed in voltage, active power, and reactive power when the emulator is compared to a physical machine. The accuracy of the emulator in comparison to the physical machine can be improved by utilizing measurements on the dynamometer bench.
- The high bandwidth emulator has been verified only in simulations. Therefore, additional verification can be performed by prototyping the PHIL test bench.
- The speed controller used for the dynamometer test bench limits the capability of the MHIL test bench. Due to the limitation, the speed and torque could not be emulated simultaneously. Therefore, the speed controller should be improved.

References

- [1] I. E. Agency, "Global EV outlook 2022," Internal Energy Agency, 2022.
- [2] I. E. Agency, "Evolution of Li-ion battery price, 1995-2019," Internal Energy Agency, 2020.
- [3] T. a. Environment, "Hitting the EV inflection point," European Federation for Transport and Environment, 2021.
- [4] K. Li, F. Chou and J. Yen, "Real-Time, Energy-Efficient Traction Allocation Strategy for the Compound Electric Propulsion System," in *IEEE/ASME Transactions on Mechatronics*, vol. 22, no. 3, pp. 1371-1380, June 2017, doi: 10.1109/TMECH.2017.2667725.
- [5] G. De Filippis, B. Lenzo, A. Sorniotti, P. Gruber and W. De Nijs, "Energy-Efficient Torque-Vectoring Control of Electric Vehicles With Multiple Drivetrains," in *IEEE Transactions on Vehicular Technology*, vol. 67, no. 6, pp. 4702-4715, June 2018, doi: 10.1109/TVT.2018.2808186.
- [6] J. Huang, Y. Liu, M. Liu, M. Cao and Q. Yan, "Multi-Objective Optimization Control of Distributed Electric Drive Vehicles Based on Optimal Torque Distribution," in *IEEE Access*, vol. 7, pp. 16377-16394, 2019, doi: 10.1109/ACCESS.2019.2894259.
- [7] J. Hu, J. Tao, F. Xiao, X. Niu and C. Fu, "An Optimal Torque Distribution Control Strategy for Four-Wheel Independent Drive Electric Vehicles Considering Energy Economy," in *IEEE Access*, vol. 7, pp. 141826-141837, 2019, doi: 10.1109/ACCESS.2019.2944479
- [8] X. Sun et al., "MPTC for PMSMs of EVs With Multi-Motor Driven System Considering Optimal Energy Allocation," in *IEEE Transactions on Magnetics*, vol. 55, no. 7, pp. 1-6, July 2019, Art no. 8104306, doi: 10.1109/TMAG.2019.2904289.
- [9] C. Lin, S. Liang, J. Chen and X. Gao, "A Multi-Objective Optimal Torque Distribution Strategy for Four In-Wheel-Motor Drive Electric Vehicles," in *IEEE Access*, vol. 7, pp. 64627-64640, 2019, doi: 10.1109/ACCESS.2019.2917313.
- [10] X. Sun, Z. Shi, Y. Cai, G. Lei, Y. Guo and J. Zhu, "Driving-Cycle-Oriented Design Optimization of a Permanent Magnet Hub Motor Drive System for a Four-Wheel-Drive Electric Vehicle," in *IEEE Transactions on Transportation Electrification*, vol. 6, no. 3, pp. 1115-1125, Sept. 2020, doi: 10.1109/TTE.2020.3009396
- [11] H. Peng, W. Wang, C. Xiang, L. Li and X. Wang, "Torque Coordinated Control of Four In-Wheel Motor Independent-Drive Vehicles With Consideration of the Safety and Economy," in *IEEE Transactions on Vehicular Technology*, vol. 68, no. 10, pp. 9604-9618, Oct. 2019, doi: 10.1109/TVT.2019.2935617.
- [12] W. Wang, Y. Li, J. Shi and C. Lin, "Vibration Control Method for an Electric City Bus Driven by a Dual Motor Coaxial Series Drive System Based on Model Predictive Control," in *IEEE Access*, vol. 6, pp. 41188-41200, 2018, doi: 10.1109/ACCESS.2018.2859356.
- [13] B. Leng, L. Xiong, Z. Yu, K. Sun and M. Liu, "Robust Variable Structure Anti-Slip Control Method of a Distributed Drive Electric Vehicle," in *IEEE Access*, vol. 8, pp. 162196-162208, 2020, doi: 10.1109/ACCESS.2020.3021694.
- [14] K. Saito and H. Akagi, "A Power Hardware-in-the-Loop (P-HIL) Test Bench Using Two Modular Multilevel DSCC Converters for a Synchronous Motor Drive," in *IEEE Transactions on Industry Applications*, vol. 54, no. 5, pp. 4563-4573, Sept.-Oct. 2018, doi: 10.1109/TIA.2018.2833424.
- [15] F. Huerta, R. L. Tello and M. Prodanovic, "Real-Time Power-Hardware-in-the-Loop Implementation of Variable-Speed Wind Turbines," in *IEEE Transactions on Industrial Electronics*, vol. 64, no. 3, pp. 1893-1904, March 2017, doi: 10.1109/TIE.2016.2624259.
- [16] K. S. Amitkumar, R. S. Kaarthik and P. Pillay, "A Versatile Power-Hardware-in-the-Loop-Based Emulator for Rapid Testing of Transportation Electric Drives," in *IEEE Transactions on Transportation Electrification*, vol. 4, no. 4, pp. 901-911, Dec. 2018, doi: 10.1109/TTE.2018.2857216.
- [17] A. Schmitt, J. Richter, M. Braun and M. Doppelbauer, "Power Hardware-in-the-Loop Emulation of Permanent Magnet Synchronous Machines with Nonlinear Magnetism - Concept & Verification," *PCIM Europe 2016; International Exhibition and Conference for Power Electronics, Intelligent Motion, Renewable Energy and Energy Management*, 2016, pp. 1-8.

- [18] K. Saito and H. Akagi, "A Real-Time Real-Power Emulator of a Medium-Voltage High-Speed Induction Motor Loaded With a Centrifugal Compressor," in *IEEE Transactions on Industry Applications*, vol. 55, no. 5, pp. 4821-4833, Sept.-Oct. 2019, doi: 10.1109/TIA.2019.2928498.
- [19] O. Vodyakho, M. Steurer, C. S. Edrington and F. Fleming, "An Induction Machine Emulator for High-Power Applications Utilizing Advanced Simulation Tools With Graphical User Interfaces," in *IEEE Transactions on Energy Conversion*, vol. 27, no. 1, pp. 160-172, March 2012, doi: 10.1109/TEC.2011.2179302.
- [20] R. S. Kaarthik and P. Pillay, "Emulation of a permanent magnet synchronous generator in real-time using power hardware-in-the-loop," 2016 IEEE International Conference on Power Electronics, Drives and Energy Systems (PEDES), 2016, pp. 1-6, doi: 10.1109/PEDES.2016.7914290.
- [21] A. Schmitt, J. Richter, M. Gommeringer, T. Wersal and M. Braun, "A novel 100 kW power hardware-in-the-loop emulation test bench for permanent magnet synchronous machines with nonlinear magnetics," 8th IET International Conference on Power Electronics, Machines and Drives (PEMD 2016), 2016, pp. 1-6, doi: 10.1049/cp.2016.0280.
- [22] A. Schmitt, J. Richter, U. Jurkewitz and M. Braun, "FPGA-based real-time simulation of nonlinear permanent magnet synchronous machines for power hardware-in-the-loop emulation systems," IECON 2014 - 40th Annual Conference of the IEEE Industrial Electronics Society, 2014, pp. 3763-3769, doi: 10.1109/IECON.2014.7049060.
- [23] M. Steurer, C. S. Edrington, M. Sloderbeck, W. Ren and J. Langston, "A Megawatt-Scale Power Hardware-in-the-Loop Simulation Setup for Motor Drives," in *IEEE Transactions on Industrial Electronics*, vol. 57, no. 4, pp. 1254-1260, April 2010, doi: 10.1109/TIE.2009.2036639.
- [24] M. Ashourianjozdani, L. A. C. Lopes and P. Pillay, "Converter-based PMSG emulator: A testbed for renewable energy experiments," 2017 IEEE International Electric Machines and Drives Conference (IEMDC), 2017, pp. 1-7, doi: 10.1109/IEMDC.2017.8002294.
- [25] L. Yang et al., "Three-Phase Power Converter-Based Real-Time Synchronous Generator Emulation," in *IEEE Transactions on Power Electronics*, vol. 32, no. 2, pp. 1651-1665, Feb. 2017, doi: 10.1109/TPEL.2016.2553168.
- [26] R. S. Kaarthik, J. Maisonneuve and P. Pillay, "Real-Time Emulation of a Pressure-Retarded Osmotic Power Generation System," in *IEEE Transactions on Industry Applications*, vol. 53, no. 6, pp. 5768-5776, Nov.-Dec. 2017, doi: 10.1109/TIA.2017.2732939.
- [27] J. Wang, Y. Ma, L. Yang, L. M. Tolbert and F. Wang, "Power converter-based three-phase induction motor load emulator," 2013 Twenty-Eighth Annual IEEE Applied Power Electronics Conference and Exposition (APEC), 2013, pp. 3270-3274, doi: 10.1109/APEC.2013.6520769.
- [28] M. A. Masadeh and P. Pillay, "Induction motor emulation including main and leakage flux saturation effects," 2017 IEEE International Electric Machines and Drives Conference (IEMDC), 2017, pp. 1-7, doi: 10.1109/IEMDC.2017.8002207.
- [29] I. Vernica, F. Blaabjerg and K. Ma, "Mission profile emulator for the power electronics systems of motor drive applications," 2017 19th European Conference on Power Electronics and Applications (EPE'17 ECCE Europe), 2017, pp. P.1-P.10, doi: 10.23919/EPE17ECCEurope.2017.8099241.
- [30] W. Zhao, Q. Song, W. Liu, M. Ahmad and Y. Li, "Distributed Electric Powertrain Test Bench With Dynamic Load Controlled by Neuron PI Speed-Tracking Method," in *IEEE Transactions on Transportation Electrification*, vol. 5, no. 2, pp. 433-443, June 2019, doi: 10.1109/TTE.2019.2904652.
- [31] A. Bouscayrol, "Different types of Hardware-In-the-Loop simulation for electric drives," 2008 IEEE International Symposium on Industrial Electronics, 2008, pp. 2146-2151, doi: 10.1109/ISIE.2008.4677304.
- [32] F. Mocera and A. Somà, "Study of a Hardware-In-the-Loop bench for hybrid electric working vehicles simulation," 2017 Twelfth International Conference on Ecological Vehicles and Renewable Energies (EVER), 2017, pp. 1-8, doi: 10.1109/EVER.2017.7935880.
- [33] K. Etzold et al., "Function Development With an Electric-Machine-in-the-Loop Setup: A Case Study," in *IEEE Transactions on Transportation Electrification*, vol. 5, no. 4, pp. 1419-1429, Dec. 2019, doi: 10.1109/TTE.2019.295228.
- [34] R. M. Schupbach and J. C. Balda, "A versatile laboratory test bench for developing powertrains of electric vehicles," *Proceedings IEEE 56th Vehicular Technology Conference*, 2002, pp. 1666-1670 vol.3, doi: 10.1109/VETECF.2002.1040499.

- [35] R. Trigui, B. Jeanneret, B. Malaquin and C. Plasse, "Performance Comparison of Three Storage Systems for Mild HEVs Using PHIL Simulation," in *IEEE Transactions on Vehicular Technology*, vol. 58, no. 8, pp. 3959-3969, Oct. 2009, doi: 10.1109/TVT.2009.2028146.
- [36] Sung Chul Oh, "Evaluation of motor characteristics for hybrid electric vehicles using the hardware-in-the-loop concept," in *IEEE Transactions on Vehicular Technology*, vol. 54, no. 3, pp. 817-824, May 2005, doi: 10.1109/TVT.2005.847228.
- [37] B. Tabbache, Y. Aboub, K. Marouani, A. Kheloui and M. E. H. Benbouzid, "A simple and effective hardware-in-the-loop simulation platform for urban electric vehicles," *2012 First International Conference on Renewable Energies and Vehicular Technology*, 2012, pp. 251-255, doi: 10.1109/REVET.2012.6195279.
- [38] E. A. Grunditz, "Design and Assessment of Battery Electric Vehicle Powertrain, with Respect to Performance, Energy Consumption and Electric Motor Thermal Capability", Chalmers University of Technology, Gothenburg, 2016.
- [39] E. A. Grunditz and T. Thiringer, "Performance Analysis of Current BEVs Based on a Comprehensive Review of Specifications," in *IEEE Transactions on Transportation Electrification*, vol. 2, no. 3, pp. 270-289, Sept. 2016, doi: 10.1109/TTE.2016.2571783.
- [40] Focus2Move, "Europe best selling cars. The top 100 in 2017," [Online]. Available: <https://www.focus2move.com/europe-best-selling-cars/>. [Accessed 01 02 2018].
- [41] N. Sharma and Y. Liu, "Multiple electrical machines applied for high drive train efficiency," *2018 IEEE International Conference on Electrical Systems for Aircraft, Railway, Ship Propulsion and Road Vehicles & International Transportation Electrification Conference (ESARS-ITEC)*, 2018, pp. 1-7, doi: 10.1109/ESARS-ITEC.2018.8607485.
- [42] U. N. E. C. f. Europe, "TEM Standard and Recommended Practices," 2002.
- [43] G. Mohan, F. Assadian and S. Longo, "Comparative analysis of forward-facing models vs backward facing models in powertrain component sizing," *IET Hybrid and Electric Vehicles Conference 2013 (HEVC 2013)*, 2013, pp. 1-6, doi: 10.1049/cp.2013.1920.
- [44] M. Ridwan, M. N. Yuniarto and Soedibyo, "Electrical equivalent circuit based modeling and analysis of brushless direct current (BLDC) motor," *2016 International Seminar on Intelligent Technology and Its Applications (ISITIA)*, 2016, pp. 471-478, doi: 10.1109/ISITIA.2016.7828706.
- [45] M. E. Şahin, F. Blaabjerg and A. Sangwongwanich, "Modeling of supercapacitors based on simplified equivalent circuit," in *CPSS Transactions on Power Electronics and Applications*, vol. 6, no. 1, pp. 31-39, March 2021, doi: 10.24295/CPSSPEA.2021.00003.
- [46] A. Andersson, "Electric Machine Control of Energy Efficient Electric Drive System", Chalmers University of Technology, Gothenburg, 2018.
- [47] L. Harnefors, "Current Control," in *Control of Variable-Speed Drives*, Applied Signal Processing and Control, Department of Electronics, Mälardalen University, 2002, pp. 19 - 29.
- [48] G. Mademlis, "Inverter Design for SiC-based Electric Drive Systems with Optimal Redundant States Control of Space Vector Modulation", Chalmers University of Technology, Gothenburg, 2021.
- [49] J. Tang, "Synchronous Machines with High-Frequency Brushless Excitation for Vehicle Application," Gothenburg, Chalmers University of Technology, Gothenburg, 2019, pp. 55-59.
- [50] W. C. Duesterhoeft, M. W. Schulz and E. Clarke, "Determination of Instantaneous Currents and Voltages by Means of Alpha, Beta, and Zero Components," *Transactions of the American Institute of Electrical Engineers*, pp. 1248 - 1255, 1951.
- [51] R. H. Park, "Two-Reaction Theory of Synchronous Machines Generalized Method of Analysis - Part I," *Transactions of the American Institute of Electrical Engineers*, pp. 716 - 727, 1929.
- [52] J. -i. Itoh and T. Abe, "Circulation current reduction for a motor simulator system using a power converter with a common mode transformer," *2009 IEEE 6th International Power Electronics and Motion Control Conference*, 2009, pp. 1662-1667, doi: 10.1109/IPEMC.2009.5157658.
- [53] J. Tang, Design and Control of Electrically Excited Synchronous Machines for Vehicle Application, Chalmers University of Technology, Gothenburg, 2021.
- [54] M. Novak, J. Novak, Z. Novak, J. Chysky and O. Sivkov, "Efficiency mapping of a 100 kW PMSM for traction applications," *2017 IEEE 26th International Symposium on Industrial Electronics (ISIE)*, 2017, pp. 290-295, doi: 10.1109/ISIE.2017.8001262

- [55] C. Candelo-Zuluaga, A. Garcia Espinosa, J. -R. Riba, P. Tubert Blanch and G. Rojas-Dueñas, "Fast and Efficient PMSM Electromagnetic Parameter Identification Methodology from the Efficiency Map," *IECON 2020 The 46th Annual Conference of the IEEE Industrial Electronics Society*, 2020, pp. 1584-1589, doi: 10.1109/IECON43393.2020.9254966.
- [56] R. Andersson, "On the Design of Electric Traction Machines : Design and Analysis of an Interior Permanent Magnet Synchronous Machine for Heavy Commercial Vehicles", Lund University, Lund, 2019.
- [57] Y. -R. Lee, Y. -C. Kwon and S. -K. Sul, "DC-Link Voltage Design of High-Bandwidth Motor Emulator for Interior Permanent-Magnet Synchronous Motors," *2018 IEEE Energy Conversion Congress and Exposition (ECCE)*, 2018, pp. 4453-4459, doi: 10.1109/ECCE.2018.8558050.
- [58] R. Shafaei, M. C. G. Perez and M. Ordonez, "Planar Transformers in LLC Resonant Converters: High-Frequency Fringing Losses Modeling," in *IEEE Transactions on Power Electronics*, vol. 35, no. 9, pp. 9632-9649, Sept. 2020, doi: 10.1109/TPEL.2020.2971424.
- [59] "CarMaker Reference Manual Version 6.0.5," IPG Automot. GmbH,, Karlsruhe, Germany, 2017.
- [60] "Driver's Manual Version 6.6.1 IPG Driver," IPG Automot. GmbH, Karlsruhe, Germany,, 2017.
- [61] dSPACE, "XSG Electric Component Models," [Online]. Available: <https://www.dspace.com>. [Accessed 10 March 2022].
- [62] S. Hall, "Testing and Modeling of Electrical Traction Machines," Lund University, Lund, 2019, pp. 11-19.
- [63] "FS400R07A3E3,"Infineon,[Online]. Available: <https://www.infineon.com> [Accessed 04 Feb 2020].
- [64] B. Jiang, N. Sharma, Y. Liu and C. Li, "Acceleration-based wheel slip control realized with decentralised electric drivetrain systems," *IET Electrical Systems in Transportation*, 2022.

Appendix 1

Data of ICEVs

Manufacturer	Model	Variants	Length (mm)	Width (mm)	Height (mm)	Curb Weight (kg)	Gross vehicle weight (kg)
Fiat	500	Pop	3571	1627	1488	865	1345
Volkswagen	Up!	Take up!	3600	1641	1504	926	1320
Fiat	Panda	Pop	3653	1643	1551	940	1420
Toyota	Yaris	Active	3945	1695	1510	975	1450
Volkswagen	Polo	S	3972	1682	1453	1055	1570
Peugeot	208	Active	3973	1739	1460	960	1520
Skoda	Fabia	S	3992	1732	1467	1005	1535
Citroen	C3	Touch	3996	1749	1474	976	1510
Opel	Corsa	Sting	4021	1736	1479	1000	1585
Ford	Fiesta	Style	4040	1735	1476	1113	1620
Hyundai	i20	SE	4045	1730	1449	980	1580
Seat	Ibiza	S	4059	1780	1444	1091	1510
Renault	Clio	Expression	4062	1732	1448	1059	1564
Dacia	Sandero	Access	4069	1733	1519	969	1490
Renault	Captur	Expression+	4122	1778	1566	1184	1682
Peugeot	2008	Active	4159	1739	1556	1045	1590
Audi	A3	SE	4241	1777	1424	1180	1740
Fiat	500X	Pop	4248	1796	1600	1275	1875
Volkswagen	Golf	S	4258	1799	1492	1206	1720
Seat	Leon	SC FR Technology	4263	1816	1459	1213	1750
Opel	Mokka	Design Nav	4275	1780	1658	1280	1789
Mercedes	A Class	SE 6 Speed Manual	4299	1780	1433	1370	1935
Dacia	Duster	Access	4315	1822	1625	1147	1697
Toyota	Auris	Hatchback Active	4330	1760	1475	1235	1735
Renault	Megane	Expression+	4359	1814	1447	1340	1801
Ford	Focus	Zetec	4360	1823	1469	1276	1900
Toyota	C-HR	Icon	4360	1795	1565	1320	1845
Fiat	Tipo	Hatchback Easy	4368	1792	1495	1270	1770
Opel	Astra	Design	4370	1809	1510	1169	1760
Nissan	Qashqai	Visia	4394	1806	1590	1331	1860
Peugeot	3008	Active	4447	1841	1624	1250	1910
Renault	Kadjar	Expression+	4449	1836	1607	1306	1853
Renault	Scenic	Expression+	4406	1866	1653	1413	2017
Hyundai	Tucson	S	4475	1850	1650	1379	1895
Kia	Sportage	1	4480	1855	1635	1454	1895
Volkswagen	Tiguan	S	4486	1839	1654	1490	2120
Volkswagen	Touran	S	4527	1829	1659	1436	2060
Ford	Kuga	Zetec	4531	1838	1689	1560	2100
Audi	A4	Saloon SE	4726	1842	1427	1320	1890
Volkswagen	Passat	S	4767	1832	1476	1367	1950
Mercedes	GLC	Sport	4656	1890	1639	1735	2400
Mercedes	C Class	SE	4686	1810	1442	1450	2015

Manufacturer	Model	Variants	Acceleration (sec)	Top speed (km/h)	Tyre size
			0 - 100 km/h		
Fiat	500	Pop	12,9	160	175/65 R 14
Volkswagen	Up!	Take up!	14,4	162	165/70 R14
Fiat	Panda	Pop	14,2	164	175/65 R14
Toyota	Yaris	Active	15,3	155	175/65 R15
Volkswagen	Polo	S	15,5	161	175/65 R14
Peugeot	208	Active	13,8	166	185/65 R15
Skoda	Fabia	S	15,7	160	185/60 R15
Citroen	C3	Touch	14	172	195/65 R 15
Opel	Corsa	Sting	15,5	160	185/65 R 15
Ford	Fiesta	Style	14,9	160	195/60 R15
Hyundai	i20	SE	12,8	170	195 /55 R16
Seat	Ibiza	S	14,7	167	185/65 R15
Renault	Clio	Expression	14,5	167	185/65 R15
Dacia	Sandero	Access	14,2	158	185/65 R15
Renault	Captur	Expression+	13,2	171	205/60 R16
Peugeot	2008	Active	13,5	169	195/60 R16
Audi	A3	SE	9,9	206	205/55 R16
Fiat	500X	Pop	11,5	180	215/60 R16
Volkswagen	Golf	S	11,9	180	195/65 R15
Seat	Leon	SC FR Technology	8,9	203	205/50 R17
Opel	Mokka	Design Nav	11,8	170	215/60 R 17
Mercedes	A Class	SE 6 Speed Manual	10,6	190	205/55 R16
Dacia	Duster	Access	11	170	215/65 R 16
Toyota	Auris	Hatchback Active	12,6		
Renault	Megane	Expression+	10,6	197	205/55 R16
Ford	Focus	Zetec	12,5	185	205/55 R16
Toyota	C-HR	Icon	10,9	190	
Fiat	Tipo	Hatchback Easy	12,1	185	195/55 R15
Opel	Astra	Design	12,6	185	205/55 R 16
Nissan	Qashqai	Visia	10,6	185	215/65 R16
Peugeot	3008	Active	10,8	188	215/65 R17
Renault	Kadjar	Expression+	10,1	192	215/65 R16
Renault	Scenic	Expression+	11,3	182	195/55 R20
Hyundai	Tucson	S	11,5	182	215/70 R16
Kia	Sportage	1	11,1	182	215/70 R16
Volkswagen	Tiguan	S	10,5	190	215/65 R17
Volkswagen	Touran	S	11,3	190	205/60 R16
Ford	Kuga	Zetec	12,6	180	235/55 R17
Audi	A4	Saloon SE	8,7	209	225/50 R17
Volkswagen	Passat	S	9,7	208	215/60 R16
Mercedes	GLC	Sport	7,3	222	235/60 R18
Mercedes	C Class	SE	7,5	237	205/60 R16

Manufacturer	Model	Energy converter				
		Variant	Power (kW)		Torque (Nm)	
Fiat	500	1.2 69 HP Start&Stop	51	5500 rpm	102	3000 rpm
Volkswagen	Up!	1.0 litre 60 PS	44	5000 rpm	95	3000 - 4300 rpm
Fiat	Panda	1.2 69 hp	51	5500 rpm	102	3000 rpm
Toyota	Yaris	1.0 Petrol 5-Speed Manual	51	6000 rpm	95	4300 - 6000 rpm
Volkswagen	Polo	1.0 ltr 60 PS	44	5000 - 6000 rpm	95	3000 - 4300 rpm
Peugeot	208	1.2 L Pure Tech 68	50	5750 rpm	106	2750 rpm
Skoda	Fabia	1.0 MPI 60 PS	44	5000 - 6000 rpm	95	3000 - 4300 rpm
Citroen	C3	PureTech 68 Manual	50	5750 rpm	106	2750 rpm
Opel	Corsa	1.4 i (75PS) ecoFLEX	55	4200 - 6000 rpm	130	4000 rpm
Ford	Fiesta	1.1 Ti VCT (70 PS)	52		110	
Hyundai	i20	1.2 Petrol 84PS	62	6000 rpm	122	4000 rpm
Seat	Ibiza	1.0 MPI 75PS	55	6200 rpm	95	3000 - 4300 rpm
Renault	Clio	1.2 16V 75	54	5500 rpm	107	4250 rpm
Dacia	Sandero	SCe 75	54	6300 rpm	97	3500 rpm
Renault	Captur	ENERGY TCE 90 S&S	66	5000 rpm	140	2250 rpm
Peugeot	2008	1.2 L Pure Tech 82	60	5750 rpm	118	2750 rpm
Audi	A3	1.0 TFSI	85	5000 - 5500 rpm	200	2000 - 3500 rpm
Fiat	500X	1.6 E-Torq 110 hp	81	5500 rpm	152	4500 rpm
Volkswagen	Golf	1.0 ltr TSI 85 PS	63	5000 - 5500 rpm	175	2000 - 3000 rpm
Seat	Leon	1.4 TSI 125PS	92	5000 - 6000 rpm	200	1400 - 4000 rpm
Opel	Mokka	1.6i (115PS) Start/Stop FWD	85	6200 rpm	155	4000 rpm
Mercedes	A Class	A 160	75	4500 - 6000 rpm	180	1200 - 3500 rpm
Dacia	Duster	SCe 115 4x2	84	5500 rpm	156	4000 rpm
Toyota	Auris	1.33 Petrol (99 hp)	73	6000 rpm	128	3800 rpm
Renault	Megane	ENERGY TCe 130	97	5500 rpm	205	2000 rpm
Ford	Focus	1.0 Ford EcoBoost	74		170	
Toyota	C-HR	1.2 Petrol Turbo (115 hp)	85	5600 rpm	185	1500 - 4000 rpm
Fiat	Tipo	1.4 95 hp	70	6000 rpm	127	4500 rpm
Opel	Astra	1.4i (100PS)	74	6000 rpm	130	4300 rpm
Nissan	Qashqai	1.2 DIG-T 115	85	4500 rpm	190	2000 rpm
Peugeot	3008	1.2L PureTech 130 S&S	96	5500 rpm	230	1750 rpm
Renault	Kadjar	ENERGY TCe 130	96	5500 rpm	205	2000 rpm
Renault	Scenic	New TCe 115	85	4500 rpm	220	1500 rpm
Hyundai	Tucson	1.6 GDi 132ps 2WD	97	6300 rpm	161	4850 rpm
Kia	Sportage	1.6 GDi Petrol 130bhp Manual	97	6300 rpm	161	4850 rpm
Volkswagen	Tiguan	1.4 ltr TSI 125 PS 2WD	92	5000 - 6000 rpm	200	1400 - 4000 rpm
Volkswagen	Touran	1.2 ltr TSI 110 PS	81	4600 - 5600 rpm	175	1400 - 4000 rpm
Ford	Kuga	1.5 EcoBoost 120 PS Manual	88		240	
Audi	A4	1.4 TFSI	110	5000 - 6000 rpm	250	1500 - 3500 rpm
Volkswagen	Passat	1.4 ltr TSI 125 PS	92	5000 - 6000 rpm	200	1400 - 4000 rpm
Mercedes	GLC	GLC 250 4MATIC	155	5500 rpm	350	1200 - 4000 rpm
Mercedes	C Class	C200	135	5500 rpm	300	1200 - 4000 rpm

Appendix 2

Data of BEVs

Manufacturer	Model	Model year	Length (mm)	Width (mm)	Height (mm)	Unladen vehicle weight (kg)	Gross vehicle weight (kg)
Smart	forfour el. dr.	2017	3495	1663	1555	1200	1450
Volkswagen	e-up!	2016	3600	1645	1489	1229	1530
Fiat	500e	2015	3617	1627	1527	1355	
Renault	Zoe	2017	4084	1730	1562	1470	1965
BMW	i3	2017	4021	1775	1598	1343	1620
Nissan	Leaf 18	2017	4445	1770	1550	1544	1995
Hyundai	IONIQ Electric	2017	4470	1820	1450	1475	1880
Honda	FIT EV	2014	4114	1719	1580	1475	
Kia	Soul EV	2015	4140	1800	1593	1490	1960
Volkswagen	eGolf	2017	4258	1799	1492	1615	2020
Chevrolet	Bolt EV	2017	4166	1765	1598	1616	
Ford	Focus Electric Hatch	2017	4391	1824	1478	1651	2007
Mercedes Benz	B-Class el. dr.	2017	4358	1812	1599	1725	2170
BYD	e6	2015	4554	1822	1630	2020	2755
Tesla	Model 3 Standard	2017	4694	1933	1443	1609	
Tesla	Model S 75D	2017	4970	1964	1445	2108	2590
Rimac	Concept One	2015	4146	1854	1070	1900	
Mercedes Benz	SLS AmG El.Dr.	2015	4638	1939	1262	2110	2435
Audi	R8 e-tron	2015	4431	1929	1252	1841	

Manufacturer	Model	Model year	Accleration	Top speed (km/h)	Tyre Size
			0 - 100 kmph		
Smart	forfour el. dr.	2017	12,7	129	185/60 R15
Volkswagen	e-up!	2016	12,4	129	165/65 R15
Fiat	500e	2015	8,9	137	185/55 R16
Renault	Zoe	2017	13,5	135	185/65 R15
BMW	i3	2017	7,2	150	155/70 R19
Nissan	Leaf 18	2017	7,9	140	205/55 R16
Hyundai	IONIQ Electric	2017	9,9	166	205/55 R16
Honda	FIT EV	2014	8,5	148	185/65 R15
Kia	Soul EV	2015	11,2	147	205/60 R16
Volkswagen	eGolf	2017	9,6	150	205/55 R16
Chevrolet	Bolt EV	2017	6,5	150	215/50 R17
Ford	Focus Electric Hatch	2017	9,9	135	225/50 R17
Mercedes Benz	B-Class el. dr.	2017	7,9	160	225/50 R17
BYD	e6	2015	8	160	235/65 R17
Tesla	Model 3 Standard	2017	5,8	209	235/45 R18
Tesla	Model S 75D	2017	5,4	225	245/45 R19
Rimac	Concept One	2015	2,5	355	245/35 R20
Mercedes Benz	SLS AmG El.Dr.	2015	3,9	250	265/35 R19
Audi	R8 e-tron	2015	3,9	250	275/40 R19

Manufacturer	Model	Model year	Energy Converter				
			Technology	Peak Power (kW)		Torque (Nm)	
Smart	forfour el. dr.	2017	EESM	60		160	
Volkswagen	e-up!	2016		60	2800 rpm	210	2800 rpm
Fiat	500e	2015	PMSM	83		200	
Renault	Zoe	2017	EESM	68	3000 - 11300 rpm	220	250 - 2500 rpm
BMW	i3	2017		127	4800 rpm	250	
Nissan	Leaf 18	2017	AC Synchronous	110	3283 - 9795 rpm	320	3283 rpm
Hyundai	IONIQ Electric	2017		120		295	
Honda	FIT EV	2014		92	3695 - 10320 rpm	256	0 - 3056 rpm
Kia	Soul EV	2015		81,4	8000 rpm	285	2730 rpm
Volkswagen	eGolf	2017		100	3000 rpm	290	3000 rpm
Chevrolet	Bolt EV	2017	PMSM	150		360	
Ford	Focus Electric Hatch	2017	PMSM	107	5500 rpm	250	
Mercedes Benz	B-Class el. dr.	2017	IM	132	9900 - 12500 rpm	340	
BYD	e6	2015		200		550	
Tesla	Model 3 Standard	2017		192		430	
Tesla	Model S 75D	2017		386	6100 rpm	660	
Rimac	Concept One	2015		913		1600	0 - 65000 rpm
Mercedes Benz	SLS AmG El.Dr.	2015		552			
Audi	R8 e-tron	2015		340			